

REPORT DOCUMENTATION PAGE			Form Approved OMB NO. 0704-0188		
<p>The public reporting burden for this collection of information is estimated to average 1 hour per response, including the time for reviewing instructions, searching existing data sources, gathering and maintaining the data needed, and completing and reviewing the collection of information. Send comments regarding this burden estimate or any other aspect of this collection of information, including suggestions for reducing this burden, to Washington Headquarters Services, Directorate for Information Operations and Reports, 1215 Jefferson Davis Highway, Suite 1204, Arlington VA, 22202-4302. Respondents should be aware that notwithstanding any other provision of law, no person shall be subject to any penalty for failing to comply with a collection of information if it does not display a currently valid OMB control number.</p> <p>PLEASE DO NOT RETURN YOUR FORM TO THE ABOVE ADDRESS.</p>					
1. REPORT DATE (DD-MM-YYYY) 05-09-2017		2. REPORT TYPE Final Report		3. DATES COVERED (From - To) 1-May-2013 - 30-Apr-2017	
4. TITLE AND SUBTITLE Final Report: Novel MC/BZY Proton Conductor: Materials Development, Device Evaluation, and Theoretical Exploration using CI and DFT Methods			5a. CONTRACT NUMBER W911NF-13-1-0158		
			5b. GRANT NUMBER		
			5c. PROGRAM ELEMENT NUMBER 206022		
6. AUTHORS			5d. PROJECT NUMBER		
			5e. TASK NUMBER		
			5f. WORK UNIT NUMBER		
7. PERFORMING ORGANIZATION NAMES AND ADDRESSES Benedict College Office of Research 1600 Harden Street Columbia, SC 29204 -1058			8. PERFORMING ORGANIZATION REPORT NUMBER		
9. SPONSORING/MONITORING AGENCY NAME(S) AND ADDRESS (ES) U.S. Army Research Office P.O. Box 12211 Research Triangle Park, NC 27709-2211			10. SPONSOR/MONITOR'S ACRONYM(S) ARO		
			11. SPONSOR/MONITOR'S REPORT NUMBER(S) 62940-CH-REP.33		
12. DISTRIBUTION AVAILABILITY STATEMENT Approved for public release; distribution is unlimited.					
13. SUPPLEMENTARY NOTES The views, opinions and/or findings contained in this report are those of the author(s) and should not be construed as an official Department of the Army position, policy or decision, unless so designated by other documentation.					
14. ABSTRACT					
15. SUBJECT TERMS					
16. SECURITY CLASSIFICATION OF:			17. LIMITATION OF ABSTRACT UU	15. NUMBER OF PAGES	19a. NAME OF RESPONSIBLE PERSON Changyong Qin
a. REPORT UU	b. ABSTRACT UU	c. THIS PAGE UU			19b. TELEPHONE NUMBER 803-705-4582

RPPR Final Report
as of 03-Nov-2017

Agency Code:

Proposal Number: 62940CHREP

Agreement Number: W911NF-13-1-0158

INVESTIGATOR(S):

Name: Changyong Qin
Email: changyong.qin@benedict.edu
Phone Number: 8037054582
Principal: Y

Name: kevin Huang
Email: huang46@cec.sc.edu
Phone Number: 8037770204
Principal: N

Organization: **Benedict College**

Address: Office of Research, Columbia, SC 292041058

Country: USA

DUNS Number: 073727943

EIN: 570314365

Report Date: 31-Jul-2017

Date Received: 05-Sep-2017

Final Report for Period Beginning 01-May-2013 and Ending 30-Apr-2017

Title: Novel MC/BZY Proton Conductor: Materials Development, Device Evaluation, and Theoretical Exploration using CI and DFT Methods

Begin Performance Period: 01-May-2013

End Performance Period: 30-Apr-2017

Report Term: 0-Other

Submitted By: Changyong Qin

Email: changyong.qin@benedict.edu

Phone: (803) 705-4582

Distribution Statement: 1-Approved for public release; distribution is unlimited.

STEM Degrees: 7

STEM Participants: 12

Major Goals: This project has the goals listed below.

- 1) Synthesis of the MC/BZY composite as proton conductors for LT-SOFCs
- 2) Characterization and electrochemical evaluation of MC/BZY
- 3) Proton conduction in molten carbonate: mechanism and kinetics
- 4) Proton migration at the MC/BZY interface: enhanced conduction mode
- 5) Other fundamental physical and chemical properties of molten carbonate based composites
- 6) Enhancing the research capacity at Benedict College through the establishment of a research center for advanced materials
- 7) Training minority students in the field of STEM
- 8) Serving the local African American community including local middle and high schools

Accomplishments: 1) A new type MC/BZY hybrid proton conductor was obtained and tested.

2) A LT-SOFC with MC/BZY electrolyte (proton conductor) was assembled and tested.

3) Mechanism of proton transfer in molten carbonate was revealed using DFT modeling.

4) Kinetics of proton transfer in MC was analyzed with DFT and experiments.

5) The Center for Advanced Materials at Benedict College was established, serving minority students for STEM research and education.

6) The research capacity at Benedict College was largely enhanced through the purchase of the research equipments from the current grant.

7) Seven STEM students completed their B.S. degree through the support of the current grant.

8) One Ph.D. student completed the advanced degree through the support of the current grant.

9) More than 10 papers have been published (or being published) as a direct result of the current grant.

10) Two postdoc fellows received training through the support of the current grant.

RPPR Final Report as of 03-Nov-2017

Training Opportunities: 1) Seven undergraduate senior papers completed for B.S. degrees
2) Twelve undergraduate summer research assistantship/internship offered
3) Summer workshops for local middle/high school student
4) One Ph.D. dissertation completed (Co-PI group)
5) Two postdoc fellows trained

Results Dissemination: 1) Summer workshop on fuel cells to local middle/high school students
2) Open house to community members during the annual campus Harambee Festival

Honors and Awards: 1) Dr. Changyong Qin, the faculty of the year award, 2013
2) Dr. Changyong Qin, Excellence in Teaching Award by South Carolina Independent Colleges and Universities, 2014
3) Numerous research presentation awards in on and off campus conferences
4) Susan Njoki, WoPhyS 2015, Travel Award

Protocol Activity Status:

Technology Transfer: Nothing to Report

ARTICLES:

Publication Type: Journal Article Peer Reviewed: Y **Publication Status:** 1-Published

Journal: The Journal of Physical Chemistry C

Publication Identifier Type: DOI

Publication Identifier: 10.1021/acs.jpcc.6b09105

Volume: 121

Issue: 5

First Page #: 2635

Date Submitted: 9/5/17 12:00AM

Date Published: 1/1/17 5:00AM

Publication Location:

Article Title: CO Oxidation by Molecular and Atomic Oxygen on Ag(100): A Density Functional Theory Study

Authors: Xueling Lei, Godwin Mbamalu, Changyong Qin

Keywords: CO; Oxidation; Silver; Catalysis; DFT

Abstract: See the PDF

Distribution Statement: 1-Approved for public release; distribution is unlimited.

Acknowledged Federal Support: Y

Publication Type: Journal Article

Peer Reviewed: Y

Publication Status: 1-Published

Journal: Scientific Reports

Publication Identifier Type: DOI

Publication Identifier: 10.1038/s41598-017-07726-3

Volume: 7

Issue: 1

First Page #:

Date Submitted: 9/5/17 12:00AM

Date Published: 8/1/17 4:00AM

Publication Location:

Article Title: Proton Transfer in Molten Lithium Carbonate: Mechanism and Kinetics by Density Functional Theory Calculations

Authors: Xueling Lei, Kevin Huang, Changyong Qin

Keywords: Molten Carbonate, Proton transfer, solid oxide fuel Cell, proton conductor, density functional theory

Abstract: Using static and dynamic density functional theory (DFT) methods with a cluster model of $[(\text{Li}_2\text{CO}_3)_8\text{H}]^+$, the mechanism and kinetics of proton transfer in lithium molten carbonate (MC) were investigated. The migration of proton prefers an inter-carbonate pathway with an energy barrier of 8.0 kcal/mol at the B3LYP/6-31G(d,p) level, which is in good agreement with the value of 7.6 kcal/mol and 7.5 kcal/mol from experiment and FPMD simulation, respectively. At transition state (TS), a linkage of O---H---O involving O 2p and H 1s orbitals is formed between two carbonate ions. The calculated trajectory of H indicates that proton has a good mobility in MC, oxygen can rotate around carbon to facilitate the proton migration, while the movement of carbon is very limited. Small variations on geometry and atomic charge were detected on the carbonate ions, implying that the proton migration is a synergetic process and the whole carbonate structure is actively involved. Overall, the calculated result

Distribution Statement: 1-Approved for public release; distribution is unlimited.

Acknowledged Federal Support: Y

RPPR Final Report
as of 03-Nov-2017

Publication Type: Journal Article Peer Reviewed: Y **Publication Status:** 5-Submitted

Journal: Applied Catalysis B: Environmental

Publication Identifier Type: ISSN

Publication Identifier: 0926-3373

Volume:

Issue:

First Page #:

Date Submitted: 9/5/17 12:00AM

Date Published:

Publication Location:

Article Title: Molten Carbonate as a Non-metal Catalyst for CO Oxidation

Authors: Jingjing Tong, Xueling Lei, Peng Zhang, Kevin Huang, Godwin Mbamalu and Changyong Qin

Keywords: Molten Carbonate; Carbon Monoxide; Oxidation; Catalysis; Density Functional Theory

Abstract: For the first time, we have examined molten carbonate as a non-metal catalyst for the CO oxidation at the temperature of 300~600 °C. The reaction mechanism was analyzed using a classic Langmuir-Hinshelwood model combined with DFT calculations. It was found that the conversion is largely enhanced by melting at about 450 °C and increased to 96% at 500 °C. The reaction process includes four steps: (1) dissociative adsorption of oxygen, (2) adsorption of CO, (3) surface reaction, and (4) desorption of CO₂. DFT modeling reveals the formation of (C₂O₄)²⁻ and (CO₄)²⁻ as the intermediate species, and that the first two steps are exothermic and preferred by chemical equilibrium. The energy barrier of oxygen dissociation to form CO₄²⁻ is calculated to be 23.0 kcal/mol from Ref. [28], which is in a good agreement with the measured overall activation energy of 19.0 kcal/mol. However, the surface reaction (step 3) has much lower energy barrier of 11.4 kcal/mol. This confirms that the oxygen dissociation

Distribution Statement: 1-Approved for public release; distribution is unlimited.

Acknowledged Federal Support: Y

DISSERTATIONS:

Publication Type: Thesis or Dissertation

Institution: Benedict College

Date Received: 07-Nov-2016

Completion Date: 4/25/16 6:16PM

Title: DFT Study of CO Oxidation by Molten Carbonate

Authors: Susan Njoki

Acknowledged Federal Support: Y

Publication Type: Thesis or Dissertation

Institution: Benedict College

Date Received: 05-Sep-2017

Completion Date: 5/12/17 7:42PM

Title: Effect of Calcium Doping on Oxygen Migration in Molten Carbonate

Authors: Juan Pablo Medina

Acknowledged Federal Support: Y

Publication Type: Thesis or Dissertation

Institution: Benedict College

Date Received: 05-Sep-2017

Completion Date: 5/12/17 4:00AM

Title: Interaction of NO_x with Molten Carbonate Relevant to DeNO_x

Authors: Tiffany A. Bolton

Acknowledged Federal Support: Y

RPPR Final Report
as of 03-Nov-2017

Publication Type: Thesis or Dissertation

Institution: University of South Carolina

Date Received: 05-Sep-2017

Completion Date: 5/12/17 4:00AM

Title: Conductivity and Oxygen reduction Reaction -An Experimental and Computational Study

Authors: Xiaolei Xiong

Acknowledged Federal Support: **Y**

Novel MC/BZY Proton Conductor: Materials Development, Device Evaluation, and Theoretical Exploration using CI and DFT Methods

Changyong Qin, Benedict College, Columbia, SC 29204 (PI)

Kevin Huang, University of South Carolina, Columbia, SC 29208 (Co-PI)

Scientific and Technical Part for 62940-CH-REP

TABLE OF CONTENT:

SUMMARY	PAGE 02
PART A: MECHANISM AND KINETICS OF PROTON TRANSFER IN MOLTEN CARBONATE	PAGE 03
PART B: BZY-MC COMPOSITE AS PROTON CONDUCTOR	PAGE 15
PART C: PROTON TRANSFER AT BYZ AND CARBONATE INTERFACE	PAGE 24
PART D: CO OXIDATION BY MOLTEN CARBONATE	PAGE 33
PART E: CO OXIDATION BY ATOMIC AND MOLECULAR OXYGEN ON AG(100)	PAGE 42

SUMMARY FOR PROPOSAL 62940-CH-REP

The current funded project has been very successful in the scientific development in addition to its broad impacts on the research infrastructure, minority STEM student research training and community services. The project was performed based on the originally proposed tasks and schedule timeline with minor modifications according to the actual process. Overall, several important topics were investigated using combined experimental and theoretical modeling methodology. Those topics are of great interest and importance to not only the science and technology community, but also to DoD and Army Research Office. The research results are encouraging and they are reported as Part A-E in this report in a format of a scientific publication, respectively.

PART A: MECHANISM AND KINETICS OF PROTON TRANSFER IN MOLTEN CARBONATE

A1. Introduction and Background

Solid oxide fuel cells (SOFCs) are of growing interest as clean energy source due to the advantages they provide, including high efficiency, low emission and fuel flexibility¹⁻⁸. Both oxygen-ion (o-SOFCs)¹⁻⁴ and proton conductor (p-SOFCs)⁵⁻⁸ based electrolytes have been extensively examined. The o-SOFCs normally operate at high temperatures of 700-1000 °C, causing severe issues like thermo-mechanical compatibility and chemical stability, and also leading to high fabrication cost. For p-SOFCs, the operating temperature is much lower (400-600 °C) using the perovskite of BaCeO₃ (BC) and its doped derivatives as electrolytes⁹⁻¹¹, making them promising candidates for commercial power generators. However, the cerates react badly with CO₂ and become dysfunctional. Despite many efforts to improve the performance of BC-based electrolytes, BaZrO₃ (BZ) and its derivatives¹²⁻¹⁵ are considered as alternatives. The BZ-based electrolytes are chemically stable, but challenged by low conductivity at the desired temperature range. To achieve the commercial feasibility, durable electrolytes with high conductivity at 400-600 °C is necessary.

Yttrium-doped barium zirconate (BZY) is one of the promising proton conducting electrolytes for intermediate temperatures (IT) SOFCs due to its excellent chemical stability and good bulk proton conductivity. However, its refractory nature makes itself very difficult to sinter and hard to achieve high density structure. More recently, Huang et al.¹⁶⁻¹⁷ reported that densification of BZY can be promoted by adding molten carbonate (MC) as a sintering aid. MC was filled into the pores of BZY first by infiltration method. Interestingly, not only high density structure of BZY was observed, but also high ionic conductivity of 0.33 and 0.38 S/cm at 600 °C in 3% H₂O-air and 3% H₂O-H₂, respectively. The contribution from proton transfer to the ionic conductivity was found to be about 55% and the MC phase had played a significant role in the proton conduction. The conduction mechanism was mainly proposed by the equation below.



This enhanced conductivity implies that the MC phase in BZY can provide extra channels for proton migration. Similar hybrid systems of MC with BZY, BCZY¹⁸⁻¹⁹, and even oxygen-ion conductor²⁰⁻²⁴ as IT-SOFC electrolyte have been previously reported by other groups and largely enhanced cell performance was observed. Such composite electrolytes are easy to fabricate with low cost, which will open a door for developing novel electrolytes for IT-SOFCs. In addition, it is important to point out that the contribution from hydroxide ion (OH⁻) to the proton conductivity was not considered here, while this was reported to be noticeable in Ref. 25. In fact, the effect of water on the proton conductivity was already examined independently by two different groups^{17, 19}. Both reported that the conductivity was increased by only 6-8% when water partial pressure changes from 0 atm to 0.3 atm in 5% H₂ Ar or N₂. This increase was explained due to the reaction of water with the surface defect (oxygen vacancy) and carbonate to produce HCO₃⁻ and OH⁻ as proton carriers. Therefore, it is fairly reasonable to think the contribution of HCO₃⁻ to the proton conductivity is much larger than that of OH⁻. The role of OH⁻ is not examined in the current study, but should be considered in the future.

In bulk perovskite oxides, proton transfer occurs through hopping between adjacent oxygen ions at normal lattice sites via a Grotthuss-type mechanism²⁶. Further, experimental and

computational data indicate that the proton transfer involves two steps: rotational diffusion around an oxygen ion and transfer diffusion toward a neighboring oxide ion²⁷⁻³². For proton conduction in BZY/MC as described in Eqn (1), the protons produced by surface defect reactions were transferred to the neighboring carbonate-ions (CO_3^{2-}) at the BZY/MC interface to form HCO_3^- . They will then be transported inside of the MC phase. However, such assumption has not been verified in any form yet. Previously, we have reported a static DFT study of the proton transfer in the crystal structure of lithium carbonate³³. The calculated energy barrier was 0.34 eV along the direction of [001]. However, the experiments in Ref. 16-17 have shown that the MC phase only have large contributions to the ionic conductivity when it is melt at higher temperature than 450 °C. This implies that the results in Ref 33 are not enough for understanding the proton conduction mechanism in molten carbonate. In the current study, two significant improvements have been made. One is to use a disordered cluster model to represent the MC phase, which is close to the real situation and should produce more reliable results. The second is to include the effect of finite temperature using the first-principles molecular dynamics (FPMD) method.

A2: Modeling Methodology

In particular, the cluster of $(\text{Li}_2\text{CO}_3)_8$ was used to represent the MC phase and those calculations were performed in two steps. In the first step, all gas phase geometries of $[(\text{Li}_2\text{CO}_3)_8\text{H}]^+$ cluster were optimized at the B3LYP³⁴⁻³⁵/6-31G(d,p)³⁶⁻³⁹ level using the Gaussian 09 program⁴⁰. All stationary points on the potential energy surface (PES) were then verified by calculated vibrational frequencies at the same theoretical level. Therefore, the reactant and product structures are truly local minima while each transition state at the first order saddle point is on the PES. For such a large molecular system, locating a transition state is time consuming and challenging. To quickly achieve this, we performed a geometry scan first, then used the structure with the highest energy for TS search, and finally verified the reaction pathways using the intrinsic reaction coordinate (IRC) calculations. In the second step, we applied the VASP code (version 5.3.5)⁴¹⁻⁴² to perform first-principles molecular dynamics (FPMD) calculations. The optimized structure of $[(\text{Li}_2\text{CO}_3)_8\text{H}]^+$ from step one is used as the starting geometry. All FPMD simulations were conducted with the NVT ensemble. PAW-PBE potentials⁴³⁻⁴⁵ were used for H (ultrasoft), Li (s1p0), C (s2p2), and O (s2p4) with the energy cutoff of 500 eV. A Verlet algorithm was integrated with Newton's equations of motion at a time step of 0.1 fs for a total simulation time of 3 ps, *i.e.*, 30000 time steps in total. The frequency of the temperature oscillations was controlled by the Nosé mass during the simulations. Additional, a $1\times 1\times 1$ k-point mesh was used at the Γ -point.

The proton transfer process is local and the reaction is usually at high temperature in a molten carbonate salt, both of which will bring detriments to the results from static DFT calculations in the gas phase using a limited size of cluster model. For example, the calculated energy barrier includes contributions from not only the proton migration itself, but also the variation of the cluster geometry. Therefore, there are possible uncertainties in the calculated energetics. To verify and correct such possible errors, we have re-examined the energies from local structures extracted from the cluster and the revised values showed large improvements and better consistency with current FPMD results and previous experimental results¹⁷. In addition, long range interactions in the molecular system were estimated by CAM-B3LYP⁴⁶, but no significant difference was observed.

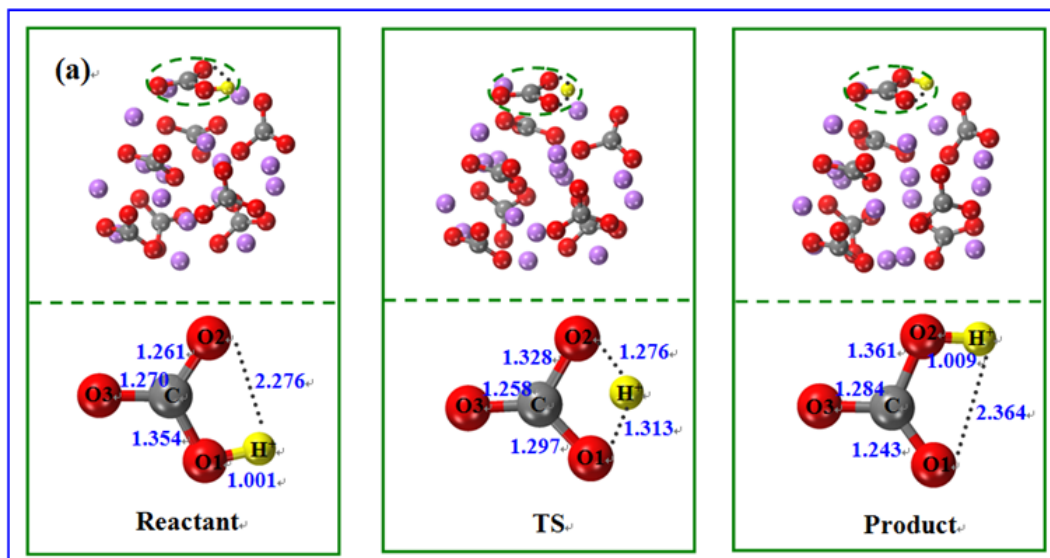
A3: Results and discussion

A3.1: DFT results of proton migration in the $(\text{Li}_2\text{CO}_3)_8$ cluster

Intra-carbonate migration of proton

For the migration of proton in MC, both intra and inter-carbonate pathways are possible and they will be discussed separately. As reported in Ref. 33, the cluster of $(\text{Li}_2\text{CO}_3)_8$ is fairly reliable to represent the disordered molten carbonate with affordable computing time. Fig. 1 shows the optimized structures of reactant, transition state (TS), product together with the relative energy for proton migration inside of a carbonate ion in the cluster of $(\text{Li}_2\text{CO}_3)_8$. At the beginning, the proton (H^+) is connected to O1 with the O1- H^+ distance of 1.001 Å. It then starts moving toward O2, leading to a TS. At TS, the only imaginary frequency is $i1851\text{ cm}^{-1}$, corresponding to the shifting of H^+ from O1 to O2. From reactant to TS, the O1- H^+ bond is stretched to 1.313 Å, while O2- H^+ shortened to 1.276 Å. At the same time, C-O1 is shortened from 1.354 Å to 1.297 Å, while C-O2 elongated from 1.261 Å to 1.328 Å. It is also noticeable that the O1-C-O2 bond angles is bent to 106.6° , which brings O1 and O2 closer and will facilitate the proton migration. The Mulliken population analysis shows a loss of 0.02 e for O1 from reactant to TS, gain of 0.05 e for O2 and loss of 0.04 e for carbon. All results indicate that the proton migration is a concerted process and involves 2p orbitals of O1-C-O2. Fig. 1(c) displays the main bonding orbital between proton with O1 and O2 at TS. It is very clear that the 2p lone pairs of O1 and O2 combine with H 1s, forming a bent O1-H-O2 linkage. The cleavage of O1- H^+ and formation of O2- H^+ is reversible as verified by the IRC calculations.

The calculated energy barrier for proton migration from O1 to O2 is 46.8 kcal/mol and 40.4 kcal/mol for the reverse process. The energy difference between the initial and final state is 6.4 kcal/mol. With long range corrections by CAM-B3LYP, the barrier is 47.6 kcal/mol and 39.9 kcal/mol, respectively, showing negligible contribution from long range interactions in the system. However, the value is only 20.5 kcal/mol in Ref. 33, which was calculated based on a single molecule of HCO_3^- . To eliminate possible uncertainty in the calculated energy barrier as discussed before, we have extracted a small HCO_3^- cluster out of the whole structure and re-calculated the energies. The energy barrier is decreased to 17.2 kcal/mol and 17.5 kcal/mol for the reverse step. The energy change for the migration process is reduced to 0.3 kcal/mol. Both imply that the contribution from geometry variation in the cluster other than proton migration itself is significant and the results from such calculations should be carefully evaluated and verified.



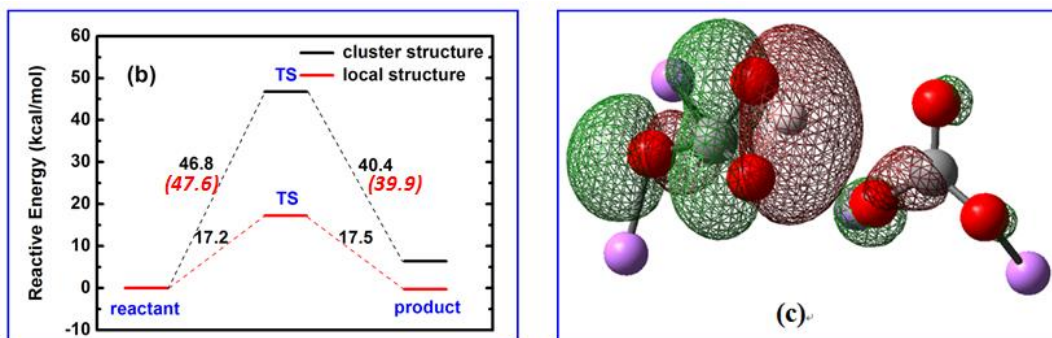


Fig. 1: (a) Structures of reactant, transition state (TS) and product, the upper panel is the whole cluster, while local structure only for the lower panel; (b) Relative energy for proton migration inside of a carbonate ion calculated by the whole cluster and local structure, respectively; (c) Selected molecular orbital in TS for bonding between proton and carbonate. The proton, carbon, oxygen and lithium atoms are shown as yellow, gray, red, and purple respectively. (Distance in Å and relative energy in kcal/mol.)

Inter-carbonate migration of proton

Fig. 2 shows the optimized structures of reactant, TS, product as well as the relative energy for proton migration through an inter-carbonate pathway in the cluster of $(\text{Li}_2\text{CO}_3)_8$. Unlike the intra-carbonate process, this pathway involves two neighboring carbonates. As shown in Fig. 2(a), a TS structure for the migration of H^+ between O2 and O5 was located on the PES. At TS, the only imaginary frequency is $i387\text{ cm}^{-1}$, corresponding to the migration of H^+ from O2 to O5. At the beginning, the O2- H^+ distance is 1.041 Å , similar to O1- H^+ in Fig. 1(a). However, it is only 1.492 Å for O5- H^+ , which is 0.784 Å shorter than O2- H^+ in Fig. 1(a), implying that the inter-carbonate pathway is possibly favored by structure. At TS, a linear O2-H-O5 linkage is formed between two carbonate ions with the O2- H^+ and O5- H^+ distance of 1.152 Å and 1.281 Å , respectively. Fig. 2(c) shows large overlap between 2p of O2 and O5, and 1s of H. The Mulliken population analysis indicates a gain of 0.10 e for O2, loss of 0.02 e for O5, and gain of 0.03 e for C1 from reactant to TS. A similar trend is observed for the reverse path from product to TS. Although the absolute values of charge are not very reliable, the small variations of electron density on the atoms where the proton migration occurs indicate that this is a synergetic process between proton and the two carbonate ions.

The calculated energy barrier is 21.6 kcal/mol from reactant to TS, while only 9.6 kcal/mol from product back to TS. It becomes 20.8 kcal/mol and 8.2 kcal/mol after the long range correction by CAM-B3LYP, respectively. The large energy difference between reactant and product (12.0 kcal/mol) implies the fact that the cluster of product from IRC might be a local minimum on PES, i.e. an intermediate structure. A similar phenomenon was observed in Ref. 33, where a very small activation energy of 1.8 kcal/mol was reported for the proton transfer between two carbonate ions. Using an extracted cluster $\text{Li}_2\text{CO}_3\text{-H}^+\text{-Li}_2\text{CO}_3$ as shown in Fig. 2(a), the energy barrier is reduced to 8.0 kcal/mol and 8.3 kcal/mol , respectively. This again confirms that the gas phase calculation may overestimate the activation energy for a molten salt system using a simple cluster model. From the current study, it is found that the calculated energy barriers will have to be checked and verified by other methods, which will be discussed in more details. Comparison of the calculated energy barriers suggests that the proton migration proceed through inter-

carbonate rather than intra-carbonate in the lithium molten carbonate, which agrees with the results from the geometry and charge analysis.

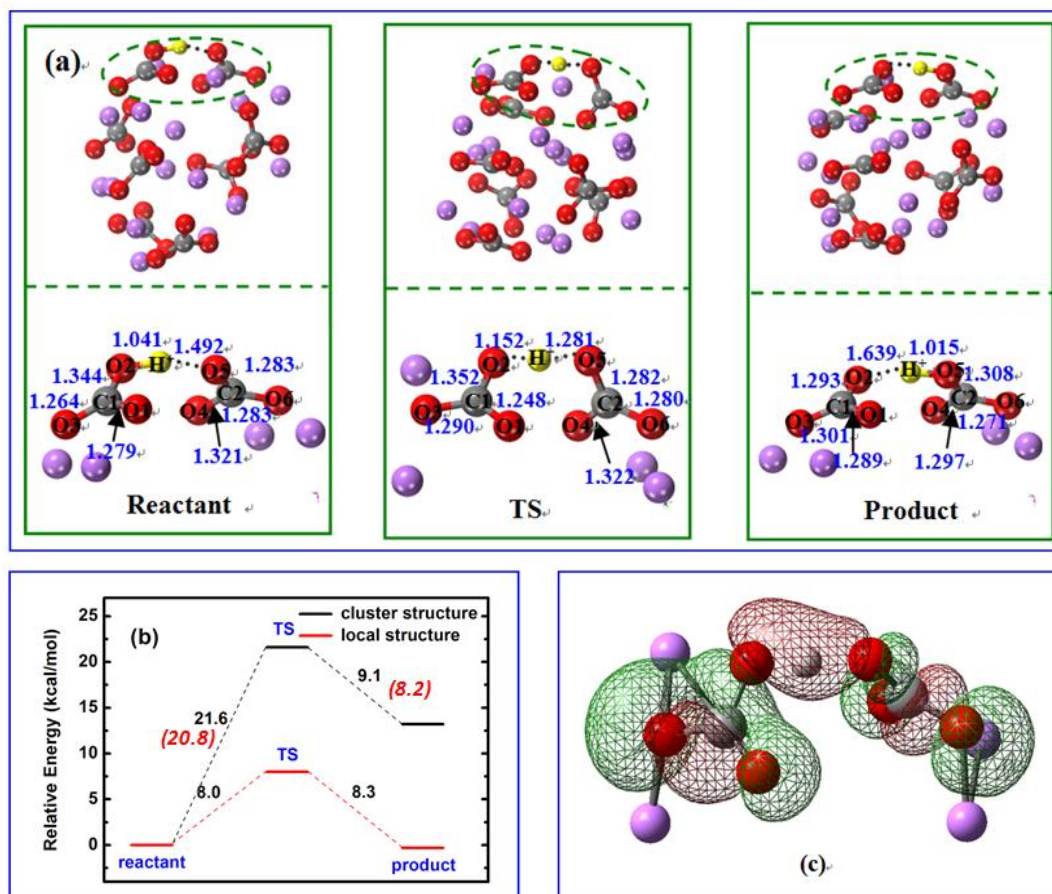


Fig. 2: (a) Structures of reactant, transition state (TS), and product, the upper panel is cluster structure and the lower panel is local structure; (b) Relative energy for proton migration for inter-carbonate in the $(\text{Li}_2\text{CO}_3)_8$ cluster and local structure, respectively; (c) Selected molecular orbital in TS for bonding between proton and carbonate. The proton, carbon, oxygen and lithium atoms are shown as yellow, gray, red, and purple respectively. (Distance in Å; Relative energy in kcal/mol.)

A3.2: FPMD evidences of proton migration in the $(\text{Li}_2\text{CO}_3)_8$ cluster

Trajectories of the proton, carbon, and oxygen atoms

To account for the effects of temperature on the proton migration in the lithium molten carbonate, we carried out first-principles molecular dynamics calculations. Fig. 3 shows a series of the snapshots of proton position at 1300 K in a time interval of 0.5 ps and the corresponding trajectory of proton, carbon and oxygen ion in the $(\text{Li}_2\text{CO}_3)_8$ clusters simulated at 1300 K for 3 ps. The proton position in each snapshot has experienced noticeable change with the time, indicating a fast proton diffusion process. The trajectory of proton is largely dispersed while the trajectory of carbon is quite localized, indicating that the proton migration in the $(\text{Li}_2\text{CO}_3)_8$ cluster is very fast with large displacement, while the carbon atoms only vibrate around their original sites with very limited displacement. It should also be noted that the trajectory of the

oxygen atom is more dispersed than that of carbon, implying that the oxygen atoms can rotate and adjust their positions during the proton migration between the carbonate ions in the cluster of $(\text{Li}_2\text{CO}_3)_8$.

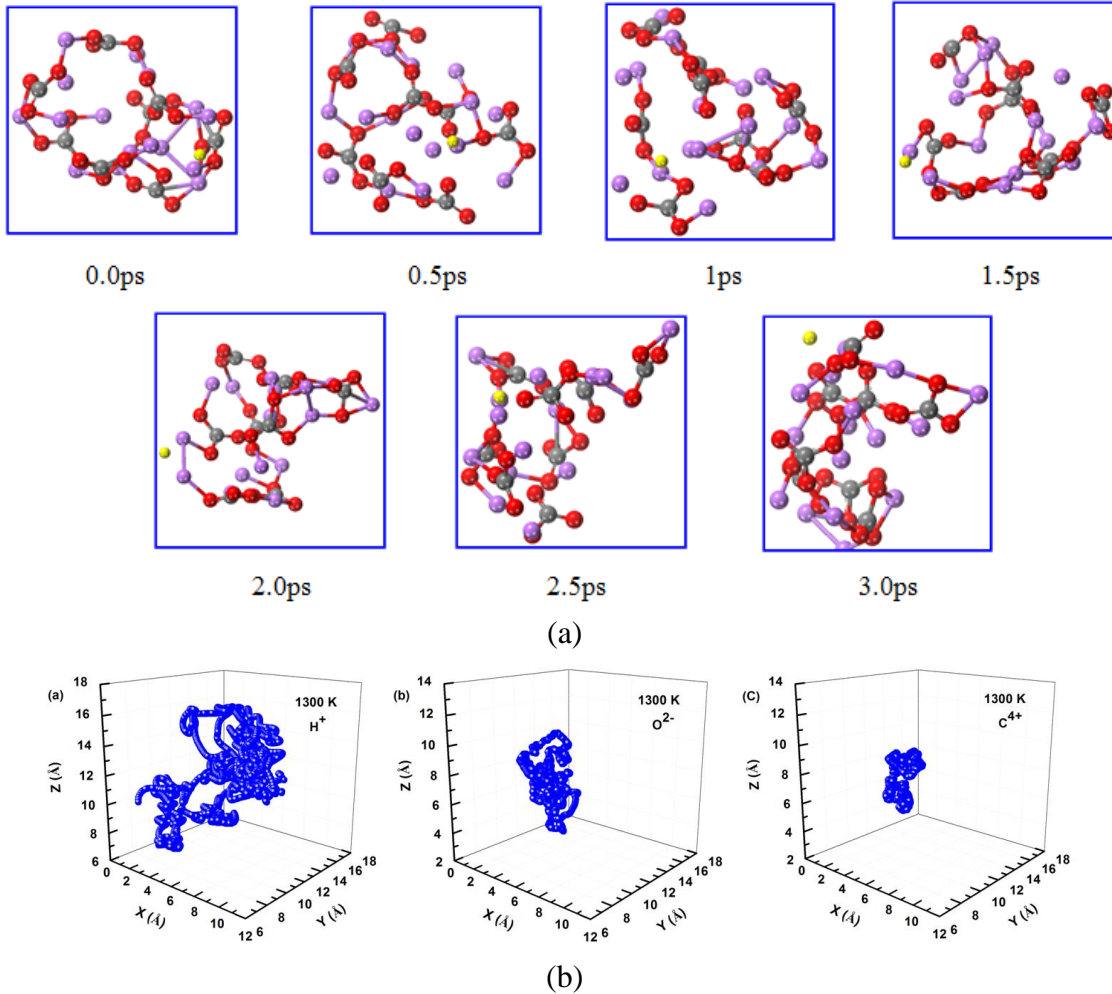


Fig. 3: (a) Snap-shots for proton transfer in the cluster of $(\text{Li}_2\text{CO}_3)_8$ simulated at 1300 K for 3 ps. The yellow ball represents the proton in motion. (b) Trajectory of proton, carbon, and oxygen ion in the cluster of $(\text{Li}_2\text{CO}_3)_8$ simulated at 1300 K for 3 ps.

Mean square displacement and Arrhenius plot

The mean square displacement (MSD) is determined by the ensemble average:

$$MSD(t) = \langle \delta r^2(t) \rangle = \frac{1}{N} \frac{1}{n} \sum_{i=0}^n \sum_{m=0}^N [r_m(t + t_{0i}) - r_m(t_{0i})]^2 \quad \text{Eqn (2),}$$

where N is the number of ions in the system, n is the number of time origins, t is the time, and t_{0i} is the initial time step originating at time i ⁴⁷⁻⁴⁸. In the current work, at least three FPMD runs were conducted for one structure at each temperature in order to obtain an averaged MSD for better reliability and accuracy. Fig. 4 shows the averaged mean square displacement for proton migration in the $(\text{Li}_2\text{CO}_3)_8$ clusters simulated at the temperature of 1100 K, 1200 K, 1300 K and 1400 K for 3 ps (here considering the melt point of lithium carbonate is about 996 K). Clearly, the MSD of proton increases linearly with time, indicating a fast proton migration in the

(Li₂CO₃)₈ clusters. Moreover, the slope of MSD increases as the temperature increases, indicating that the proton has higher ability of diffusion at increased temperature.

The diffusion coefficient is calculated by fitting the slope of the MSD vs. time:

$$D = \lim_{t \rightarrow \infty} \frac{MSD(t)}{6t} \quad \text{Eqn (3).}$$

Then, the Arrhenius plot can be obtained from the diffusion coefficient via Arrhenius relationship:

$$D(T) = D_0(T) \exp\left(-\frac{E_a}{k_B T}\right) \quad \text{Eqn (4).}$$

Herein, D_0 and E_a are the pre-exponential factor and the diffusion barrier, respectively. k_B is the Boltzmann constant and T is the absolute temperature. By fitting to the Arrhenius relationship (Eqn. 4) over the considered temperature range, the pre-exponential factor and the effective activation energy can be obtained. Fig. 5 shows the Arrhenius plot for proton migration in the cluster of (Li₂CO₃)₈. From the slope of the straight line, the activation energy is calculated to be 7.5 kcal/mol, which is in good agreement with the energy barrier of 8.0 kcal/mol for the proton migration between carbonate ions in the cluster of (Li₂CO₃)₈. The trajectory analysis and the activation energy strongly support that the proton transfer prefers the inter-carbonate pathway and suggest that static DFT methods with a limited size cluster model in the gas phase has uncertainties in describing the state of molten carbonate and that further refinement on calculated energies with extracted local structure is necessary. Such treatment can also be applied in treating similar molecular systems in future.

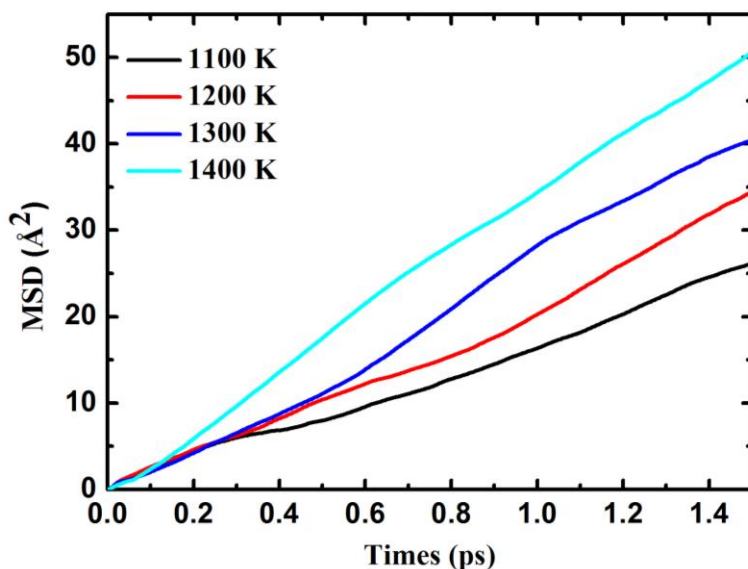


Fig. 4: MSD for proton transfer in the cluster of (Li₂CO₃)₈ simulated at 1100 K, 1200 K, and 1300 K for 3 ps.

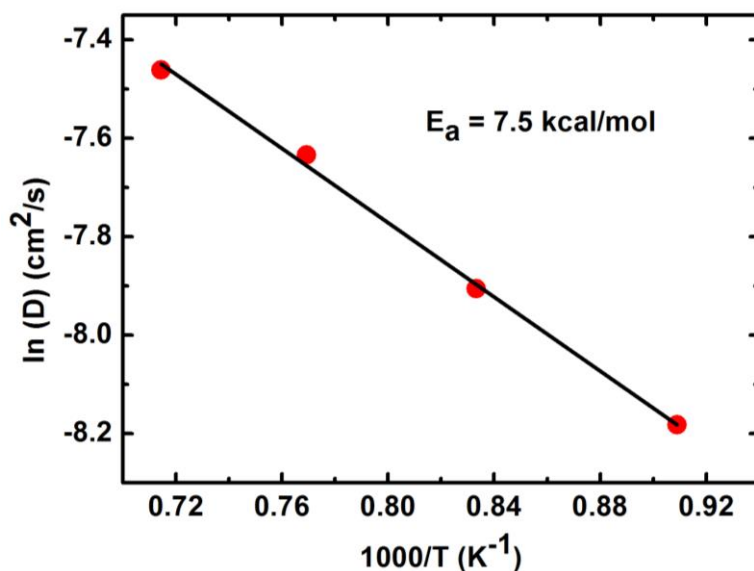


Fig. 5: Arrhenius plot for proton transfer in the cluster of $(\text{Li}_2\text{CO}_3)_8$

A3.3: Mechanism of proton transfer in MC

Due to the fact that the mechanism of proton migration in MC is complicated, both static DFT and FPMD calculations at finite temperatures have been performed in the current study. The results from DFT calculations in the gas phase have provided detailed information on structural evolution, charge transfer and energetics, while trajectories, MSD at different finite temperatures and activation energy by Arrhenius plot were obtained from FPMD. All theoretical evidences from multiple perspectives have supported that the inter-carbonate pathway is dominant for the proton migration in molten carbonate. However, the intra-carbonate pathway is still possible to serve as an intermediate step in the whole process. In addition, the combination of the static and dynamic DFT methods in this study has shown great advantages in treating such ionic liquid systems.

It is interesting to note that the degree of geometry change of the carbonate ions at TS is slightly different from the intra to inter-carbonate pathway. In Fig. 1(a), the changes of the O3 charge and O3-C bond distance are significantly smaller than those for other atoms and bonds in the carbonate ion, indicating O3 is not actively participated in the proton migration process. However, both O1-C and O2-C bonds change significantly during the process. One bond increases and the other will decrease accordingly. The O1-C-O2 bond is bent to 106.6° to accommodate the proton migration. This is consistent with the Lewis diagram in Fig. 6(a). With respect to the inter-carbonate path, all atoms in both carbonate ions have experienced some small changes in atomic charge and bond distance, showing they are all actively involved in the process. The O-C-O bond angles remain almost unchanged ($\sim 120^\circ$) in the whole process. The bond forming and breaking process can be described by the Lewis diagram in Fig. 6(b). Theoretically, if a reaction experiences more electron delocalization and less geometry distortion at TS, it should have a lower energy barrier. From this chemical aspect, the inter-carbonate path should be more favored by reaction kinetics.

For the energy barriers from static DFT calculations, they are obviously overestimated. This uncertainty is probably due to the structural variation of the ionic cluster, especially the part not

involved in the proton migration in the optimization process. The value of energy barrier itself is small, but the total energy of the cluster is large. To correct the errors, we have extracted the small local structure out of the whole cluster, which allows us to catch the energy change due to the proton migration and ignores the effect on the energy from the ions not involved in the process. The energy barrier was reduced from 46.8 to 17.5 kcal/mol for the intra-carbonate path and from 20.8 to 8.0 kcal/mol for the inter-carbonate one, respectively. Such large changes imply the challenges in treating such an ionic liquid of molten salt state using gas phase DFT and cluster models. The correction method used here has been very effective and is easy to apply, and further verifications will be carried out in the future. The final energy barrier from DFT is 8.0 kcal/mol, which is in a good agreement with the activation energy of 7.5 kcal/mol from FPMD simulations. The activation energy was measured to be 7.6 kcal/mol using a BZY/MC composition electrolyte at 600 °C and MC was considered as the main conducting media for protons¹⁷. Based on those values, we can conclude that the energy barrier for the migration of proton in molten lithium carbonate salt is in the range of 7.5-8.0 kcal/mol and excellent consistency between DFT modeling and experimental measurement was observed.

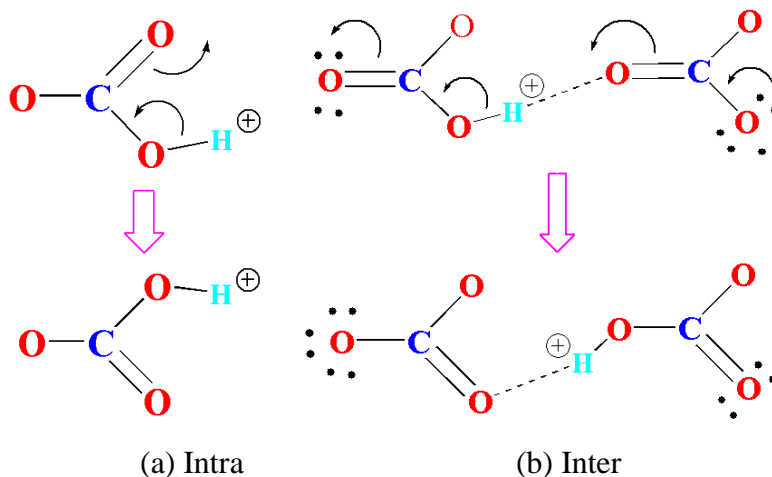


Fig. 6: Lewis Diagram for the Intra- (a) and Inter-Carbonate (b) Migration of Proton.

A4: Conclusions for Part A

The pathway and energy barrier of proton migration in the lithium molten carbonate are predicted by static and dynamic density functional theory calculations. The results show that the proton migration prefers the inter-carbonate to the intra-carbonate pathway. The migration energy barrier of 8.0 kcal/mol for local structure extracted from the $(\text{Li}_2\text{CO}_3)_8$ cluster is consistent with the 7.8 kcal/mol obtained from *ab initio* molecular dynamic simulations. Also, this result is excellent in line with the experimental value of 7.6 kcal/mol observed in a MC/BZY composition at 600 °C. The analyses of atomic charges, bond distances, bond angles, vibrational frequencies, and molecular orbitals all indicate that the proton migration in the lithium molten carbonate is a synergetic process. The trajectories of proton, carbon and oxygen suggest that the oxygen atoms can adjust their positions during the proton migration between the carbonate ions in the cluster of $(\text{Li}_2\text{CO}_3)_8$. The MSDs of proton simulations at temperatures of 1100 K, 1200 K, and 1300 K for 3 ps feature a linear increase with time, implying a fast proton migration in the lithium molten carbonate. Moreover, the mechanism of proton migration can be explained by the

Lewis electron dot diagram. Overall, the calculated results have an excellent agreement with our previous experimental results and indicate that molten carbonate can provide a low energy barrier channel for proton conduction in IT-SOFCs. The kinetics and mechanism of such process are well elucidated by DFT calculations. In addition, our calculations indicate that the combination of the static and dynamic DFT methods is of great advantages in treating such ionic liquid systems and can give reliable results.

A5: References for Part A

1. Stambouli, A. B., Traversa, E. "Fuel cells, an alternative to standard sources of energy." *Renew Sust Energ Rev* **6**, 297 (2002).
2. Stambouli, A. B., Traversa, E. "Solid oxide fuel cells (SOFCs): a review of an environmentally clean and efficient source of energy." *Renew Sust Energ Rev* **6**, 433 (2002).
3. Andújar, J. M., Segura, F. "Fuel cells: History and updating. A walk along two centuries." *Renew Sust Energ Rev* **13**, 2309 (2009).
4. Stambouli, A. B. "Fuel cells: The expectations for an environmental-friendly and sustainable source of energy." *Renew Sust Energ Rev* **15**, 4507 (2011).
5. Fabbri, E., Pergolesi D. and Traversa, E. "Materials challenges toward proton-conducting oxide fuel cells: a critical review." *Chem. Soc. Rev.* **39**, 4355 (2010).
6. Malavasi, L., Fisher C. A. J. and Islam, M. S. "Oxide-ion and proton conducting electrolyte materials for clean energy applications: structural and mechanistic features." *Chem. Soc. Rev.* **39**, 4370 (2010).
7. Kreuer, K. D. "PROTON-CONDUCTING OXIDES." *Annu. Rev. Mater. Res.* **33**, 333 (2003).
8. Fabbri, E., Bi, L., Pergolesi, D. and Traversa, E. "Towards the Next Generation of Solid Oxide Fuel Cells Operating Below 600 °C with Chemically Stable Proton-Conducting Electrolytes." *Adv. Mater.* **24**, 195 (2012).
9. Katahira, K., Kohchi, Y., Shimura, T., Iwahara, H. "Protonic conduction in Zr-substituted BaCeO₃." *Solid State Ionics* **138**, 91 (2000).
10. Xie, K. et al. "A stable and easily sintering BaCeO₃-based proton-conductive electrolyte." *J. Alloys Compd.* **473**, 323 (2009).
11. Dailly, J., Marrony, M. "BCY-based proton conducting ceramic cell: 1000 h of long term testing in fuel cell application." *J. Power Sources* **240**, 323 (2013).
12. Park, K. Y. et al. "Enhanced proton conductivity of yttrium-doped barium zirconate with sinterability in protonic ceramic fuel cells." *J. Alloys Compd.* **639**, 435 (2015).
13. Babilo, P., Uda, T., Haile, S. M. "Processing of yttrium-doped barium zirconate for high proton conductivity." *J. Mater. Res.* **22**, 1322 (2007).
14. Iguchi, F. et al. "The influence of grain structures on the electrical conductivity of a BaZr_{0.95}Y_{0.05}O₃ proton conductor." *Solid State Ionics* **177**, 2381 (2006).
15. D'Epifanio, A. et al. "Design of BaZr_{0.8}Y_{0.2}O_{3-δ} Protonic Conductor to Improve the Electrochemical Performance in Intermediate Temperature Solid Oxide Fuel Cells (IT-SOFCs)." *Fuel Cells* **08**, 69 (2008).

16. Li, X., Xu, N., Zhang, L., Huang, K. "Combining proton conductor $\text{BaZr}_{0.8}\text{Y}_{0.2}\text{O}_{3-\delta}$ with carbonate: Promoted densification and enhanced proton conductivity." *Electrochem. Commun.* **13**, 694 (2011).
17. Xiong, X. et al. "Synergetic proton conduction in $\text{BaZr}_{0.8}\text{Y}_{0.2}\text{O}_{3-\delta}$ -carbonate composite electrolyte for intermediate-temperature solid oxide fuel cells." *Solid State Ionics* **279**, 66 (2015).
18. Hei, Y., Huang, J., Wang, C., Mao, Z. "Highly conductive barium zirconate-based carbonate composite electrolytes for intermediate temperature-protonic ceramic fuel cells." *Int. J. Hydrog. Energy* **39**, 14328 (2014).
19. Park, K. Y. et al "Novel doped barium cerate-carbonate composite electrolyte material for low temperature solid oxide fuel cell." *J. Alloys Compd.* **585**, 103 (2014).
20. Zhu, B. et al. "Innovative low temperature SOFCs and advanced materials." *J. Power Sources*, **118**, 47 (2003).
21. Di, J. et al. "Samarium doped ceria- $(\text{Li}/\text{Na})_2\text{CO}_3$ composite electrolyte and its electrochemical properties in low temperature solid oxide fuel cell." *J. Power Sources*, **195**, 4695 (2010).
22. Bodén, A. et al. "Conductivity of SDC and $(\text{Li}/\text{Na})_2\text{CO}_3$ composite electrolytes in reducing and oxidising atmospheres." *J. Power Sources*, **172**, 520 (2007).
23. Xia, C. et al. "A high performance composite ionic conducting electrolyte for intermediate temperature fuel cell and evidence for ternary ionic conduction." *J. Power Sources*, **188**, 156 (2009).
24. Xia, C. et al. "Intermediate temperature fuel cell with a doped ceria-carbonate composite electrolyte." *J. Power Sources*, **195**, 3149 (2010).
25. Evans A., Xing W., and Norby T. "Electromotive Force (emf) Determination of Transport Numbers for Native and Foreign Ions in Molten Alkali Metal Carbonates" *J. of Electrochem. Soc.* **162**(10), F1135-1143 (2015).
26. Nowick A. S. and Du, Y. "High-temperature protonic conductors with perovskite-related structures." *Solid State Ionics* **77**, 137 (1995).
27. Kreuer, K. D. "On the complexity of proton conduction phenomena." *Solid State Ionics* **136-137**, 149 (2000).
28. Pionke, M. et al. "Investigation of the hydrogen mobility in a mixed perovskite: $\text{Ba}[\text{Ca}_{(1+x)/3}\text{Nb}_{(2-x)/3}]\text{O}_{3-x/2}$ by quasielastic neutron scattering." *Solid State Ionics* **97**, 497 (1997).
29. Kreuer, K. D., Fuchs A. and Maier, J. "H/D isotope effect of proton conductivity and proton conduction mechanism in oxides." *Solid State Ionics* **77**, 157 (1995).
30. Münch, W., Seifert, G., Kreuer K. D. and Maier, J. "A quantum molecular dynamics study of the cubic phase of BaTiO_3 and BaZrO_3 ." *Solid State Ionics* **97**, 39 (1997).
31. Münch, W., Seifert, G., Kreuer K. D. and Maier, J. "A quantum molecular dynamics study of proton conduction phenomena in BaCeO_3 ." *Solid State Ionics* **86-88**, 647 (1996).
32. Kreuer, K. D. "On the development of proton conducting materials for technological

- applications.” *Solid State Ionics* **97**, 1 (1997).
33. Lei, X., Qin C. and Huang, K. “Energetics of proton transfer in alkali carbonates: a first principles calculation.” *RSC Adv.* **5**, 56205 (2015).
 34. Lee, C., Yang, W., Parr, R. G. “Development of the Colle-Salvetti correlation-energy formula into a functional of the electron density.” *Phys. Rev. B* **37**, 785 (1988).
 35. Becke, A. D. “Density-functional thermochemistry. III. The role of exact exchange.” *J. Chem. Phys.* **98**, 5648 (1993).
 36. Francel, M. M. et al. “Self-consistent molecular orbital methods. XXIII. A polarization-type basis set for second-row elements.” *J. Chem. Phys.* **77**, 3654 (1982).
 37. Blaudeau, J. P., McGrath, M. P., Curtiss L. A. and Radom, L. “Extension of Gaussian-2 (G2) theory to molecules containing third-row atoms K and Ca.” *J. Chem. Phys.* **107**, 5016 (1997).
 38. Rassolov, V. A., Pople, J. A., Ratner M. A. and Windus, T. L. “6-31G* basis set for atoms K through Zn.” *J. Chem. Phys.* **109**, 1223 (1998).
 39. Rassolov, V. A. et al. “6-31G* basis set for third-row atoms.” *J. Comp. Chem.* **22**, 976 (2001).
 40. Frisch, M. J. et al. Gaussian 09, Revision B. 01, Gaussian Inc., Wallingford CT, 2010.
 41. Kresse, G., Hafner, J. “*Ab initio* molecular dynamics for liquid metals.” *J. Phys. Rev. B* **47**, 558(R) (1993).
 42. Kresse, G., Furthmüller J. “Efficient iterative schemes for *ab initio* total-energy calculations using a plane-wave basis set.” *J. Phys. Rev. B* **54**, 11169 (1996).
 43. Blöchl, P. E. “Projector augmented-wave method.” *Phys. Rev. B* **50**, 17953 (1994).
 44. Kresse, G., Joubert, D. “From ultrasoft pseudopotentials to the projector augmented-wave method.” *Phys. Rev. B* **59**, 1758 (1999).
 45. Perdew, J. P., Burke, K., Ernzerhof, M. “Generalized Gradient Approximation Made Simple.” *Phys. Rev. Lett.*, **77**, 3865 (1996).
 46. Yanai, T., Tew, D. and Handy, N. “A new hybrid exchange-correlation functional using the Coulomb-attenuating method (CAM-B3LYP).” *Chem. Phys. Lett.* **393**, 51 (2004).
 47. Croteau, T., Patey, G. N. “Structures and rearrangements of LiCl clusters.” *J. Chem. Phys.* **124**, 244506 (2006).
 48. Bengtson, A. Nam H. O., Saha S., Sakidja R., Morgan D. “First-principles molecular dynamics modeling of the LiCl–KCl molten salt system.” *Comput. Mater. Sci.* **83**, 362 (2014).

PART B: NEW MC/BZY HYBRID PROTON CONDUCTOR

B1: Experimental procedures

B1.1: Fabrication of MC/BZY Electrolyte

The BZY ($\text{BaZr}_{0.8}\text{Y}_{0.2}\text{O}_{3-\delta}$) electrolyte was synthesized via conventional solid-state reaction. The starting materials were BaCO_3 (99.8%, Alfa Aesar), ZrO_2 (99.7%, Alfa Aesar) and Y_2O_3 (99.9%, Alfa Aesar). Stoichiometric amount of the starting materials were first weighed, intimately mixed and pelletized, followed by firing at 1100°C for 5 h. The calcined pellets were then broken into powders and calcined again at 1300°C for another 5 h. After ball milling, the powders were then blended with ~10 wt% of carbon-black as a pore former, pelletized and finally sintered at 1500°C for 5 h. Thus made samples were porous and ready for molten carbonate infiltration.

Two molten carbonate systems were selected for this study: Li_2CO_3 -38mol% K_2CO_3 (denoted as LK) and Li_2CO_3 - 48mol% Na_2CO_3 (denoted as LN); these compositions reflect a eutectics. They were first melted and homogenized in an Al_2O_3 crucible at 650°C for 2 h. The porous BZY pellet pre-loaded in a silver basket were then slowly immersed into the MC. After a roughly 2-h soaking, they were gradually pulled out of the melt and suspended above the crucible before slowly cooling the furnace to room temperature. Thus fabricated MC-BZY composites were slightly polished to remove the residual carbonate on the surface. The samples were then ready for microstructural and electrical characterizations.

B1.2: Characterization of MC/BZY

The phase purity of the BZY powder and MC-BZY composites were examined by X-ray diffraction (XRD) using (D/max-A, Rigaku, Japan), while microstructures of the BZY as well MC-BZY composites were captured by a field emission scanning electron microscopy (FE-SEM, Zeiss Ultra).

The ionic conductivity of the MC-BZY composites was assessed by electrochemical impedance spectroscopy (EIS) on a symmetrical cell configuration consisting of the MC-BZY composite sandwiched by two identical silver-based electrodes and current collectors. The EIS measurements were carried out using an electrochemical workstation (IM6, Zahner) under open-circuit conditions within a frequency range of 10^5 to 0.01 Hz and under a 10 mV of stimulus AC amplitude. The ionic resistance was extracted from the high-frequency intersection of the spectrum with the real-axis. The temperature was varied from 400 to 650°C , covering the solid-to-liquid transition of the carbonate phase (the melting temperature of the carbonate phase is $\sim 490^\circ\text{C}$). To understand the nature of ionic conduction, the ionic conductivity was also measured in both oxidizing (air) and reducing atmospheres (H_2 - N_2 mixture) with a range of varied partial pressures of H_2O and H_2 . The different partial pressures of H_2O were generated by a homemade water bubbler system and monitored by an on-line humidity sensor (Vaisala model 332). To verify the involvement of protons in ionic conduction, D_2O was also used as an alternative to H_2O . In addition, the effects of MC loading and MC-type on ionic conductivity were also studied.

B1.3: DFT modeling of proton transfer in molten carbonates

The energetics of proton transfer in a MC was analyzed by Gaussian09 suite of quantum chemistry programs [10]. The disordered MC phase was simulated by a cluster of $(\text{Li}_2\text{CO}_3)_8$. The B3LYP hybrid functional [11, 12] in combination with the basis set of 3-21G(d, p) were used to calculate the energetics of H^+ -transfer in $[(\text{Li}_2\text{CO}_3)_8\text{H}]^+$ cluster.

B2: Results and Discussion

B2.1: XRD patterns and microstructures

The XRD patterns of BZY synthesized at 1500°C for 5 h is shown in Fig.1 (a), indicating two cubic phases, which have been previously reported [13]. The reactivity between BZY and LN was also studied by firing a mixture of BZY and LN (1:1 vol%) at 650°C for 2h. The XRD patterns are shown in Fig.1 (b), indicating no phases formed other than the original BZY and LN, which is consistent with that reported in Ref. [9]. Rietveld refinements of XRD patterns resulting from the pure BZY and BZY-LN indicated that the mole ratio of the two cubic BaZrO_3 phases was consistently 59:41. The two BaZrO_3 cubic phases exhibited a lattice parameter of $a=4.2021\text{\AA}$ and $a=4.2366\text{\AA}$, respectively. For the composite sample, the lattice parameters for the two BaZrO_3 cubic phases were $a=4.1999\text{\AA}$ and $a=4.2358\text{\AA}$, further suggesting no reaction occurred between BZY and molten carbonate.

The microstructures of BZY and MC-BZY composite are shown in Fig.2 (a) and (b), respectively. It is evident that BZY even after being sintered at 1500°C contains poorly connected grains, indicating the refractory nature of BZY materials. By contrast, Fig.2 (c) and (d) of the MC-BZY composite shows a dense microstructure with the MC phase filling the pores.

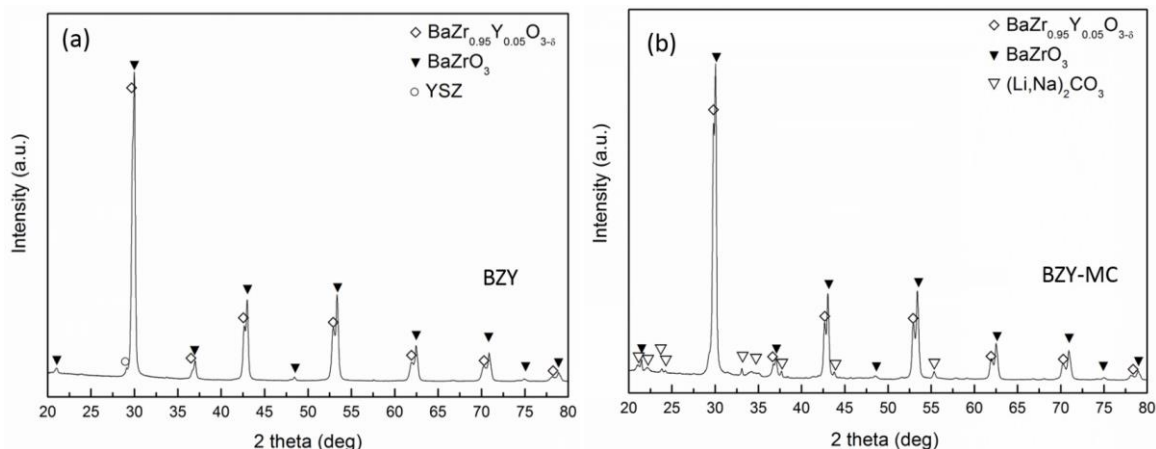


Fig.1 XRD pattern of (a) BZY sintered at 1500°C for 5h and (b) MC-BZY fired at 650°C .

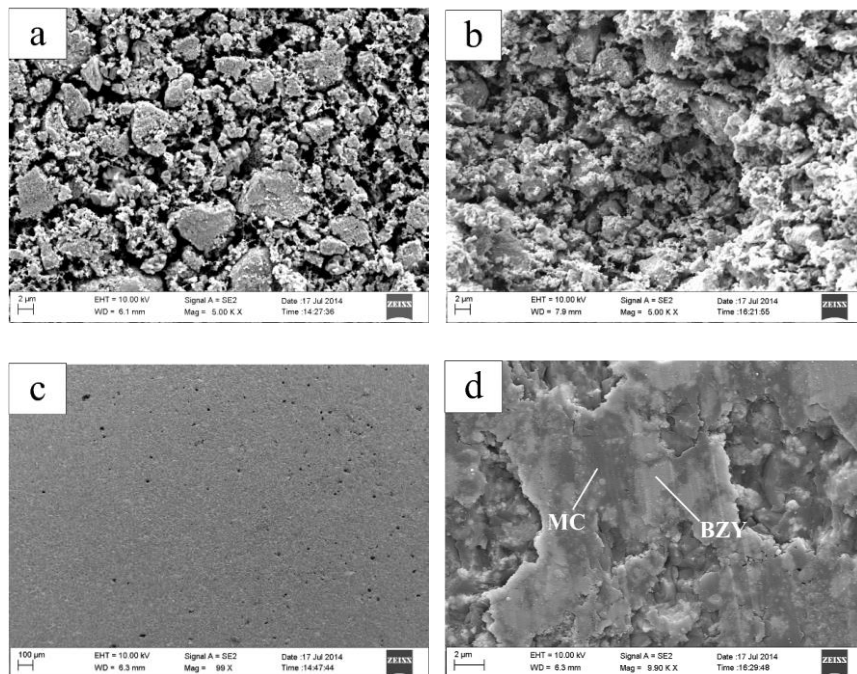


Fig.2 SEM images of (a) surface and (b) cross-section of BZY sintered at 1500°C; (c) surface and (d) cross-section of a LN-BZY composite prepared at 650°C.

B2.2: Conductivity vs MC loading

The effect of MC loading on the ionic conductivity of a LK-BZY is shown in Fig.3. Since the MC loading is determined by the initial porosity in BZY, different contents of carbon-black pore former were used during preparation of porous BZY. Fig.3 clearly indicates that higher MC loading (or higher initial porosity in BZY) results in a higher ionic conductivity over the entire temperature range tested. This is an expected result as the primary conductor in MC-BZY is the MC phase, which is also evidenced by the activation energy $E_a=0.29-0.30$ eV close to that of pure molten carbonate. In practice, however, the high conductivity of the MC phase could be limited by the amount of MC that can be retained within the BZY skeleton, analogous to the case of MC in LiAlO_2 matrix used in commercial molten carbonate fuel cells.

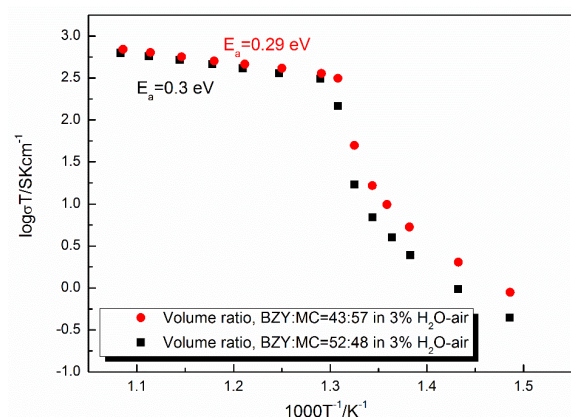


Fig.3 Ionic conductivity vs temperature in LK-BZY composites at different MC loadings

B2.3: Conductivity vs MC type

The effect of MC type, *i.e.* LK vs LN, on ionic conductivity of MC-BZY is shown in Fig.4. To ensure a fair comparison, the MC loading of the two samples was fixed at 48 vol%. Clearly, LN-BZY has a higher conductivity than LK-BZY at $t > 500^\circ\text{C}$. This observation is consistent with the literature showing higher conductivity for LN than LK system [14]. In addition, $E_a = 0.30$ and 0.40 eV at above the melting temperature for the LN-BZY and LK-BZY system, respectively, are comparable to the literature values [14]. The LN system was selected for the subsequent electrical characterization because of its high conductivity.

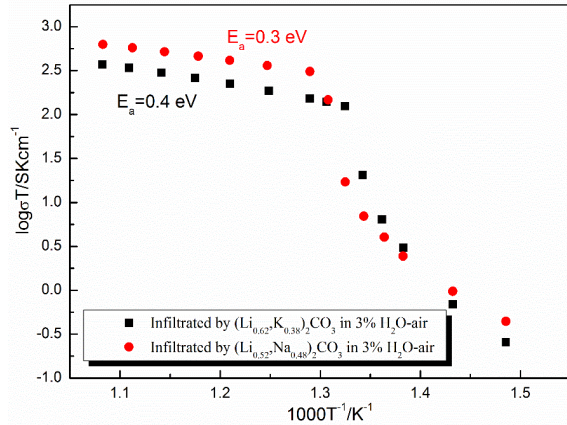


Fig.4 Conductivity comparison of a LK-BZY and LN-BZY vs temperature in 3% H_2O -air.

B2.4: Conductivity vs atmosphere

Fig.5 shows the conductivity of a LN-BZY with a MC loading of 57 vol% measured in both oxidizing and reducing atmospheres. It is evident that conductivity measured in reducing 3% H_2O -(5% H_2 - N_2) is higher than that measured in oxidizing 3% H_2O -air over the entire temperature range. The result suggests that the enhanced conductivity by H_2 be associated with the MC phase since the BZY's conductivity above the melting temperature is negligible compared to the MC phase. The almost identical activation energy between the LN-BZY and pure LN shown in Fig.5 supports this assertion.

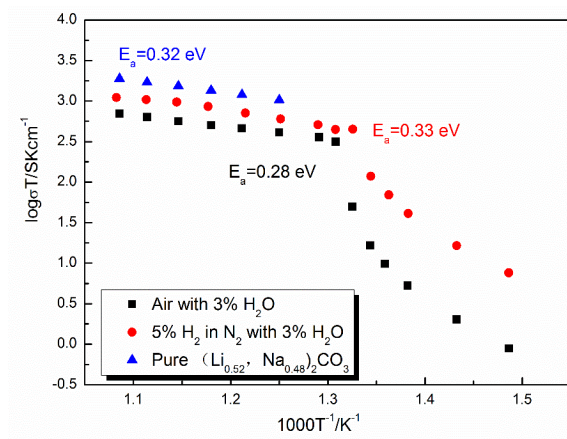
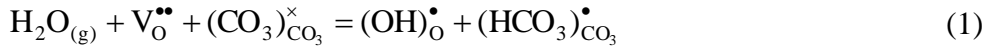


Fig.5 Conductivity vs temperature of a LN-BZY composite measured in 3% H_2O -air and 3% H_2O -(5% H_2 - N_2)

B2.5: Conductivity vs P_{H_2O}

To further investigate the feasibility of proton conduction, the conductivity of a LN-BZY composite with a MC loading of 57 vol% was measured as a function of partial pressure of H_2O (P_{H_2O}) at 600°C; the results are shown in Fig.6. First, the conductivity in reducing 5% H_2 - N_2 is nearly twice as high as that in air under each P_{H_2O} , which agrees with Fig.5 measured under $P_{H_2O}=0.03$ atm. Second, the conductivity increases with P_{H_2O} . Third, the dependence of conductivity on P_{H_2O} is almost the same for the two gas compositions. These observations again suggest that the proton conduction be associated with the MC phase and protons be originated from either H_2O or H_2 or both.

From a defect chemistry perspective, the enhanced proton conductivity by H_2 and H_2O can be understood by the following reaction (in Kröger-Vink notation):



Here $V_O^{\bullet\bullet}$ denotes oxygen vacancies in BZY, serving as the charge compensation carriers; $(OH)_O^{\bullet}$ represents hydroxyl defect residing on oxygen lattice of BZY; $(CO_3)_{CO_3}^{\times}$ is a regular carbonate-ion; $(HCO_3)_{CO_3}^{\bullet}$ is the new proton conducting species residing on carbonate-ion. From reaction (1), it is evident that increasing partial pressure of H_2O can increase the concentrations of $(OH)_O^{\bullet}$ and $(HCO_3)_{CO_3}^{\bullet}$, ultimately leading to an increase in conductivity by protons. It is also inferred from Fig.6 that $(HCO_3)_{CO_3}^{\bullet}$ residing on carbonate-ion is the dominant charge carrier for proton conduction. It is worth mentioning that reaction (1) implicates a synergetic proton transfer between BZY and MC, in which both $V_O^{\bullet\bullet}$ and $(CO_3)_{CO_3}^{\times}$ play an important role. The details on the proton transfer mechanism will be discussed in the following.

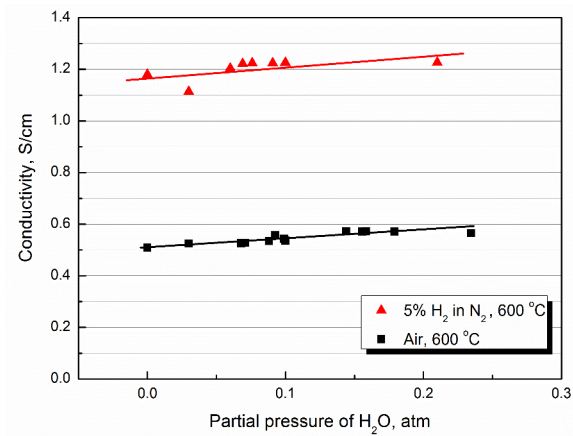
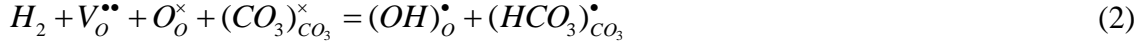


Fig.6 Conductivity of a LN-BZY composite vs P_{H_2O} at 600°C.

B2.6: Conductivity vs P_{H_2}

To understand the enhanced conductivity by H_2 , the conductivity of LN-BZY composite was measured over a range of partial pressure of H_2 (P_{H_2}) at 600°C; the result is shown in Fig.7. Note

that the conductivity shown in Fig.7 is lower than that in Fig.6. This is caused by a lower MC loading in the sample, *viz.* 48 vol% for Fig.7 vs 57 vol% for Fig.6. The defect chemistry reaction leading to the increased concentrations of $(OH)_O^\bullet$ and $(HCO_3)_{CO_3}^\bullet$, and thus the conductivity can be expressed by:



here O_O^\times is the regular oxygen lattice in BZY. Again, $(HCO_3)_{CO_3}^\bullet$ is the dominant charge carrier over $(OH)_O^\bullet$ because MC is the primary ionic conductor at 600°C. The synergy of proton transfer between BZY and MC phase is further discussed in the following.

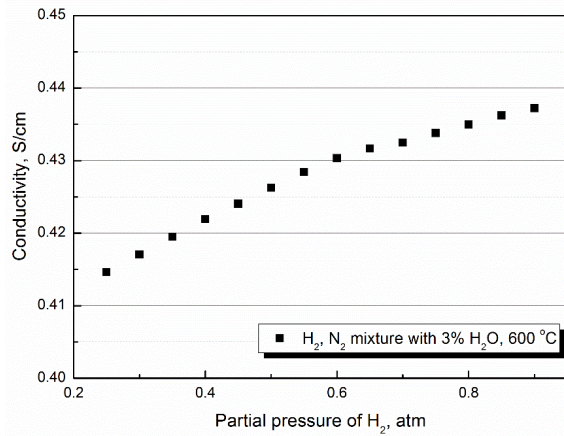


Fig.7 Conductivity of a LN-BZY composite vs P_{H2} at 600°C

B2.7: Conductivity in D₂O

To verify whether H in H₂O is one of the proton sources, we measured conductivity in the presence of D₂O. Fig.8 compares the conductivities measured in air saturated with 3% H₂O and 3% D₂O. The conductivity difference for the two gases is small but visible, suggesting the nature of proton conduction. As aforementioned, proton species $(HCO_3)_{CO_3}^\bullet$ is the primary source for the observed enhanced conductivity in both H₂O and H₂ containing atmospheres. The close E_a to pure LN shown in Fig.8 further indicates the dominance of ionic conduction by the molten carbonate phase.

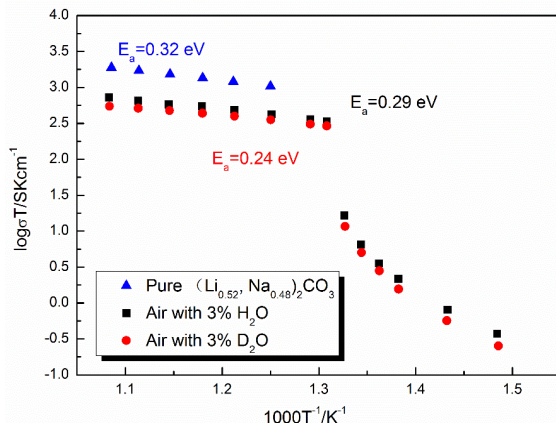


Fig.8 Conductivity of a LN-BZY vs temperature in 3% H₂O-air and in 3% D₂O-air.

B2.8: DFT modeling of proton transfer in molten carbonates

To understand the theoretical feasibility of proton conduction in molten carbonates, we performed a first-principles DFT calculation of the energetics of proton transfer in a molten carbonate phase. Fig.9 shows the energetics of proton transfer intrinsic reaction coordinate (IRC) across a cluster of Li_2CO_3 (Fig.9 (a)), a surrogate for molten carbonate for the DFT calculations. The H^+ marked in green color bonds with O5 as the reactant and bonds with O20 as the product. The IRC calculations specify that the H^+ first rotates counter-clockwise along the O5 to reach the TS. During this process, the bond between H^+ and O5 is slightly shortened from 1.070 Å to 1.030 Å with an energy barrier of 8.9 kcal/mol. The conversion from TS into product is rather fast. The H^+ separates from O5 and moves towards O20. Meanwhile, the bond length of H^+ -O5 increases from 1.030 Å to 1.267 Å, whereas the bond length of H^+ -O20 reduces from 2.933 Å to 1.174 Å, thus completing a single H^+ -transfer process. In addition, it is also seen from Fig.9 (b) that 53.1 kJ/mole energy is needed to overcome for a reversible transition from product to reactant, which further implies that continuous H^+ -transfer in $(\text{Li}_2\text{CO}_3)_8$ cluster or molten carbonate is feasible.

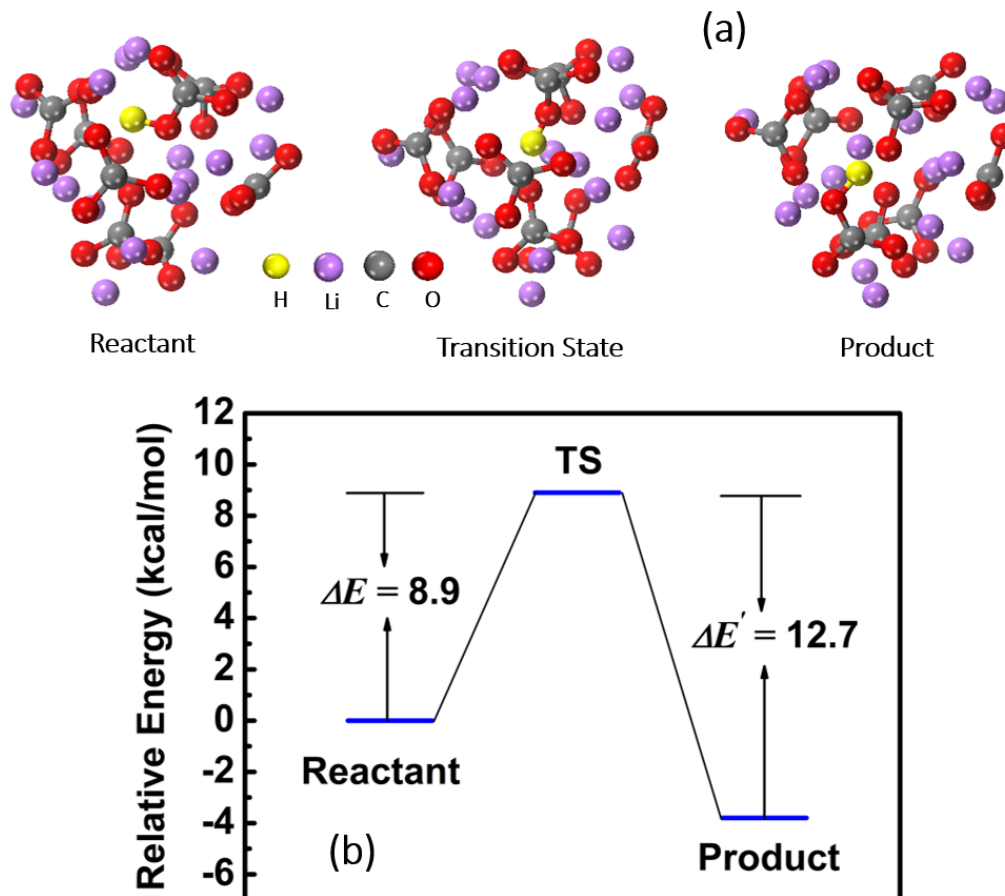


Fig.9 The energetics of proton transfer in cluster of $(\text{Li}_2\text{CO}_3)_8$; (a) cluster structure; (b) the relative energies vs IRC. Unit: kcal/mole

B2.9: A synergetic proton transfer mechanism

As indicated by reaction (1) and (2), the creation of proton species $(HCO_3)_{CO_3}^\bullet$ relies upon the presence of $V_o^{\bullet\bullet}$ and O_o^\times in the BZY. In other words, proton transfer across the composite is synergetic between BZY and MC. To illustrate the mechanism, Fig.10 shows a schematic of the synergetic proton transfer in the atmospheres containing H_2O or H_2 or both. It is worth reemphasizing that $(HCO_3)_{CO_3}^\bullet$ is considered the primary proton conducting species accompanying the major carbonate-ion conduction in the MC-BZY composite electrolyte.

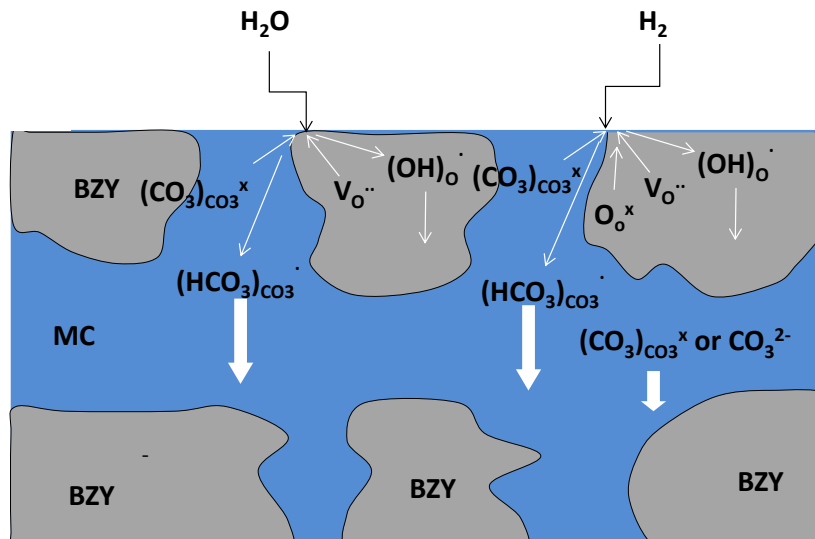


Fig.10 Schematic of synergetic proton conduction in MC-BZY composite electrolyte

B3: Conclusion and Summary for Part B

In summary, electrical properties of the MC-BZY composite electrolyte was methodologically evaluated to understand the enhanced conductivity and improved SOFC performance. It was shown that the composite can be made into a dense membrane at 650°C by filling the pores in BZY with MC phase. The ionic conductivity of the composite above 500°C was affected by the loading and type of MC. More important, the sample exposed in H_2 -containing atmospheres exhibited nearly twice the conductivity of the one in air. The dependences of conductivity on partial pressures of H_2 and H_2O , as well as the type of H (H vs D) suggested that proton conduction take places, primarily in the MC phase. A defect chemistry model was presented to explain the synergetic proton transfer between BZY and MC phases. A preliminary first-principles DFT calculation further confirmed that proton transfer in molten carbonate was indeed a low-energy barrier process.

B4: References

1. K.-Y. Park, Y. Seo, K. B. Kim, S.-J. Song, B. Park and J.-Y. Park, Journal of Alloys and Compounds **639** (0), 435-444 (2015).
2. P. Babilo, T. Uda and S. M. Haile, J. Mater. Res. **22** (5), 1322-1330 (2007).

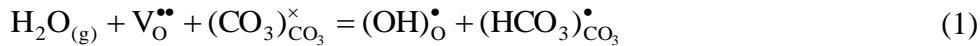
3. F. Iguchi, T. Yamada, N. Sata, T. Tsurui and H. Yugami, *Solid State Ionics* **177** (26-32), 2381-2384 (2006).
4. K. Katahira, Y. Kohchi, T. Shimura and H. Iwahara, *Solid State Ionics* **138** (1,2), 91-98 (2000).
5. J. Dailly and M. Marrony, *Journal of Power Sources* **240**, 323-327 (2013).
6. K. Xie, R. Yan, X. Chen, S. Wang, Y. Jiang, X. Liu and G. Meng, *J. Alloys Compd.* **473** (1-2), 323-329 (2009).
7. X. Li, N. Xu, L. Zhang and K. Huang, *Electrochemistry communications* **13** (7), 694-697 (2011).
8. Y. Hei, J. Huang, C. Wang and Z. Mao, *International Journal of Hydrogen Energy* (2014).
9. K.-Y. Park, T.-H. Lee, J.-T. Kim, N. Lee, Y. Seo, S.-J. Song and J.-Y. Park, *J. Alloys Compd.* **585**, 103-110 (2014).
10. M. J. Frisch, G. W. Trucks, H. B. Schlegel, G. E. Scuseria, M. A. Robb, J. R. Cheeseman, G. Scalmani, V. Barone, B. Mennucci, G. A. Petersson, H. Nakatsuji, M. Caricato, X. Li, H. P. Hratchian, A. F. Izmaylov, J. Bloino, G. Zheng, J. L. Sonnenberg, and etc. al, (Gaussian, Inc., Wallingford, CT, USA, 2009).
11. C. Lee, W. Yang and R. G. Parr, *Phys. Rev. B: Condens. Matter* **37** (2), 785-789 (1988).
12. A. D. Becke, *Phys. Rev. A: Gen. Phys.* **38** (6), 3098-3100 (1988).
13. S. Tao and J. T. S. Irvine, *Journal of Solid State Chemistry* **180** (12), 3493-3503 (2007).
14. T. Kojima, Y. Miyazaki, K. Nomura and K. Tanimoto, *J. Electrochem. Soc.* **160** (10), H733-H741 (2013).

PART C: PROTON MIGRATION AT THE BZY AND MC INTERFACE

C1: Introduction

A focus of the recent development of solid oxide fuel cell (SOFC) technology towards commercialization is to lower SOFC's operating temperature from the current 700-800°C to below 600°C. One key to realize such reduced temperature SOFCs is to discover and employ a high-conductivity solid-oxide electrolyte. One promising class of solid oxide electrolytes is BaMO₃ (M=Zr, Ce) based perovskite protons (H⁺) conductors¹⁻⁸. Unlike conventional intrinsic H⁺-conductors such as H₃PO₄, these oxide-based H⁺-conductors strongly rely on the oxygen-vacancy (V_O^{••}) and its interactions with H₂O to produce H⁺-carrying species of OH_O[•], which is known as the “Grotthuss mechanism”⁹. Since the hydration reaction is exothermic, lower temperatures favor the formation of OH_O[•], thus proton conductivity. This fundamental fact is interestingly synergetic with low-temperature SOFCs, making BaMO₃-based materials a promising low-temperature solid electrolyte candidate.

BaZr_{0.8}Y_{0.2}O_{2.95} (BZY) is a representative of well-studied oxide-based proton conductors with reasonably high conductivity⁴⁻⁸. Compared with its counterpart BaCeO₃, BZY attracts much more attention due to its chemical stability in CO₂-containing atmospheres. However, it is hard to sinter it into a dense microstructure, rendering difficulties for practical use. Recently, we showed that molten carbonate (MC) salts infiltrated into BZY can help produce a dense microstructure¹⁰⁻¹¹. More interestingly, such a dual-phase electrolyte exhibited enhanced proton conductivity. Similar results have also been observed by other groups with excellent SOFC performance¹²⁻¹³. In an effort to understand this phenomenon, we proposed that OH_O[•] derived from V_O^{••} transfers H⁺ to the neighboring carbonate-ion (CO₃)_{CO₃}^x, forming a new proton species (HCO₃)_{CO₃}[•] in MC phase¹⁰⁻¹¹, through the following defect reaction (in Kröger-Vink notation):



A subsequent DFT modeling revealed that proton migration in the form of (HCO₃)_{CO₃}[•] within a MC phase is a very facile process with low energy barrier¹⁴. However, how H⁺ is transferred across the interface of BZY/MC as suggested by reaction (1) remains ambiguous at this point despite the fact that a range of computational modeling work on H⁺ migration and stability in BaMO₃-based proton conductors has been reported in the open literature¹⁵⁻¹⁸.

In the present work, we aim to understand the energetics of proton migration across the BZY/MC interface from a DFT perspective. Pathways and energetics of proton migration at the ZrO₂-terminated surface (100) of a pure BZ (BZ: BaZrO₃) and a BZ with MC are particularly computed and compared. The results clearly suggest that the presence of MC can significantly enhance the H⁺ migration across the surface of BZ (and BZY).

C2: Computational method and model

All DFT calculations conducted in this study were performed using a Vienna *ab initio* simulation package (VASP)¹⁹⁻²⁰ with the projector augmented wave (PAW) approach²¹⁻²². The exchange-correlation term of electrons was described by the Perdew-Burke-Ernzerhof (PBE) functional²³. For all surface calculations, a 4×4×1 Monkhorst-Pack sampling of the Brillouin zone was used²⁴. A vacuum region of 15 Å in the z-axis direction was created to prevent any interaction between

cells. The O $2s^2 2p^4$, C $2s^2 2p^2$, Zr $4s^2 4p^6 5s^2 4d^2$, $4s^2 4p^6 5s^2 4d^1$ of Y, and Ba $5s^2 5p^6 6s^2$ were taken as the valence electron configurations in the calculations. To ensure a high accuracy, a cutoff energy of 500 eV was chosen for the plane waves. During the structural optimization, all atoms were fully relaxed with a force less than 0.02 eV/Å. Furthermore, the D2 method of Grimme²⁵ was applied to calculate the dispersion interaction between carbonate-ion and surface, in which the cutoff radius for pair interactions, global scaling factor optimized at the PBE and damping parameter were taken as 15.0 Å, 0.75 and 20.0, respectively. The saddle points and migration pathways with the minimum energy were sought by the nudged elastic band (NEB) method²⁶. For all the calculations, spin-polarized and dipole corrections have also been taken into account.

Calculations on energetics and pathways of proton migration were conducted on an 8-layer asymmetrical slab at the ZrO₂-terminated (100) surface. The (100) surface was selected because it has been previously determined to be the most stable surface for BaZrO₃²⁷⁻²⁸. An asymmetrical slab was chosen to maintain a stoichiometric and neutral unit cell, which is an acceptable approach in the study of similar systems. For example, Evarestov *et al*²⁹ showed a negligible difference in surface energy between an asymmetric and symmetric LaMnO₃ (110) surface slab. Liu *et al* used an 8-layer asymmetric LaMnO-terminated LaMnO₃ (110) surface slab in Ref 30. Furthermore, previous studies have shown that a total of 8 layers are sufficient to simulate the surface processes on BaZrO₃^{27-28, 31-32}. In the current model, the bottom 4 layers were fixed to represent the bulk of BaZrO₃, whereas the top 4 layers were relaxed and considered as the domain for adsorbed H⁺ and CO₃²⁻. On the other hand, with a ZrO₂-terminated surface, H⁺ can be modeled to migrate along the edge of a ZrO₆ octahedron, which has been previously determined as a favorable pathway³³.

C3: Results and Discussion

C3.1: Adsorption of proton on the ZrO₂-terminated surface

We started calculations by first optimizing the bulk structure with a $6 \times 6 \times 6$ k-point mesh using the computational methods described above. The calculated lattice constant of a cubic BaZrO₃ is 4.25 Å, which is in good agreement with the experimental 4.20 Å³⁴ and theoretical 4.24 Å²⁷. The adsorption behavior of a single proton on the ZrO₂-terminated surface was then studied. A total of five adsorption sites were considered and are schematically shown in Fig.1: (a) on the top of O atom (upright), **To**, (b) on the top of O atom (tilted to Zr atom), **To-zr**, (c) on the top of O atom (tilted to hollow site), **To-hollow**, (d) on the top of Zr atom, **T_{Zr}**, and (e) on the top of hollow site, **T_{hollow}**. After a full relaxation, the **To-hollow** configuration (c) is calculated to be the most favorable adsorption site with the lowest energy, indicating that the proton prefers to be on the top of O and tilted to the hollow site. This finding is in agreement with previous understanding on the formation of proton defects, where water from the gas phase dissociates into a hydroxide ion and a proton. The former will then fill an oxygen vacancy, while the latter forms a covalent bond with the lattice oxygen⁹. Moreover, Fig.1 (c) also indicates that the lattice oxygen deviates from its lattice position to the hollow site and that the proton tilts to the hollow site, shortening the distance between proton and its neighboring oxygen. Therefore, this geometry is in favor of the proton migration from an O to its adjacent O, so will reduce the energy barrier of proton transfer.

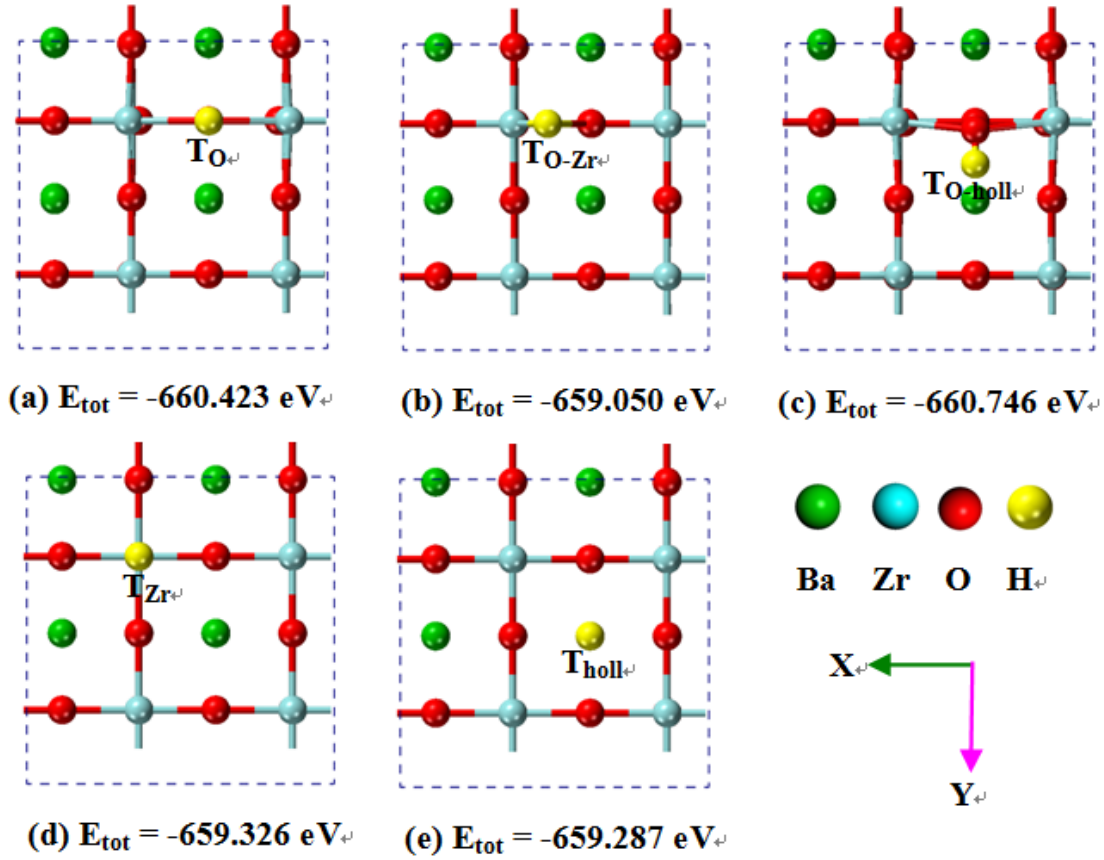
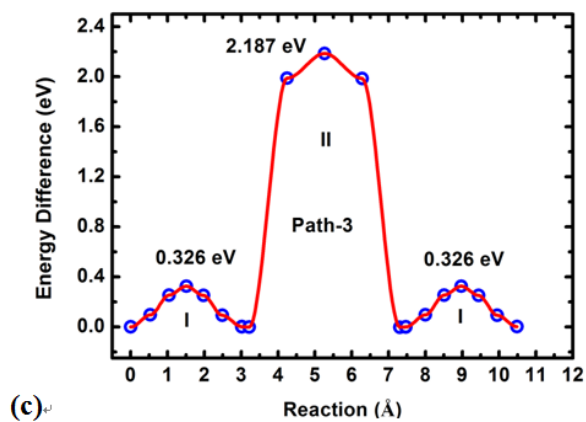
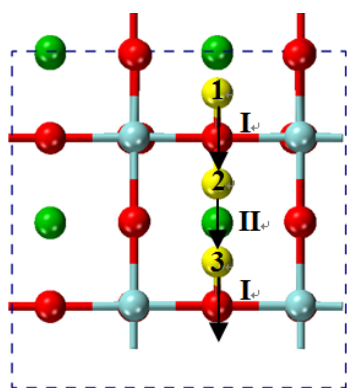
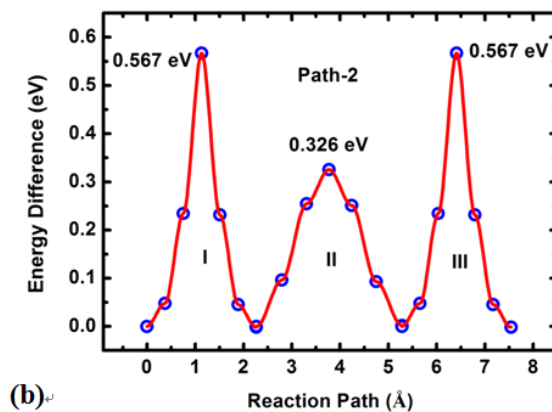
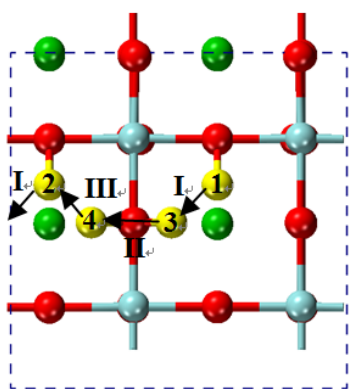
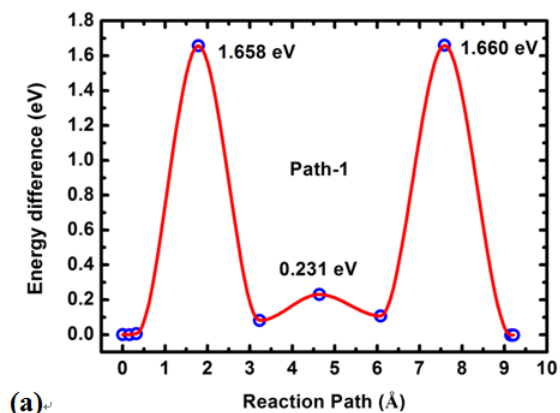
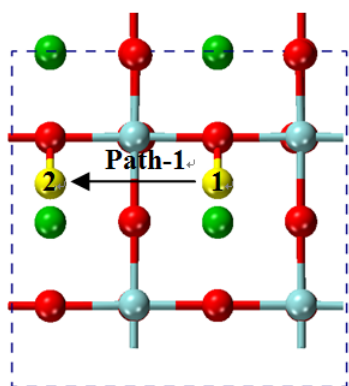


Fig.1 Optimized structures (top view) and total energy of proton adsorbed on the ZrO_2 -terminated surface. (a) on the top of O atom (upright), T_{O} , (b) on the top of O atom (tilted to Zr atom), $\text{T}_{\text{O-Zr}}$, (c) on the top of O atom (tilted to hollow side), $\text{T}_{\text{O-hollow}}$, (d) on the top of Zr atom, T_{Zr} , and (e) on the top of hollow site, T_{hollow} .

C3.2: Proton migration on the ZrO_2 -terminated surface

Next, selected migration pathways and their corresponding energy barriers for the proton migration on the ZrO_2 -terminated (100) surface were studied. **Fig.2** shows the migration pathways and energy profiles of H^+ along X-direction (a to b), Y-direction (c to d), and XY direction (e). For the X-direction, two independent migration pathways are possible: linear path 1 \rightarrow 2 (labeled as “Path-1”) with the shortest migration distance and curved path from 1 \rightarrow 3 \rightarrow 4 \rightarrow 2 (labeled as Path-2). These two migration pathways and the corresponding energetics are shown in **Fig.2 (a) and (b)**, respectively. “Path-1” includes one-step migration and experiences an energy barrier of 1.660 eV. “Path-2” consists of three steps, marked as I, II, and III. The step I and III are related to H^+ transfer from an oxygen toward a neighboring oxygen with the bond breaking and reforming of O-H^+ . The step II involves only H^+ rotation around an oxygen with the O-H^+ bond connected. The energy barriers of H^+ transfer and rotation are 0.567 eV and 0.326 eV, respectively. Therefore, the overall energy barrier for “Path-2” is 0.567 eV, which is in agreement with the activation energy of 0.69 eV for H^+ transfer observed in BaZrO_3 ¹⁷, mobility activation enthalpies of 0.41-0.63 eV for protonic defects in cubic perovskite-type oxides³⁵, activation energy of 0.3-0.6 eV³³ and 0.45-0.65 eV³⁶ for H^+ migration in BZY electrolytes. Evidently, the proton transfer is the rate-determining step, which agrees well with the

experimental and other computational results ^{17-18, 37-38}. Overall, the results show that proton migration preferentially favors a curved over a straight pathway.



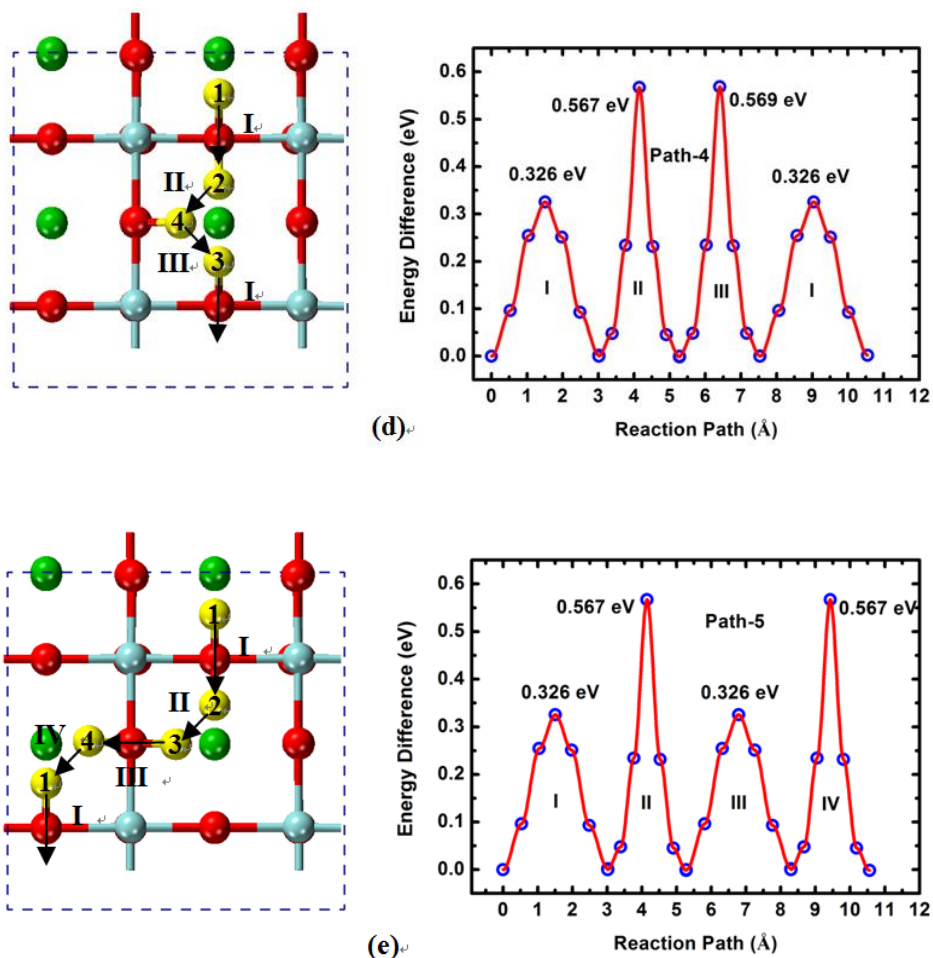


Fig.2 Migration pathways and energy profiles for H⁺ migration along X direction (a to b), Y direction (c to d), and XY direction (e). The migration pathways are marked with arrows.

Fig.2 (c) and (d) show two more different migration pathways, labeled as “Path-3” and “Path-4”, for H⁺ migration along the Y-direction. These two pathways represent H⁺ migration along a linear and zigzag pattern, respectively. Fig.2 (c) shows that “Path-3” follows migration sequence 1 → 2 → 3 → 1, consisting of a H⁺ rotation step (I) followed by a transfer step (II) via the top of hollow site. The former needs to overcome an energy barrier of 0.326 eV, while a much higher energy barrier of 2.187 eV for the latter. The high energy profile suggests that H⁺ migration via this pathway be energy prohibitive. Fig.2 (d) shows the “Path-4” via 1 → 2 → 4 → 3 → 1, consisting of a H⁺ rotation step (I) followed by two transfer steps (II, III). The highest energy barrier for H⁺ migration is 0.569 eV, indicating that the zigzag pathway is the favorable route for H⁺ migration.

From the symmetry viewpoint, we also consider XY-direction as the “Path-5” for H⁺ migration. Fig.2 (e) shows “Path-5” following a migration sequence of 1 → 2 → 3 → 4 → 1, which consists of two H⁺ rotation steps (I and III) and two H⁺ transfer steps (II and IV). The highest energy barrier for this type of H⁺ migration is 0.567 eV, also indicating a favorable pathway.

Based on the DFT analysis above, we now can conclude that H⁺ migration on the ZrO₂-terminated (100) surface of BaZrO₃ favors a curved pathway, involving both transfer and rotation of proton conduction mechanism.

C3.3: Proton migration on the ZrO_2 -terminated surface with Y-doping

For practical use, Y-doping on Zr-site of BaZrO_3 is necessary to introduce oxygen vacancies, and the latter is the source of proton species $\text{OH}_\text{O}^\bullet$. The model for the ZrO_2 -terminated (100) surface with an yttrium on the Zr-site is shown in Fig.3 (a). We assumed that an oxygen vacancy will be created next to yttrium and this allows to examine its effect on energy barrier of H^+ migration.

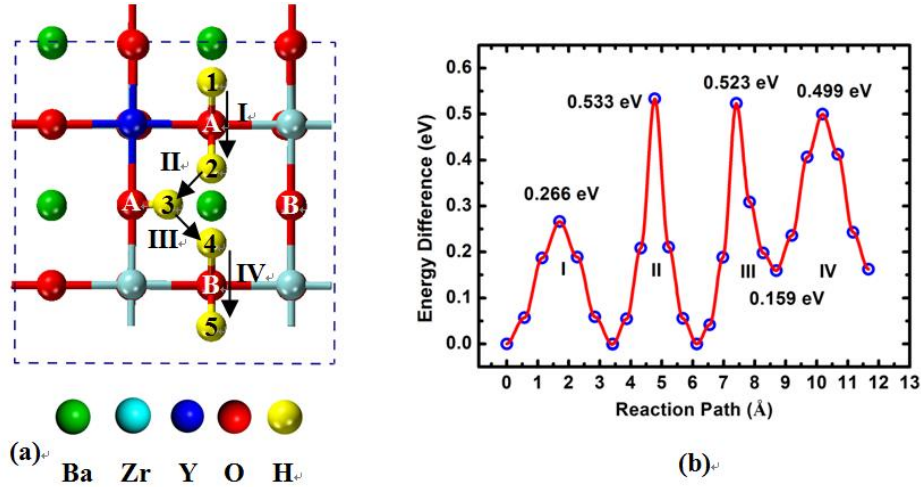


Fig.3 Migration pathways and energy profiles for H^+ -migration along Y direction at Y-doped ZrO_2 -termination surface (100). The migration pathways are marked with arrows.

According to the coordination environment, two types of O, denoted as A and B, are identified in the model. The A-type O bonds with Y to form a half YO_6 octahedron on the surface, while the B-type O bonds with Zr to form another half ZrO_6 octahedron on the surface. To compare with the energy barriers of H^+ migration on a perfect surface of ZrO_2 , H^+ migration along Y-direction (“Path-4”) at the defective surface was examined. The migration pathway via $1 \rightarrow 2 \rightarrow 3 \rightarrow 4 \rightarrow 5$ includes four steps: step I and IV represent H^+ rotation around A-and B-type O, respectively; step II and III represent H^+ transfer between two A-type O and between A-and B-type O, respectively. Energy barriers of the four migration steps are given in Fig.3 (b), with 0.266, 0.533, 0.523, and 0.340 eV for step I, II, III and IV, respectively. The total energy barrier for H^+ migration along this pathway is, therefore, 0.533 eV, which is not significantly different from 0.567 eV of the perfect surface, implying that the effect of yttrium on the energy barrier of H^+ migration on the surface is negligible. Therefore, the following DFT calculations of MC effect on H^+ migration were primarily conducted on a perfect BZ surface with ZrO_2 -termination.

C3.4: Proton migration at the ZrO_2 -terminated surface/MC interface

To understand the observed enhanced proton conductivity of BZY by MC, we further calculated the energy barrier of H^+ migration at the interface consisting of a ZrO_2 -terminated (100) surface and MC using the method described above. The H^+ migration along the Y-direction (“Path-3”) was used as an example for illustration purpose. Fig.4 shows the pathway considered and energy barriers calculated for H^+ migration, where (a) and (b) are the side and top view, respectively, and (c) is the energetics calculated for each migration step. The pathway consists of four individual steps: $1 \rightarrow 2 \rightarrow 3 \rightarrow 4 \rightarrow 1$. Step I ($1 \rightarrow 2$) is the H^+ rotation around an O of the ZrO_2 -terminated surface; step II ($2 \rightarrow 3$) is the H^+ transfer from surface to CO_3^{2-} , step III ($3 \rightarrow 4$) is

H^+ rotation around an O of CO_3^{2-} , and finally, step IV ($4 \rightarrow 1$) is H^+ transfer from CO_3^{2-} back to surface. It is interesting to see that during the whole process of H^+ migration, CO_3^{2-} links position “2” to “1” like a bridge lying above the hollow site. Fig.4 (c) displays that energy barriers for step I, II, III and IV are 0.326, 0.281, 0.332, and 0.061 eV, respectively. The highest energy barrier is 0.332 eV, suggesting that the step-III of H^+ rotation around O in CO_3^{2-} is the rate-limiting step, whereas H^+ transfer between surface and CO_3^{2-} is relatively easy with a low energy barrier. The energy barrier of 0.332 eV for H^+ migration is in excellent agreement with 0.33 eV obtained from the conductivity measurement of a BZY-MC composite¹¹. Compared to the results shown in Fig.3, the presence of CO_3^{2-} on the surface of $BaZrO_3$ has significantly reduced the energy barrier for H^+ migration from 0.567 eV to 0.332 eV. Overall, the calculations confirm that MC provides an alternative easy pathway for protons to travel along the surface of BZY. The observed enhanced proton conductivity in BZY/MC composite is, therefore, the result of a facile proton exchange between BZY and MC phase along the interface.

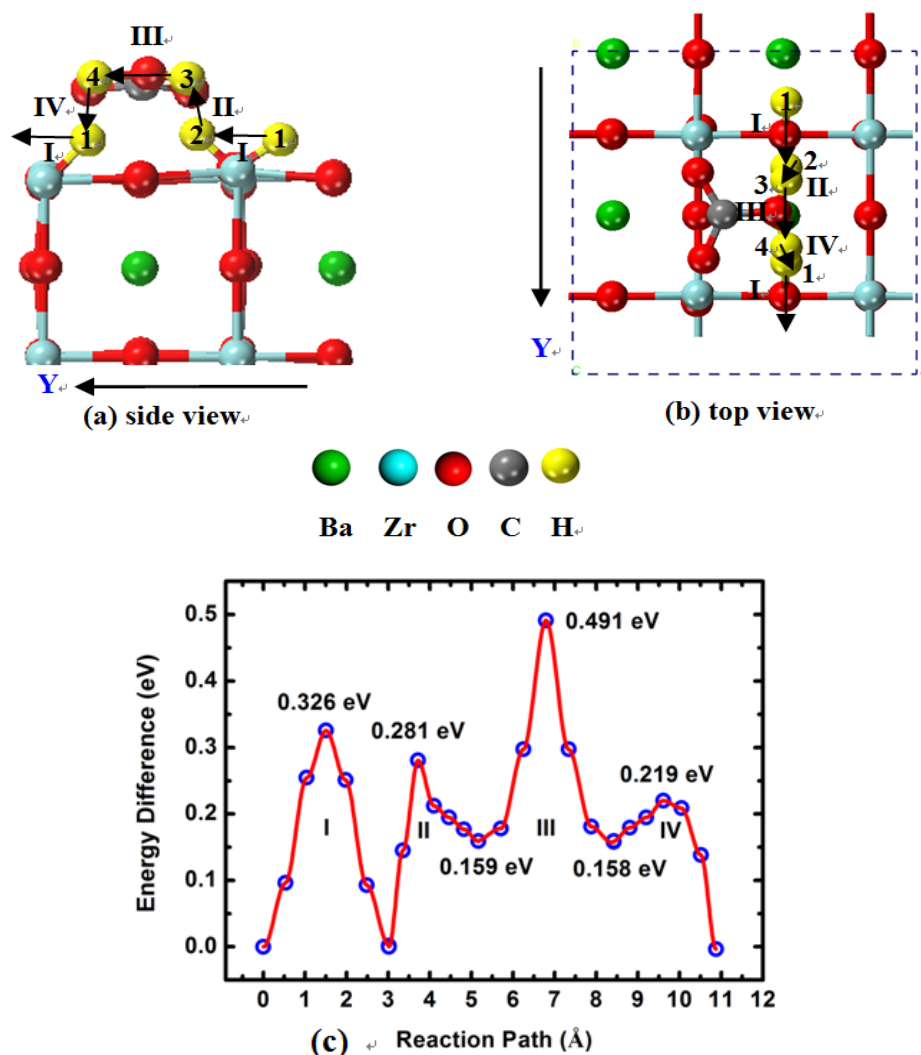


Fig.4 Migration pathways and energy profiles (c) for proton migration along Y direction with the aid of molten carbonate (MC), (a) is side view and (b) is top view. The migration pathways are marked with arrows.

C4: Conclusion

In summary, we have for the first time studied proton migration at the interface of BaZr(Y)O₃ and molten carbonate by density functional theory calculations. Proton migration along the ZrO₂-terminated (100) surface of BaZrO₃ favors a curved path with an energy barrier of 0.567 eV. In the presence of carbonate-ion, the energy barrier is significantly reduced to 0.332 eV, which is in excellent agreement with 0.33 eV of activation energy observed in conductivity measurement. The rate-determining step is the proton transfer with the absence of MC, whereas it becomes the proton rotation around oxygen in carbonate-ion in the presence of MC. In addition, the effect of Y-doping on the energy barrier for proton migration on surface is insignificant (0.567 eV for BZ surface vs 0.533 eV for BZY surface). Overall, the enhanced proton conductivity in BZY-MC composite electrolyte is attributed to the facile interfacial proton exchange between BZY and MC phase.

C5: REFERENCES

- (1) Katahira, K.; Kohchi, Y.; Shimura, T.; Iwahara, H. *Solid State Ionics* **2000**, 138 (1-2), 91–98.
- (2) Dailly, J.; Marrony, M. *J. Power Sources* **2013**, 240, 323–327.
- (3) Xie, K.; Yan, R.; Chen, X.; Wang, S.; Jiang, Y.; Liu, X.; Meng, G. *J. Alloys Compd.* **2009**, 473 (1-2), 323–329.
- (4) Park, K.-Y.; Seo, Y.; Kim, K.-B.; Song, S.-J.; Park, B.; Park, J.-Y. *J. Alloys Compd.* **2015**, 639, 435–444.
- (5) Iguchi, F.; Yamada, T.; Sata, N.; Tsurui, T.; Yugami, H. The influence of grain structures on the electrical conductivity of a BaZr_{0.95}Y_{0.05}O₃ proton conductor, *Solid State Ionics* **2006**, 177, 2381–2384.
- (6) Babilo, P.; Uda, T.; Haile, S. M. *Mater. Res.* **2007**, 22, 1322.
- (7) Tao, S. W.; Irvine, J. T. S. *J. Solid State Chem.* **2007**, 180, 3493.
- (8) Yamazaki, Y.; Hernandez-Sanchez, R.; Haile, S. M. *Chem. Mater.* **2009**, 21, 2755.
- (9) Nowick A. S. and Du, Y. *Solid State Ionics* **1995**, 77, 137–146.
- (10) Li, X.; Xu, N.; Zhang, L.; Huang, K. *Electrochem. Commun.* **2011**, 13 (7), 694–697.
- (11) Xiong, X.; Lei, X.; Zhang, C.; Wang, J.; Huang, K. *Solid State Ionics* **2015**, 279, 66–71.
- (12) Hei, Y.; Huang, J.; Wang, C.; Mao, Z. *Int. J. Hydrogen Energy* **2014**, 39, 14328.
- (13) Park, K.-Y.; Lee, T.-H.; Kim, J.-T.; Lee, N.; Seo, Y.; Song, S.-J.; Park, J.-Y. *J. Alloys Compd.* **2014**, 585, 103–110.
- (14) Lei, X.; Qin C. and Huang, K. *RSC Adv.* **2015**, 5, 56205.
- (15) Dawson, J. A.; Miller, J. A. and Tanaka, I. *Chem. Mater.* **2015**, 27, 901–908.
- (16) Tauer, T.; O’Hayre, R. and Medlin, J. W. *Chem. Mater.* **2014**, 26, 4915–4924.
- (17) Münch, W.; Seifert, G.; Kreuer K. D. and Maier, J. *Solid State Ionics* **1997**, 97, 39–44.
- (18) Münch, W.; Seifert, G.; Kreuer K. D. and Maier, J. *Solid State Ionics* **1996**, 86–88, 647–652.
- (19) Kresse, G.; Hafner, J. *Phys. Rev. B*, **1993**, 47, RC558-561.

- (20) Kresse, G.; Furthmüller, J. *Phys. Rev. B*, **1996**, *54*, 11169-11186.
- (21) Blöchl, P. E. *Phys. Rev. B*, **1994**, *50*, 17953-17979.
- (22) Kresse, G.; Joubert, D. *Phys. Rev. B*, **1999**, *59*, 1758-1775.
- (23) Perdew, J. P.; Burke, K.; Ernzerhof, M. *Phys. Rev. Lett.*, **1996**, *77*, 3865–3868.
- (24) Monkhorst H. J.; Pack J. D. *Phys. Rev. B* **1976**, *13*, 5188-5192.
- (25) Grimme S. *J. Comp. Chem.* **2006**, *27*, 1787.
- (26) Enkelman, G.; Beruaga, B. P.; Jónsson, H. *J. Chem. Phys.* **2000**, *113*, 9901.
- (27) Heifets, E.; Ho, J.; Merinov B. *Phys. Rev. B* **2007**, *75*, 155431.
- (28) Ho, J.; Heifets, E.; Merinov, B. *Surf. Sci.* **2007**, *601*, 490.
- (29) Evarestov, R. A.; Kotomin, E. A.; Mastrikov, Y. A.; Gryaznov, D.; Heifets, E.; Maier, J. *Phys. Rev. B* **2005**, *72*, 214411.
- (30) Choi, Y. M.; Lin, M. C. and Liu, M. *Angew. Chem. Int. Ed.* **2007**, *46*, 7214 –7219.
- (31) Wang, Y.; Arai, M.; Sasaki, T.; Wang, C. *Appl. Phys. Lett.* **2006**, *88*, 091909.
- (32) Eglitis, R.I. *Solid State Ionics* **2013**, *230*, 43–47.
- (33) Fabbri, E.; Pergolesi, D.; Traversa, E. *Chem. Soc. Rev.* **2010**, *39*, 4355.
- (34) Islam, M. S.; Slater, P. R.; Tolchard, J. R. and Dinges T. *Dalton Trans.* **2004**, *19*, 3061–3066.
- (35) Kreuer K. D. *Solid State Ionics* **1999**, *125*, 285–302.
- (36) Fabbri, E.; Bi, L.; Pergolesi, D. and Traversa, E. *Adv. Mater.* **2012**, *24*, 195–208.
- (37) Pionke, M.; Mono, T.; Schweika, W.; Springer T. and Schober, T. *Solid State Ionics* **1997**, *97*, 497–504.
- (38) Kreuer, K. D.; Fuchs A. and Maier, J. *Solid State Ionics* **1995**, *77*, 157–162.

PART D: MOLTEN CARBONATE AS A NON-METAL CATALYST FOR CO OXIDATION

D1: Introduction

Carbon monoxide (CO) is not only toxic to human and environment but also a poison to many metal catalysts in industrial processes. The easiest way to remove CO from other gases is to turn it into carbon dioxide, a less toxic and inert gas. Precious metals have been mostly promoted for such purpose with promising performances observed. For example, Bond et al. have firstly demonstrated Pd/SnO₂ as an excellent CO oxidizing catalyst at the temperature of 120-200 °C [1]. More recently, Stark and Harris developed the catalyst systems of Pd/SnO₂ and Pt/SnO₂, showing every high conversion efficiency even at -27 °C. They were successfully deployed to CO₂ laser systems [2-3]. Additionally, other metal catalysts such as Au/MnO₂ [4-6], Au/Fe₂O₃ [7-8], Pt/Al₂O₃ [9-11], Ru-Pt [12-13] and Ag/MnO₂ [14-15] have also been extensively investigated for catalyzing the oxidation of CO at ambient or low temperatures. Significant potential applications for such systems include CO₂ laser, auto exhaust gas treatment, gas purification and mine rescue.

To reduce or remove the usage of precious metals as they are of high cost and limited resource availability, many efforts have been geared towards low-cost transition metals and their oxides [16-18]. For example, Wang et al. prepared a copper-based catalyst of 7.5Cu/10SDC and achieved a conversion of 97% at 175 °C [19]. Kang et al. reported a catalyst of CoO_x/CeO₂ with a very low reaction temperature and good water vapor resistance [20]. It was proposed that highly dispersed Co at high valence state plays an important role in the process of CO oxidation. More recently, nanostructures like graphene [21-22], nanotube [23-24], zeolite [25], and MOF[26-27] have also been extensively examined for CO oxidation. As we know, the gas mixtures are at very high temperatures in some cases such as combustion engine exhaust and industry processes, which may cause changes of the geometrical and electronic structure, and chemical reactivity for the metal-based catalysts. Finally, the catalyst will be degraded.

In the past decades, molten carbonates (MC) have been used in the fuel cells as electrolyte. Recently, they were introduced into the cathode of solid oxide fuel cells (SOFC) as a booster for the reaction of oxygen reduction. Qin et al. studied the dissociative adsorption of oxygen in MC using density functional theory (DFT) modeling and found that oxygen exists in MC as perocarbonate (CO₄²⁻) [28]. In CO₄²⁻, an oxygen atom is carried by a carbonate ion and considered as a strong oxidizing agent. To prove the concept that MC could be a possible non-metal catalyst for oxidization, we have performed a combined experimental and computational study of CO oxidation catalyzed by MC in the current report. To our knowledge, this is the first time to use liquid phase molten salt to catalyze the CO oxidation and will open a door for developing non-metal eco-friendly catalysts for different industrial and environmental processes in the future.

D2: Experimental and Computational Methods

D2.1: Catalyst preparation

Ternary eutectic molten carbonate of Li/Na/K was supported on Al₂O₃ (1/8" pellets, high surface area, Alfa Aesar) and used as CO oxidation catalyst. Li₂CO₃ (Alfa Aesar, 99.8%), Na₂CO₃ (Alfa Aesar, 99.9%) and K₂CO₃ (Alfa Aesar, 99.8%), the precursors of the ternary molten carbonate, were dissolved in deionized water in a molar ratio of 42.5 : 32.5 : 25.0 to form a saturated

aqueous solution. The catalyst (MC/Al₂O₃) was prepared by impregnation of porous Al₂O₃ with the ternary carbonate aqueous solution. More specifically, the Al₂O₃ porous pellets were soaked in carbonate solution for approximately 4 hours in a vacuum chamber (10KPa), then dried in an oven at 80 °C for 12 hours and followed with calcinating at 400 °C to remove the moisture. The MC load was approximately 1.0% by weight.

D2.2: Catalyst characterization

The microstructure and the composition of the catalyst before and after testing were analyzed by scanning electron microscopy (SEM, Zeiss FESEM) combined with an energy dispersive X-ray spectroscopy (EDS). The catalytic oxidation of carbon monoxide was carried out in a horizontal flow reactor, illustrated in Fig. 1. The catalyst, 20g MC/Al₂O₃ (approximately 0.2g MC), was loaded to the center of the alumina tube and packed tightly with two porous ceramic pellets. A mixture of CO and air was fed in from one side of the reactor and collected from the other side. The flow rate of each gas was controlled by mass flow controllers (Alicat Scientific, MC-50SCCM-D/5M), while soap film flow meter was used for calibrations. The flow rate of CO was controlled at 6.76 sccm, while the total flow of approximately 100 sccm. The actual total flow rate of inlet gas (feed gas) and outlet gas (product gas) was measured by the soap film flow meter and used for calculating the CO conversion. The outlet gas was analyzed by a CO₂ detector (Vernier, CO₂ sensor) to identify the content of the CO₂. The concentration of CO₂ was tested every 10 °C from 300~600 °C. At each temperature point, the system was held at least for 30 min before measuring the CO₂ concentration. The CO₂ content is then used to determine the CO conversion as a function of temperature.

For the reaction of CO oxidation, $\text{CO} + \frac{1}{2} \text{O}_2 \rightarrow \text{CO}_2$, the amount of CO consumed should equal to that of CO₂ produced. Therefore, the CO conversion as percentage can be calculated by:

$$\text{Conversion} = F'_{\text{CO}_2} / F_{\text{CO}} = (F'_{\text{total}} \times C_{\text{CO}_2}) / F_{\text{CO}},$$

where F'_{total} is outlet gas total flow rate, F'_{CO_2} is CO₂ yield flow rate in outlet gas, C_{CO_2} is the concentration of CO₂ in the outlet gas, and F_{CO} is the CO feed flow rate.

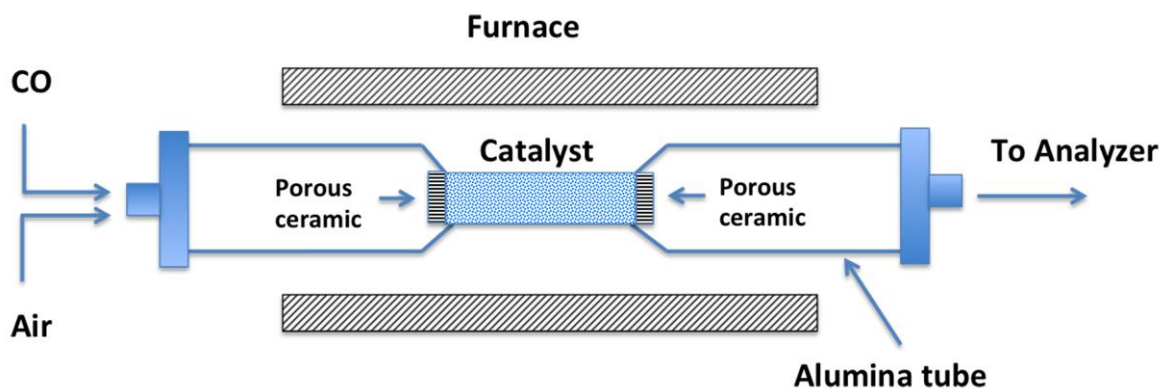


Figure 1: Illustration of the tubular reactor for the catalyst testing

D2.3: DFT Modeling

All structures were optimized at the B3LYP [29-30]/6-31G(d,p) [31-34] level using the Gaussian 09 program[35]. All stationary points on the potential energy surface (PES) were then verified by

calculated vibrational frequencies at the same theoretical level. Therefore, the reactant and product structures are truly local minima while each transition state is at the first order saddle point. The reaction pathway, i.e. the connection between reactant, TS and product, was verified by the intrinsic reaction coordinate (IRC) calculations.

D3: Results and discussion

D3.1: Physical characterization

Fig. 2 (a) and (b) shows the SEM images of the MC/Al₂O₃ catalyst before and after test, respectively. The flake like crystal is the MC phase, which covers almost all the surface of the Al₂O₃ support comparing to pure Al₂O₃, as shown in Fig. 2(c). To further confirm the composition of the crystal phase, EDS was involved to test the composition of the red square area in Fig. 2(a), and the result was shown in Fig. 2(d). From Fig. 2(d), Na, K, C and O were observed, indicating that the crystal phase is the molten carbonate. However, Li is too light to be detected by EDS. Element Al is from the Al₂O₃ support, and Au is from the Au coating, which had to be added for the SEM imaging. A schematic of the MC/Al₂O₃ catalyst below melting point is shown in Fig. 2(e), while Fig. 2(f) for it above the melting point. The catalyst was weighted before and after test and the weight was almost the same, indicating no any loss of the catalyst during the reaction process. In addition, its microstructure remains same before and after the test. So the MC/Al₂O₃ catalyst has a good stability.

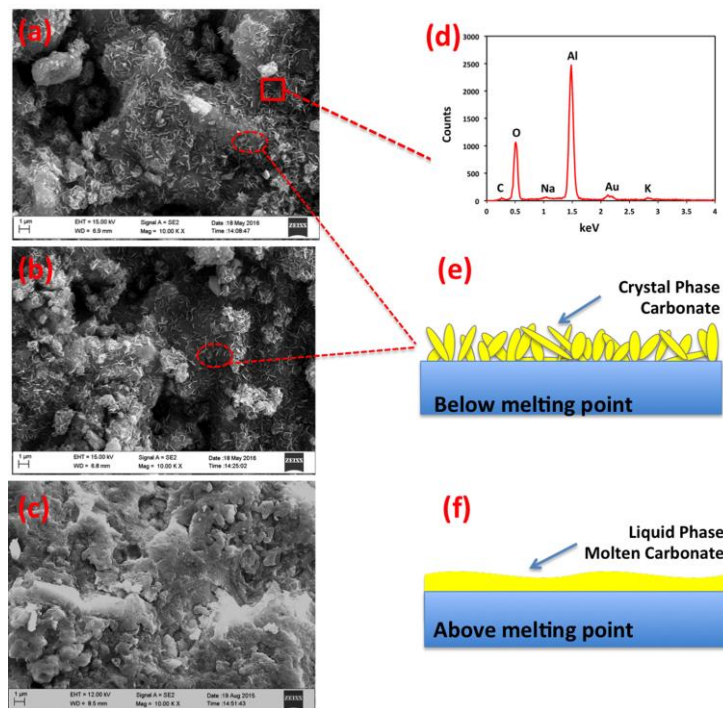


Figure 2: SEM images of (a) MC/Al₂O₃ before test; (b) MC/Al₂O₃ after test; (c) Al₂O₃ pellet support; (d) EDS result of MC on the Al₂O₃; (e) schematic of solid phase of MC on the Al₂O₃; (f) schematic of MC on the Al₂O₃ above melting point

D3.2: Catalytic reaction evaluation

Fig. 3 shows the conversion of the carbon monoxide to carbon dioxide with and without the presence of the MC/Al₂O₃ catalyst. It is found that the CO conversion with MC/Al₂O₃ is higher

in the whole temperature range of 300~600 °C, showing a good catalytic performance of MC/Al₂O₃ for the oxidation of CO. Two inflection points are shown in the conversion curve of MC/Al₂O₃. The first inflection point is at about 450 °C, which is the melting point of the MC. Below 450 °C, the CO conversion on solid phase MC is very low, but still much higher than that with no MC catalyst. However, the CO conversion on liquid phase increases dramatically with the temperature increase from 400 °C to 450 °C. The CO conversion with MC/Al₂O₃ reaches 96% at 500°C, while only 25% at the same temperature without catalyst. The results indicate that both solid phase and liquid phase MCs present the catalytic activity for the CO oxidation, but the liquid phase has a much higher catalytic activity. The second inflection point is at 500°C, the conversion curve becomes flat and stabilized at 96-98% due to the fact that most of CO has been converted to CO₂.

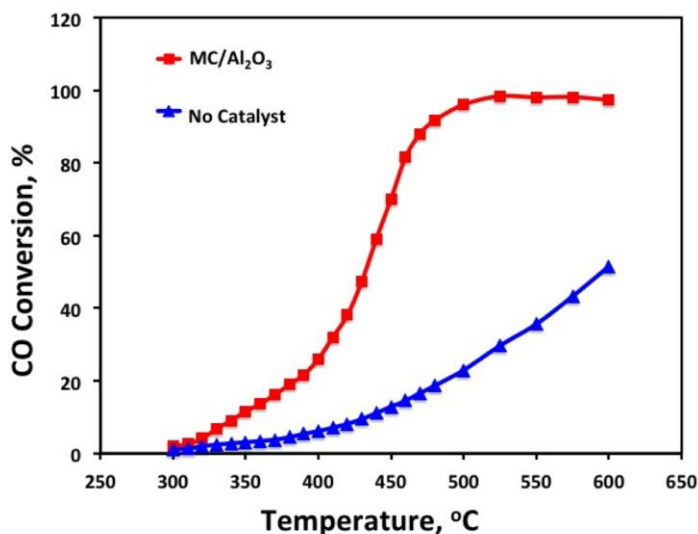


Figure 3: CO conversion vs Temperature

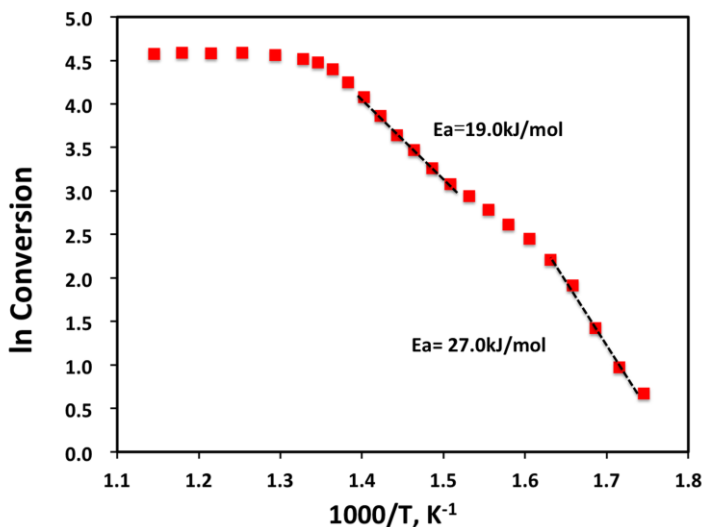
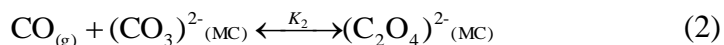
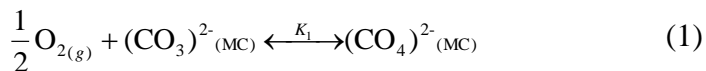


Figure 4: Arrhenius plot of calibrated CO conversion

Fig. 4 shows the arrhenius plot of the CO conversion by MC/Al₂O₃ as a function of 1000/T (K⁻¹). Before molten carbonate melting, the activation energy (E_a) is approximately 27.0 kcal/mol. After melting point, the E_a value is decreased to 19.0 kcal/mol. The large difference in E_a implies that the reaction may proceed through different pathways under low and high temperature. Above 500 °C, the gas phase reaction of CO with oxygen becomes significant and it is extremely hard to evaluate the contribution from the catalyst. So we did not examine the activity energy beyond 500 °C.

D3.3: Reaction mechanism

Assuming that the reaction will proceed through a Langmuir-Hinshelwood (L-H) mechanism, it can then be described by Eqn. (1-3). Using DFT methods, those three steps have been investigated to help understand the reaction kinetics and mechanism. The enthalpy change is calculated to be -0.3 kcal/mol and -36.4 kcal/mol at the B3LYP/6-31G(d) level for Eqn. (1) and (2), respectively. This indicates that both oxygen dissociation and CO adsorption are exothermic and favored by chemical equilibrium, but the step of Eqn. (2) is much more favored, i.e. $K_2 \gg K_1$. However, the step of Eqn. (1) has an energy barrier of about 23.0 kcal/mol calculated by DFT in pure lithium carbonate [28].



For the surface reaction of Eqn. (3), DFT calculations were performed using a small cluster of Li₂(C₂O₄)-Li₂(CO₄) as shown in Fig. 5. The overall reaction path and potential energy surface (PES) are plotted in Fig. 6. At the initial state, both CO and O₂ are brought to the surface of carbonate catalyst as the molecular form of (C₂O₄)²⁻ and (CO₄)²⁻ and the oxygen and CO are pointing to each other, highlighted by red and blue circle, respectively. Once the oxygen atom leaves its carbonate carrier, it will approach CO of (C₂O₄)²⁻ and this leads to a transition state (TS1). At TS1, the O-O bond is breaking, while the C-O bond is forming as highlighted in the orange circle. Next, CO₂ is formed, but it is attached to a carbonate ion, forming an intermediate state of pyrocarbonate (C₂O₅)²⁻. The same structure was identified by Huang et al. and reported in Ref. [36]. Through another transition state (TS2), CO₂ is released and finally detached from the surface of MC. From Fig. 6, the energy barrier for the surface reaction of Eqn. (3) is calculated to be only 11.4 kcal/mol.

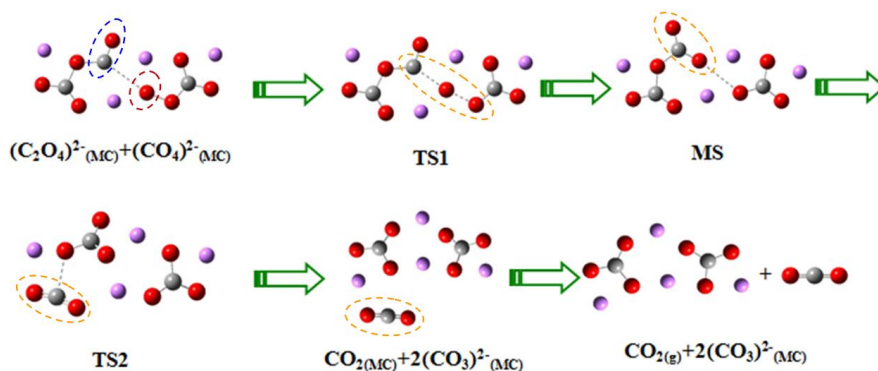


Figure 5: Structural evolution of the reaction process calculated by DFT

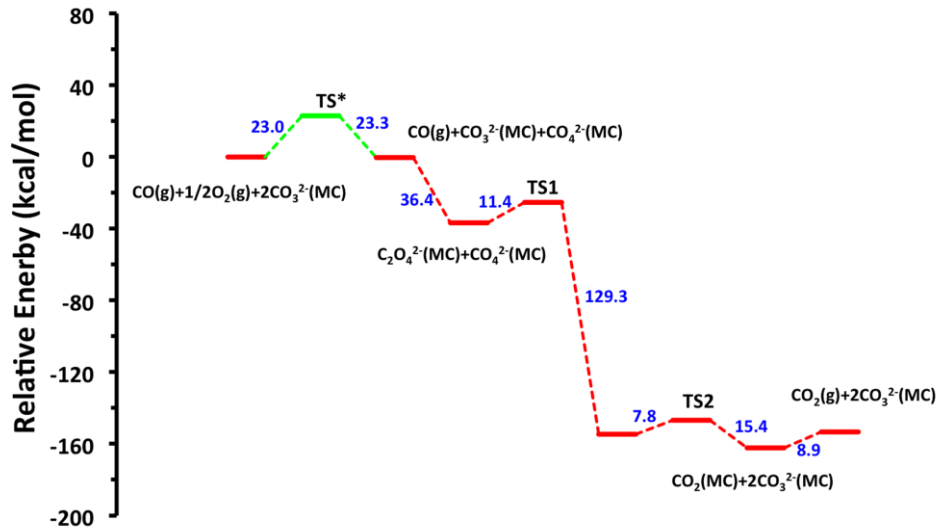


Figure 6: Reaction path and potential energy surface

From classical Langmuir-Hinshelwood mechanism, the reaction rate can be described by:

$$r = k C_{CO_3^{2-}}^2 \frac{K_1 K_2 C_{O_2}^{1/2} C_{CO}}{(1 + K_1 C_{O_2}^{1/2} + K_2 C_{CO})^2} \quad (4),$$

where r is the reaction rate, k for the rate constant of Eqn. (3), K_1 and K_2 for the equilibrium constant of Eqn. (1) and (2). From the DFT results, we can conclude $K_1 C_{O_2}^{1/2} \ll K_2 C_{CO}$, then the reaction rate will be approximated as:

$$r = k C_{CO_3^{2-}}^2 \frac{K_1 K_2 C_{O_2}^{1/2} C_{CO}}{(1 + K_2 C_{CO})^2} \quad (5).$$

If the concentration of CO is extremely low, then $K_2 C_{CO} \ll 1$ and the reaction rate is approximated as

$$r = k K_1 K_2 C_{O_2}^{1/2} C_{CO} C_{CO_3^{2-}}^2 \quad (6).$$

The reaction is the first order with respect to CO, while half order for O_2 . Increase of the concentration of reactant, both CO and O_2 , will increase the reaction rate. On the other hand, if the CO concentration is very high, then $K_2 C_{CO} \gg 1$ and the reaction rate is described by the equation of

$$r = k C_{CO_3^{2-}}^2 \frac{K_1 C_{O_2}^{1/2}}{K_2 C_{CO}} \quad (7).$$

In this case, the CO molecules will cover the catalyst surface and will inhibit the reaction. This should make the reactor more difficult and experience higher overall energy barrier. In the

current experiment setting, the effect of the concentration of CO was not investigated yet and will be reported in the future.

In Fig. 6, the reaction path is described by the PES as a function of reaction coordinate. The green part of oxygen dissociation in molten carbonate is from Ref. [28]. The reaction is initiated by oxygen dissociation, and then undergoes with CO adsorption, surface reaction of absorbed species, and finally desorption of CO₂. The rate determining step is oxygen dissociative adsorption with an energy barrier of 23.0 kcal/mol, while the surface reaction is relatively easy with calculated activation energy of 11.4 kcal/mol. The actual activation energy through Arrhenius plot method (Fig. 4) is measured to be 19.0 kcal/mol. This agrees with the DFT results. It should be pointed out that the contribution of entropy was not considered in the DFT calculations, but it should have some contributions to their reaction kinetics in such a high temperature reaction system.

D4: Conclusions

In the current study, we have examined molten carbonate as a non-metal catalyst for the CO oxidation at the temperature of 300~600 °C for the first time. The conversion is largely enhanced by melting at about 450 °C and increased to 96% at 500 °C. The reaction mechanism is described by a Langmuir-Hinshelwood model including four steps: (1) dissociation adsorption of oxygen, (2) adsorption of CO, (3) surface reaction, and (4) desorption of CO₂. DFT modeling reveals the formation of (C₂O₄)²⁻ and (CO₄)²⁻ as the intermediate species. It also shows that the first two steps are exothermic and preferred by chemical equilibrium, but the oxygen dissociation has higher energy barrier than the surface reaction itself and become the rate determining step in the whole process. The calculated energy barrier for oxygen dissociation to form CO₄²⁻ is 23.0 kcal/mol from Ref. [28], which is in a good agreement with the measured overall activation energy of 19.0 kcal/mol. Further analysis of the reaction kinetics indicates that the reaction is affected by the CO concentration. With low CO concentration, the reaction is the first order with respect to CO and half order to O₂. From this study, it has been proven that molten carbonate can serve as an efficient catalyst for CO oxidation and potentially for other oxidation reactions at the temperature range of 450~600 °C. More studies are demanded to further deliberate the reaction mechanism and explore more potential industrial applications.

D5: References:

- [1] G. C. Bond, L. R. Molloy, M. J. Fuller. Oxidation of carbon monoxide over palladium-tin(IV) oxide catalysts: an example of spillover catalysis, *J. C. S. Chem. Comm.* 829 (1975) 796-797
- [2] D. S. Stark, M. R. Harris. Catalysed recombination of CO and O₂ in sealed CO₂ TEA laser gases at temperatures down to -27°C, *J. Phys. E: Sci. Instrum.* 16 (1983) 492-496
- [3] D. S. Stark, A. Crocker, N. A. Lowde. A semiconductor-preionised sealed TEA laser operating at high CO₂ concentrations and repetition rates up to 100 Hz, *J. Phys. E: Sci. Instrum.* 16(1983)11
- [4] Gar B. Hoflund, Steven D. Gardner, David R. Schryer, Billy T. Upchurch, Erik J. Kielin. Au/MnO_x catalytic performance characteristics for low-temperature carbon monoxide oxidation, *Applied Catalysis B: Environmental*, 6 (1995) 117-126

- [5] S. D. Gardner, G. B. Hoflund. Catalytic behavior of noble metal/reducible oxide materials for low-temperature CO oxidation. I. comparison of catalyst performance, *Langmuir*, 7 (1991) 2135-2139
- [6] L. H. Chang, N. Sasirekha, Y. W. Chen, W. J. Wang. Preferential oxidation of CO in H₂ Stream over Au/MnO₂-CeO₂ catalysts, *Ind. Eng. Chem. Res.* 45 (2006) 4927-4935
- [7] A. A. Herzing, C. J. Kiely, A. F. Carley, P. Landon, G. J. Hutchings. Identification of active gold nanoclusters on iron oxide supports for CO oxidation. *Science*, 321 (2008) 1331-1335
- [8] S. T. Daniells, M. Makkee, J. A. Moulijn. The effect of high-temperature pre-treatment and water on the low temperature CO oxidation with Au/Fe₂O₃ catalysts. *Catalysis Letters*, 39 (2005) 39-47
- [9] G. Avgouropoulos, T. Ioannides, C. Papadopoulou, J. Batista, S. Hovevar, H. K. Matralis. A comparative study of Pt/Y-Al₂O₃, Au/ α -Fe₂O₃ and CuO-CeO₂ catalysts for the selective oxidation of carbon monoxide in excess hydrogen, *Catal. Today*, 75 (2002) 157-167
- [10] Y. J. Mergler, A. Van Aalst, J. Van Delft, B. E. Nieuwenhuys. CO oxidation over promoted Pt catalysts, *Applied Catalysis B: Environmental*, 10 (1996) 245-261
- [11] K. Yoshimi, M. B. Song, M. Ito. Carbon monoxide oxidation on Pt (111) electrode studied by in-situ IRAS and STM: co-adsorption of CO with water on Pt (111), *Surface Science*, 368 (1996) 389-395
- [12] S. H. Joo, J. Y. Park, J. R. Renzas, D. R. Butcher, W. Huang, G. A. Somorjai. Size effect of ruthenium nanoparticles in catalytic carbon monoxide oxidation, *Nano Lett.* 10 (2010) 2709-2713
- [13] S. Alayoglu, A. U. Nilekar, M. Mavrikakis, B. Eichhorn. Ru-Pt core-shell nanoparticles for preferential oxidation of carbon monoxide in hydrogen, *Nature Materials*, 7 (2008) 333-338
- [14] T. Kou, D. Li, C. Zhang, Z. Zhang, H. Yang. Unsupported nanoporous Ag catalysts towards CO oxidation, *J. Molecular Catalysis A: Chemical*, 382 (2014) 55-63
- [15] R. Xu, X. Wang, D. Wang, K. Zhou, Y. Li. Surface structure effects in nanocrystal MnO₂ and Ag/MnO₂ catalytic oxidation of CO, *J. catalysis*, 237 (2006) 429-430
- [16] B. Skarman, D. Grandjean, R. E. Benfield, A. Hinz. Carbon monoxide oxidation on nanostructured CuO_x/CeO₂ composite particles characterized by HREM, XPS, XAS and high-energy diffraction, 211 (2002) 119-133
- [17] J. Y. Luo, M. Meng, X. Li, X. G. Li, Y. Q. Zha, T. D. Hu, Y. N. Xie, J. Zhang. Mesoporous Co₃O₄-CeO₂ and Pd/Co₃O₄-CeO₂ catalysts: synthesis, characterization and mechanistic study of their catalytic properties for low-temperature CO oxidation. *J. Catalysis*, 254 (2008) 310-324
- [18] W. Liu, M. F. Stephanopoulos. Total oxidation of carbon monoxide and methane over transition metal –fluorite oxide composite catalysts: I. catalyst composition and activity, *J. Catalysis*, 153 (1995) 304-316
- [19] J. B. Wang, D. H. Tsai, T. J. Huang. Synergistic catalysis of carbon monoxide oxidation over copper oxide supported on samaria-doped ceria, *J. Catalysis*, 208 (2002) 370-380
- [20] M. Kang, M. W. Song, C. H. Lee. Catalytic carbon monoxide oxidation over CoO_x/CeO₂ composite catalysts. *Applied catalysis A: General*, 251 (2003) 143-156

- [21] Y. Li, Z. Zhou, G. Yu, W. Chen, Z. Chen. CO catalytic oxidation on iron-embedded graphene: computational quest for low-cost nanocatalysts, *J. Phys. Chem. C* 114 (2010) 6250-6254
- [22] Y. Li, Y. Yu, J. G Wang, J. Song, Q. Li, M. Dong, C. Liu. CO oxidation over grapheme supported palladium catalyst, *Applied catalysis B: Environmental*, 125 (2012) 189-196
- [23] W. An, Y. Pei, X. C. Zeng. CO oxidation catalyzed by single-walled helical gold nanotube. *Nano. Lett.* 8 (2008) 195-202
- [24] I. Lin, Y. Lu, Hsin. Chen, Nitrogen-doped carbon nanotube as a potential metal-free catalyst for CO oxidation, *Phys. Chem. Chem. Phys.* 18 (2016) 12093-12100
- [25] N. G. Miriam, M. G. Izaskun, B. M. Angel, L. C. Dolores, C. A. Diego, Y. Hiromi. Pd/zeolite-based catalysts for the preferential CO oxidation reaction: ion-exchange, Si/Al and structure effect, *Catalysis Science Technology*. 6 (2016) 2623-2632
- [26] H. noei, O. Kozachuk, S. Amirjalayer, S. Bureekaew, M. Kauer, R. Schmid, B. Marler, M. Muhler, R. A. Fischer, Y. Wang. CO adsorption on a mixed-valence ruthenium metal-organic framework studied by UHV-FTIR spectroscopy and DFT calculations, *J. Phys. Chem. C* 117 (2013) 5668-5666
- [27] J. Ye, C. Liu. $\text{Cu}_3(\text{BTC})_2$: CO oxidation over MOF based catalysts, *Chem. Commun.* 47 (2011) 2167-2169
- [28] X. Lei, K. Haines, K. Huang, C. . Qin. DFT study of oxygen dissociation in molten carbonate, *J. Phys. Chem. A* 119 (2015) 8806-8812
- [29] C. Lee, W. Yang, R. G. Parr. Development of the Colle-Salvetti correlation-energy formula into a functional of the electron density, *Phys. Rev. B* 37 (1988) 785
- [30] A. D. Becke. Density-functional thermochemistry. III. The role of exact exchange. *J. Chem. Phys.* 98 (1993) 5648
- [31] M. M. Francel, W. J. Pietro, W. J. Hehre. Self-consistent molecular orbital methods. XXIII. A polarization-type basis set for second-row elements, *J. Chem. Phys.* 77 (1982) 3654
- [32] J. P. Blaudeau, M. P. McGrath, L. A. Curtiss, L. Radom. Extension of Gaussian-2 (G2) theory to molecules containing third-row atoms K and Ca. *J. Chem. Phys.* 107 (1997) 5016
- [33] V. A. Rassolov, J. A. Pople, M. A. Ratner, T. L. Windus. 6-31G* basis set for atoms K through Zn. *J. Chem. Phys.* 109 (1988) 1223
- [34] V. A. Rassolov, M. A. Ratner, J. A. Pople, P. C. Redfern, L. A. Curtiss. 6-31G* basis set for third-row atoms. *J. Comp. Chem.* 22 (2001) 976
- [35] M. J. Frisch, et al. Gaussian 09, Revision B. 01, Gaussian Inc., Wallingford CT, 2010
- [36] L. Zhang, X. Huang, C. Qin, K. Brinkman, Y. Gong, S. Wang, K. Huang. First spectroscopic identification of pyrocarbonate for high CO_2 flux membranes containing highly interconnected three dimensional ionic channels, *Phys. Chem. Chem. Phys.* 15 (2013) 13147-13152

PART E: CO OXIDATION BY ATOMIC AND MOLECULAR OXYGEN ON AG(100)

E1: Introduction

Carbon monoxide (CO) is one of the toxic and harmful gases in the air and also a poisoning gas in many industrial catalytic processes. Its oxidation by selected catalysts has been of considerable interest because of its significance in air cleaning and gas purification. For this purpose, a variety of catalysts have been investigated. Noble metals are of high efficiency at low temperatures¹⁻⁴, but their applications are limited by high costs and limited amount of resources. Therefore, more research has been turned to non-noble metal-based catalysts, such as binary oxides of $\text{Co}_3\text{O}_4/\text{CeO}_2$ ⁵, CuO/CeO_2 ⁶, and ternary oxide of $\text{CuO}/\text{Co}_3\text{O}_4/\text{CeO}_2$ (CCC)⁷. Such oxides above have shown high activity for the CO oxidation in simulated exhaust conditions. Additionally, great attention has recently been paid to Pt-based intermetallic compounds⁸⁻¹¹. For example, the Pt/Fe bimetallic nano-alloy¹² is favorable for CO oxidation, over which CO can be completely removed around the room temperature. Besides metal oxide and bimetallic catalysts, new efforts are also being made to search for better supporting materials such as monolayer MoS_2 ¹³, graphyne¹⁴, graphene¹⁵⁻¹⁷, graphene oxide¹⁸, and single layer hexagonal BN (*h*-BN)¹⁹⁻²³. They can not only effectively anchor the metal atoms, but also can boost the catalytic performance due to their large specific surface areas and novel electronic and thermal properties. This opens a new direction in designing future catalysts for the CO oxidation.

Compared to catalysts mentioned above, silver (Ag) as a relatively inexpensive metal is an important candidate for the CO oxidation reaction in present industries. Ag-based catalysts have been extensively investigated in recent years due to their catalytic properties for CO oxidation²⁴⁻²⁸. The results in Ref. [24] show that porous Ag- Fe_2O_3 nanocomposite has a good reproducibility and stability in CO oxidation. Zhang et al. reported that an Ag/SBA-15 catalyst with low loading of 1.42 wt% can achieve 98% conversion of CO at 20 °C²⁶. More recently, it was shown that well-dispersed spherical silver nanoparticles deposited on carbon nanotube can convert CO to CO_2 approximately 100% at 220 °C²⁷. On the theoretical side, the CO oxidation was also examined on silver or silver-based alloys using cluster models in combination with density functional theory (DFT) methods²⁹⁻³². It is surprising that simple silver surfaces such as 100, 110 and 111 have not been considered yet, which are of considerable importance for a better understanding of the reaction kinetics and mechanism. In this report, a systematic DFT study of CO oxidation by molecular and atomic oxygen on the surface of Ag(100) is presented. The goal is to obtain the mechanism for CO oxidation at the atomic level. Hence, the reaction pathways, energetics, geometrical and electronic structures (density of state and molecular orbitals) were particularly computed and discussed.

E2: Computational details and models

All calculations were performed using the suite program of Gaussian09³³. The pw91pw91 hybrid exchange-correlation functional³⁴⁻³⁵ was used, which has shown good reliability and accuracy in previous reports³⁶⁻⁴⁰. For silver, the effective core potential (ECP) of Lanl2 combined with the DZ basis set was adopted⁴¹⁻⁴³. While for O and C atoms, the full electron basis set of 6-31G(d) was employed⁴⁴⁻⁴⁶. All stationary points on the potential energy surface (PES) were verified by calculated vibrational frequencies at the same theoretical level as used in the geometry optimization. To locate a transition state (TS), a relaxed PES scan was carried out first to find the structure with the highest energy on the reaction path. It was then optimized with full relaxation using the Berny algorithm and confirmed to be a saddle point with only one

imagery frequency. Finally, the reaction path was determined by the intrinsic reaction coordinate (IRC)⁴⁷⁻⁴⁸ calculations, which verifies the connection from the reactant, TS to product on PES.

In the current work, only the low index surface of Ag(100) was considered as the model for silver surface, which was represented by a three-layer silver cluster with a fixed Ag-Ag distance of 2.89 Å, the value from experimental bulk lattice. As displayed in figure 1, the cluster models of Ag₂₉ and Ag₃₈ represent the Ag(100) surface and are used for CO oxidation by atomic oxygen and molecular oxygen, respectively. Three adsorption sites were considered: on the top of silver atom (atop site), on the top of Ag-Ag bond (bridge site), and on the top of the center of tetragonal silver ring (hollow site). The adsorption energy is defined by the formula of

$$E_{ads} = E_{adsorbate} + E_{Ag(100)} - E_{adsorbate@Ag(100)},$$

where $E_{adsorbate}$ represents the total energy of O, triplet O₂, and CO, respectively. $E_{Ag(100)}$ and $E_{adsorbate@Ag(100)}$ are the total energy of Ag(100) without and with the adsorbate. By this definition, a positive value of adsorption energy represents an exothermic adsorption process.

To test the reliability of pw91pw91, a comparative study of the adsorption of CO on Ag(100) were performed using b3pw91⁴⁹ and b3lyp⁵⁰⁻⁵¹. The results are presented in subsection 3.1 with adsorption energies summarized in Table 1. From table 1, it is found that the values by pw91pw91 are in the best agreement with those from experiments and other theoretical calculations. In addition, we did some testing calculations on the CO adsorption using long-rang corrected B3LYP functionals (CAM-B3LYP, GD2/B3LYP and GD3/B3LYP). The results are listed in Table 2. It was found that GD2 and GD3 can largely improve the adsorption energy, but have only small effects on the natural charge and adsorption structures. So those testing results have confirmed that pw91pw91 is the best choice for the current molecular system.

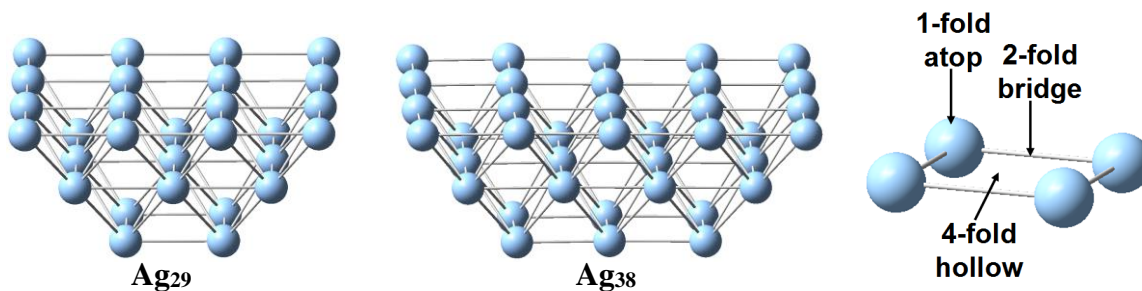


Fig. 1 Cluster models (Ag₂₉ and Ag₃₈) for Ag(100) and three typical adsorption sites of atop, bridge, and hollow. The model is designed by a three-layer silver cluster with fixed Ag-Ag distance of 2.89 Å. Ag₂₉ and Ag₃₈ represent the surface of Ag(100) for the CO oxidation by atomic and molecular oxygen, respectively.

Table1. The calculated C-O bond length (d_{C-O}), CO-surface distance of (d_{C-Ag}), C-O stretching frequency (ω_{C-O}), CO-Ag vibrational frequency (ω_{CO-Ag}), and adsorption energy (E_{ads}) for the CO adsorption on Ag(100) together with previous experimental and theoretical values.

d_{C-O} (Å)	d_{C-Ag} (Å)	ω_{C-O} (cm ⁻¹)	ω_{CO-Ag} (cm ⁻¹)	E_{ads} (kcal/mol)
---------------	----------------	------------------------------------	--------------------------------------	-------------------------

pw91pw91	1.152	2.232	2055.5	156.5	8.4
b3pw91	1.138	2.312	2176.0	123.6	3.7
b3lyp	1.137	2.469	2181.5	83.4	2.7
theoretical	1.150 ⁵²	2.230 ⁵²	2050 ⁵²	203 ⁵²	-
experimental	-	-	2137.0 ⁵³	-	6.5 ⁵⁴

Table2. The calculated natural charge on C atom (Q_C), on O atom (Q_O), sum of CO molecule (Q_{CO}), C-O bond length (d_{C-O}), CO-surface distance of (d_{C-Ag}), and adsorption energies of CO (E_{ads}) on silver (Ag_{38}) obtained from PW91PW91, B3LYP, CAM-B3LYP, GD2/B3LYP, and GD3/B3LYP, respectively.

	Q_C (e)	Q_O (e)	Q_{CO} (e)	d_{C-O} (Å)	d_{C-Ag} (Å)	E_{ads} (kcal/mol)
PW91PW91	0.559	-0.374	0.185	1.152	2.232	8.4
B3LYP	0.638	-0.423	0.215	1.137	2.469	2.7
CAM-B3LYP	0.648	-0.421	0.227	1.132	2.409	4.6
GD2/B3LYP	0.613	-0.409	0.204	1.138	2.301	8.0
GD3/B3LYP	0.620	-0.412	0.208	1.137	2.334	8.5

E3: Results and Discussions

E3.1: Adsorptions of single O atom, O₂ and CO molecules on Ag(100)

We first examined the adsorption of single O atom, O₂ and CO molecules on the clean surface of Ag(100), which is the prerequisite for the CO oxidation. Various adsorption configurations have been considered in order to find the most stable one for each adsorbate. Fig. 2 shows the optimized structures with the highest adsorption energy for single O, O₂ and CO, respectively. For atomic oxygen, it prefers the 4-fold hollow site with an adsorption energy of 76.6 kcal/mol. While for molecular oxygen, the O₂ molecule is parallel to the silver substrate and adsorbed on the hollow site with only small adsorption energy of 2.7 kcal/mol. The distance between oxygen and silver surface (d_{O-Surf}) is 1.037 Å and 1.724 Å for atomic and molecular oxygen, respectively. From the calculated adsorption energy and d_{O-Surf} , we conclude that the adsorption of O atom on Ag(100) is stronger than that of O₂ molecule. In addition, the natural population analysis (NPA) indicates that the sum of natural charges is -0.943 e and -0.784 e for atomic and molecular oxygen, respectively. The negative charge implies a significant charge transfer from silver substrate to the O atom or O₂ molecule, showing a strong chemical bonding between silver and oxygen. So the adsorption of either atomic or molecular oxygen is of chemical type on Ag(100). Furthermore, after O₂ adsorption, the O-O bond length is elongated to 1.397 Å, which is significantly larger than that of the free O₂ molecule, 1.228 Å. Compared with the vibrational frequency of free O₂ molecule (1574.6 cm⁻¹), the O-O stretching frequency of 838.7 cm⁻¹ is drastically lowered by the bonding to the silver surface. In the view of the elongated O-O bond and very low vibrational frequency, it is clear that the O-O bond is weakened and the O₂ molecule is likely turned into superoxide on silver. This result is very similar to the dioxygen on

Ag (110) reported by Backx et al.⁵⁵. The weakening of the O-O bond makes dioxygen more reactive, which will facilitate the oxidation of CO molecule on the silver surface.

Different from oxygen, CO is found to be the most stable at the 1-fold atop site in an upright position with the carbon atom pointing towards the silver surface (C-down adsorption model), which agrees with previous studies using the configuration interaction (CI) method⁵⁶. The corresponding adsorption energy and C-Ag distance is 8.4 kcal/mol and 2.232 Å, respectively. The present adsorption energy is very close to the experimental value of 6.5 kcal/mol obtained using thermal desorption spectroscopy (TDS) on Ag (111) surface⁵⁴, but it is slightly higher than 4.4 kcal/mol at the CI level⁵⁶ on Ag(100) and ~3.2-3.7 kcal/mol at the DFT-GGA-PW91 level⁴⁸ on Ag(111). The net natural charge transfer from CO to Ag(100) is found to be 0.185 e (C: 0.559 e; O: -0.374 e), which is slightly larger than 0.123 e obtained from CI calculations and mainly from the C lone pair orbital to silver⁵⁶. The calculated molecular orbital in Fig. 3 confirms that CO adsorption on silver is of chemical type. Upon adsorption, the C-O bond length (d_{C-O}) is elongated due to the interaction between C $2p$ and Ag $4d$ orbitals. The d_{C-O} is calculated to be 1.152 Å, which is slightly larger than that of free CO molecule, 1.148 Å, but in line with the 1.150 Å calculated using the projector-augmented-wave (PAW) method⁵². Moreover, the vibrational frequency of C-O is calculated to be 2055.5 cm^{-1} , which is smaller than that of free CO molecule (2128.1 cm^{-1}) and experimental value of 2137.0 cm^{-1} ⁵³.

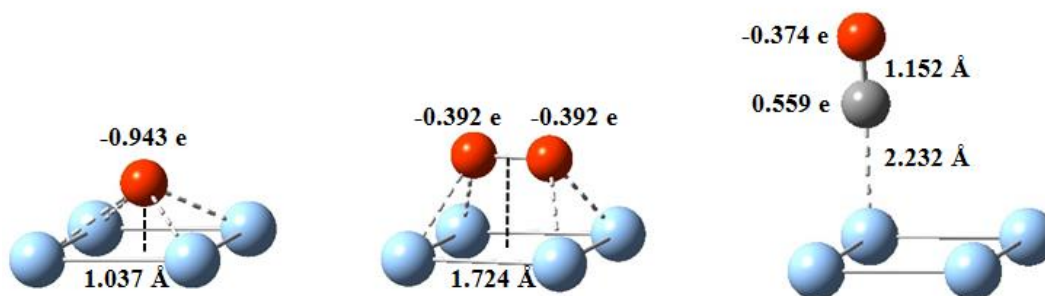


Fig. 2 The optimized adsorption structure with the lowest energy for single O atom (a), O₂ molecule (b), and CO molecule (c) on Ag(100).

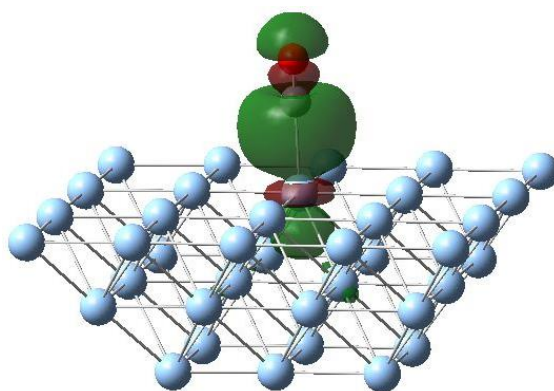


Fig. 3 Selected molecular orbital of CO adsorption on Ag(100).

E3.2: CO oxidation by molecular oxygen on Ag(100)

As we know, there are two well-established mechanisms for the CO oxidation by O₂ molecule: the Langmuir-Hinshelwood (L-H)^{13, 57-58} and the Eley-Rideal (E-R) mechanism^{15, 18, 59-61}. In the L-H mechanism, the CO and O₂ molecules are co-adsorbed on the surface of silver before reaction, a peroxo-type OOCO complex is proposed to be an intermediate state (MS). However, in the E-R mechanism, the CO molecule directly reacts with the pre-adsorbed O₂ molecule, producing a carbonate-like CO₃ complex as the MS. In the present study, the calculated adsorption energies for both CO (8.4 kcal/mol) and O₂ (2.7 kcal/mol) on Ag(100) are positive. So the L-H mechanism is expected to prevail over the E-R mechanism for CO oxidation by O₂ molecule on the silver surface. From previous studies¹³, the complete CO oxidation includes two steps: the L-H mechanism as a starting step with the reaction of CO+O₂→OOCO→CO₂+O, then following the E-R mechanism with the reaction of CO+O→CO₂. To achieve a comprehensive and better understanding, both mechanisms of CO oxidation are discussed below.

First, we considered the L-H mechanism of CO oxidation. Figure 4 depicts the structures of initial state (IS), transition state (TS), and final state (FS) together with the energy barrier of CO oxidation on Ag(100) with O₂ molecule present. As seen from figure 4, after CO and O₂ co-adsorbed on silver, CO is nearly parallel to O₂ with the C-O₂ distance of 1.356 Å and the O₂-C-O₁ angle of 119.3°. At this phase, the bond length of O₂-O₃ (1.461 Å) is larger than that of free oxygen molecule, indicating that the adsorbed oxygen molecule is activated and ready to participate in the CO oxidation reaction. The O₁-C bond length is 1.229 Å, slightly larger than that in the free CO molecule.

As displayed in figure 4, the CO oxidation process is initiated by the stretching of oxygen molecule (O₂-O₃) and leads to a TS on PES. At TS (only imaginary frequency is $i465.6\text{ cm}^{-1}$), the O₂-O₃ distance is elongated to 1.793 Å and the C-O₂ distance is shortened to 1.280 Å, showing a simultaneous bond forming and breaking process. At the end of reaction, C-O₁ and C-O₂ bond lengths are shortened to the equal value of 1.179 Å, which is the same as the bond length in free CO₂. The O₁-C-O₂ angle becomes 180.0° and a linear CO₂ molecule is formed. The calculated energy barrier is only 6.9 kcal/mol, indicating a favorable reaction of CO oxidation on silver. In addition, it is noticeable that the bond of O₁-C is first elongated from initial state of 1.229 Å to transition state of 1.244 Å, and then shortened to 1.179 Å at final state. The distance between O₃ and Ag surface decreases from 1.8 Å of initial state to 1.6 Å of transition state to 1.1 Å of final state. The variation of such bond distances sufficiently indicates that the CO oxidation is a synergistic process with CO, O₂ and silver surface all actively involved.

E3.3: CO oxidation by atomic oxygen on Ag(100)

In this section, we will focus on the E-R mechanism of CO oxidation. As discussed above, the final state of CO oxidation by O₂ molecule leads to a detached CO₂ and another chemisorbed O atom on the silver surface. Next, the CO oxidation by atomic oxygen on the silver surface will be examined. Figure 5 shows the local structures of beginning, transitioning, and ending states for the CO oxidation by atomic oxygen on the Ag(100) surface. First, CO is adsorbed on Ag(100) with an O atom pre-adsorbed. The calculated adsorption energy of CO is 6.2 kcal/mol by $E_{ads} = E_{\text{CO(gas)}} + E_{\text{O/Ag(100)}} - E_{\text{CO-O/Ag(100)}}$, which is slightly lower than that calculated on the clean Ag(100). However, both values are in fairly good agreement with the value of 6.5 kcal/mol⁵⁴ observed by experiment for CO molecule adsorbed on the clean surface of Ag(100), indicating

small effect of pre-adsorbed oxygen on the adsorption of CO. In figure 5, at the beginning state, the CO molecule is weakly adsorbed on the top of Ag2 with a tilt angle of 25.6° and C-O2 distance of 2.796 Å. The C-O1 bond length of 1.149 Å is very close to the 1.148 Å for free CO molecule and slightly shorter than 1.152 Å for CO adsorption on the clean silver surface. Compared with the adsorption on the clean silver surface, the C-Ag2 distance of 2.570 Å is larger than that of 2.243 Å, while the O2-Ag(100) distance of 1.003 Å is slightly short than that of 1.085 Å.

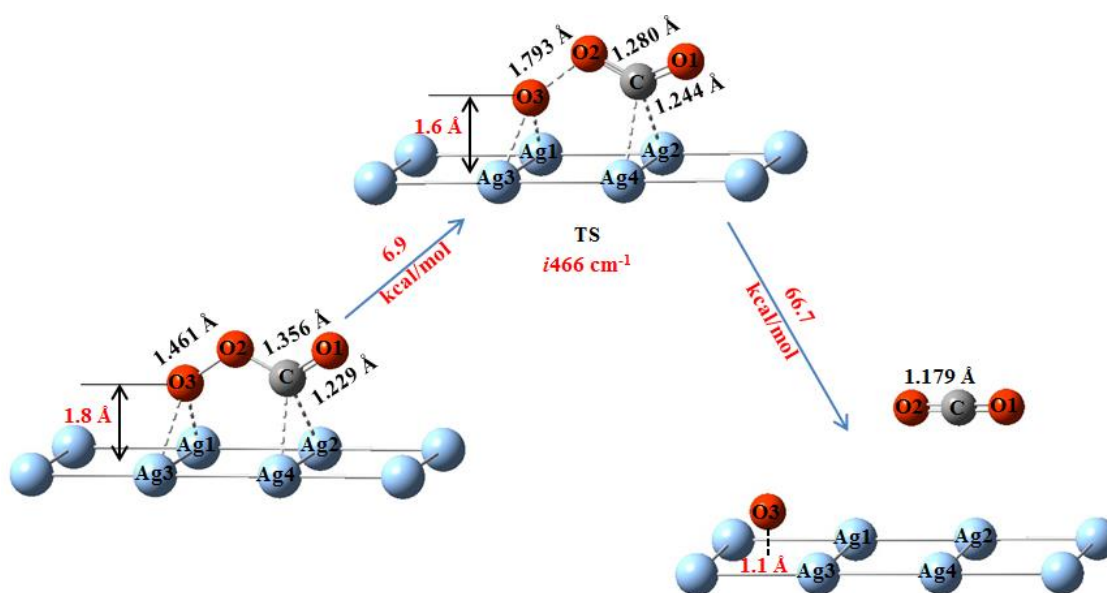


Fig. 4 Optimized structures and activation energy for CO oxidation by molecular oxygen on Ag(100).

As the CO molecule (CO1) descends and approaches the surface, the distance of C-Ag2 decreases. At the same time, the CO molecule rotates itself and the O2 atom accordingly raises itself. As a result, the O1-C-O2 angle increases and the C-O2 distance decreases quickly. This leads to a TS located on the PES with a single imaginary frequency of $i118\text{ cm}^{-1}$. At TS, the C-O2 distance is significantly shortened to 2.082 Å from 2.796 Å, while the C-O1 bond length is enlarged to 1.162 Å, and the O1-C-O2 angle is increased to 113.7° from the 103.8° at the beginning state. Simultaneously, the C-Ag2 distance decreased to 2.382 Å while the O2-surface distance increased to 1.158 Å. During this process, the system experiences an energy barrier of only 2.1 kcal/mol. Such a small conversion barrier implies that it is very easy for CO oxidation by atomic oxygen on the silver surface disregarding the effect of entropy. Finally, the O1-C-O2 angle is increased to 179.9° , and the bond lengths of O1-C and C-O2 equal to 1.179 Å, nearly identical to those in the free CO₂ molecule (bond angle: 180.0° ; bond length: 1.179 Å). This indicates the formation of CO₂ and a complete oxidation of CO. The PES calculated by IRC shows the connection from the starting structure, TS, to the final structure, providing a full picture of CO oxidation to CO₂ on the Ag(100) surface with O atom pre-adsorbed.

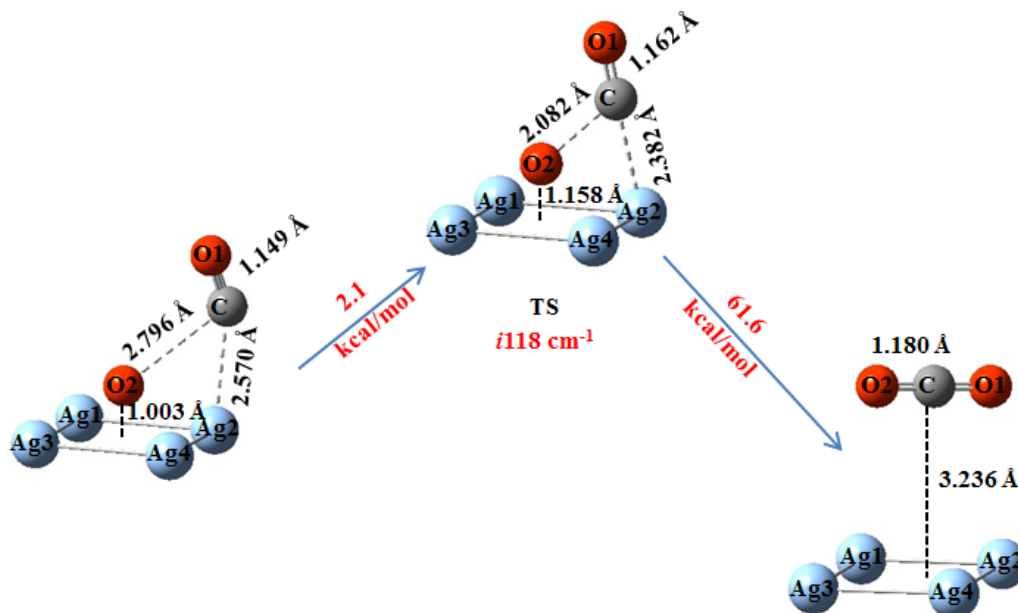


Fig. 5 Optimized structures and activation energy for CO oxidation by atomic oxygen on Ag(100).

E3.4: CO oxidation mechanism

E3.4.1 CO oxidation mechanism by molecular oxygen

To further understand the mechanism of CO oxidation by molecular and atomic oxygen on the silver surface, we plotted the broadened density of state (DOS) and overlap DOSs as shown in figure 6 and 7, respectively. Here, the electronic DOS was obtained by broadening the electronic energy levels with a Gaussian function. The full width at half maximum (FWHM) and the scale ratio for DOS were set to be 0.05 and 0.1, respectively. In addition, the isosurfaces of selected molecular orbitals (MOs) in the process of CO oxidation are also displayed in figure 6 and 7 with an isovalue of 0.02.

For CO oxidation by oxygen molecule on silver, figure 6 shows the broadened DOS and overlap DOSs of each atom. O1 (red line), O2 (blue line) and O3 (dark teal) represented the DOS of the O atom in the adsorbed CO molecule, one O atom in the adsorbed O₂ molecule finally bonded to the C atom, and another O atom in the adsorbed O₂ molecule finally chemisorbed on the silver surface, respectively. OP1 (dark yellow line), OP2 (dark blue line) and OP3 (brown line) represented the overlap DOSs of C-O1, C-O2 and O2-O3, respectively. The black line and pink line were DOSs of C atom and Ag atom, respectively. Be aware that the overlap of DOS (OP_n) is greater or less than zero denotes the corresponding MO is favorable or unfavorable for forming chemical bond, respectively. Different from the CO oxidation by atomic oxygen, the process of CO oxidation by molecular oxygen involves the dissociation of oxygen molecule on the silver surface. In other words, the O-O bond needs to be broken as the CO molecule being oxidized. As seen from DOSs and overlap DOSs in figure 6, at the reactant phase, there are overlaps of DOS between C and O1, C and O2, O2 and O3 at the energy range of -13 eV – -10 eV, which is also

evidenced from OP1, OP2, and OP3. So the orbitals are conducive for bonding in this energy range, which is also observed in the MOs. For the instance of MO on the left, there is a π -like bond between C, O1 and O2. Furthermore, there are significant hybrid orbitals between s and p orbitals of O2 and O3 atom, resulting in a σ bond between O2 and O3. Likewise, there are s , p and d hybrid orbitals between C, O3 and Ag, leading to partial σ -bonding between O3 and Ag, C and Ag, respectively. For the MO on the right, it is mainly of a big π -bond between O1, C, O2, and O3, mixed with partial σ -bond of O3-Ag, and C-Ag, respectively.

At the TS, the overlap of DOS between C and O2 is increased while that between O2 and O3 decreased, implying that the bonding between C and O2 is enhanced and that between O2 and O3 is weakened. On the other hand, the interaction between C and Ag is largely decreased as the C atom is leaving the silver surface and the O1-C-O2 bond angle being increased. On the contrary, the interaction between O3 and Ag is largely enhanced with the O3 atom getting closer to the surface and the bond length of O2-O3 being elongated. The results from DOS analysis are also supported by the selected MOs at TS.

Finally, the O-O bond of oxygen molecule is completely broken and CO oxidation is finished. From the DOSs and overlap DOSs of product, it is found that the DOSs of O1 and O2 are degenerate, so are the overlap DOSs of OP1 and OP2, but the overlap DOSs of OP3 is almost zero in the whole considered energy range. Correspondingly, the MO (left) at -12.4 eV forms a π bond by 2p orbitals of O1, C, and O2 atom, which is parallel with the nodal plane. The MO (right) at -12.3 eV also forms a π bond, which is perpendicular to the nodal plane.

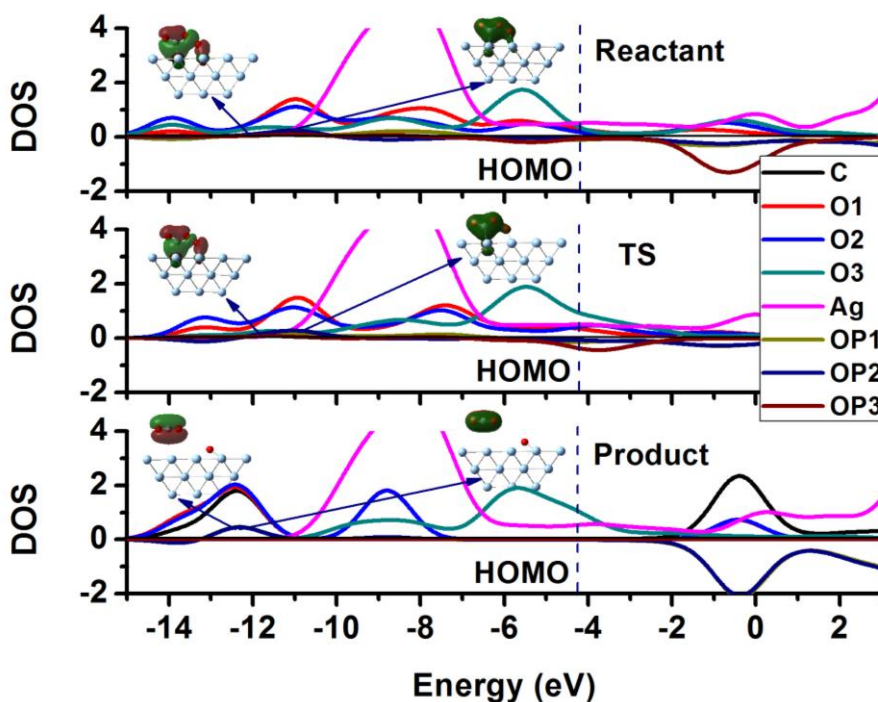


Fig. 6 The density of state (DOS), overlap DOS, and the selected molecular orbitals (MOs) related to the bonding of O1-C-O2-O3-Ag at reactant, transition state (TS), and product for CO oxidation by molecular oxygen on Ag (100), respectively. O1, O2 and O3 represent the O atom in the adsorbed CO molecule, one O atom in the adsorbed O₂ molecule finally bonding to the C atom, and another O atom in the adsorbed O₂ molecule finally

chemisorbed on the Ag surface, respectively. OP1, OP2 and OP3 represent the overlap DOSs of C-O1, C-O2 and O2-O3, respectively. Red and green parts correspond to positive and negative regions respectively, and the isovalue of the isosurface is set to be 0.02. For DOS of product, the DOSs of O1 and O2 atoms are degenerate, so are the overlap DOSs of OP1 and OP2 are degenerate, but the overlap DOSs of OP3 is almost zero in the whole considered energy range.

E3.4.2: CO oxidation mechanism by atomic oxygen

For CO oxidation by atomic oxygen, as shown in figure 7, O1 (red line) and O2 (blue line) are defined as the DOSs of the oxygen in the adsorbed CO molecule and one directly adsorbed on the silver surface, respectively. OP1 (pink line) and OP2 (dark yellow line) are defined as the overlap DOSs of C-O1 and C-O2, respectively. At the beginning of CO oxidation (reactant), the red line is high, showing overlaps with the black line (DOS of C) in the region of -15 eV to -10 eV. However, the dark teal curve (DOS of Ag) and the blue one mainly appear in the region of -10 eV to HOMO. The pink curve is greater than zero in the region of -12.5 eV to -10 eV under the HOMO energy level, while the dark yellow curve is almost zero in the whole considered energy range. Therefore, we can conclude that 2p orbitals of O1 and C have made significant contributions to the bonding between C and O1. This is also evidenced in the corresponding MOs. In addition, Ag 4d and O2 2p orbitals have significant overlaps in the band of -10 eV to HOMO. On the other hand, there is only very little interactions between C 2p and O2 2p orbitals since the overlap DOS between C and O2 (OP2) is almost zero in our considered energy range. These conclusions are then confirmed by the isosurfaces of corresponding MOs. For example, the MO on the left is mainly attributed to a C-O1 π -bond, while that on the right is a π -bond perpendicular to the nodal plane. All these facts reveal that the C-O1 remains the bonding characteristics of a free CO molecule and is positioned for bonding with O2 atom on the silver surface. All these facts support an E-R reaction mechanism for this reaction step. It is necessary to make it clear that the effects of temperature are not considered here, which could make the free energy change of the CO adsorption positive due to the negative change of entropy at high temperatures. The actual mechanism of the CO oxidation by atomic oxygen is largely affected by the temperature. Therefore, the conclusion of an E-R mechanism here should not be exaggerated and further examinations by molecular dynamics (MD) based methods are needed to clarify the exact reaction mode.

At TS, the overlap between red and black lines is reduced, while that between blue and black lines is increased in the energy window of [-11.5, -8.5 eV]. This is supported by the decreasing of peak intensity of OP1. At the same time, the OP2 intensity appears greater than zero in the same energy range. These evidences indicate that the bond of C-O1 is weakened and the bond of C-O2 is strengthened. Meanwhile, the interaction between C atom and Ag surface is increased. From the MO on the left, as the CO molecule approaches the O2 atom and Ag surface, a σ -bond is formed by C 2p and O2 2p. The overlap between Ag 4d and C 2p is also significant. The distinct interactions of C-O2 and C-Ag are also observed in the MO on the right. These bonding and anti-bonding characteristics of MOs are coincident with the above analysis of bond length and bond angle of O1-C-O2. At the ending of CO oxidation (product), as the O1, C and O2 adjust their bond length, bond angle and orientation, the CO₂ molecule is finally formed and become parallel to the surface. In figure 6, the DOSs of O1 and O2 atoms are degenerate, so are the overlap DOSs of OP1 and OP2.

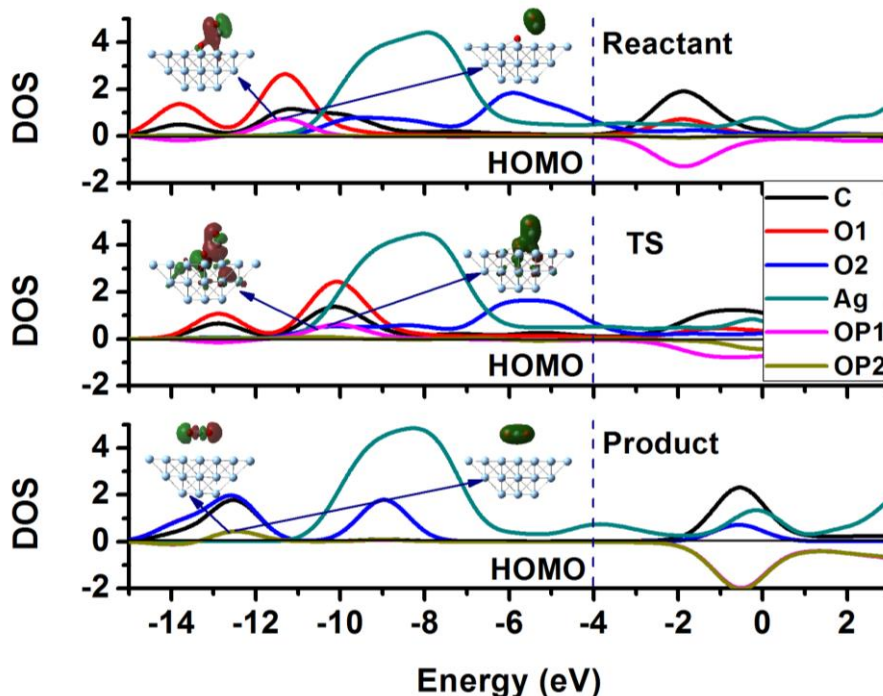


Fig. 7 The density of state (DOS), overlap DOS, and selected molecular orbitals (MOs) related to the bonding of O1-C-O2 at reactant, transition state (TS), and product for CO oxidation by atomic oxygen on Ag (100), respectively. O1 and O2 represent the O atom in the adsorbed CO molecule and the O atom pre-adsorbed on silver, respectively. OP1 and OP2 represent the overlap DOS between C and O1, and between C and O2, respectively. Red and green parts correspond to positive and negative regions respectively. The isovalue of the isosurface was set to be 0.02. For DOS of product, the DOSs of O1 and O2 are degenerate, and so are the overlap DOSs of OP1 and OP2.

E3.4.3: Formation and Dissociation of CO₃ on Ag(100)

For the reaction of CO oxidation on silver, the formation of surface carbonate species ($\text{CO}_{2(\text{g})} + \text{O}_{(\text{ad})} \rightarrow \text{CO}_{3(\text{ad})}$) has been identified³⁶. Two adsorption structures are bi-coordinated perpendicular and tri-coordinated parallel with calculated adsorption energy of 91.2 and 89.1 kcal/mol, respectively. For the dissociated reaction $\text{CO}_{3(\text{ad})} \rightarrow \text{O}_{(\text{ad})} + \text{CO}_{2(\text{g})}$, the energy barrier is calculated to be 19.8 and 26.3 kcal/mol for the bi-coord and tri-coord pathways, respectively. However, the reaction of $\text{CO}_{3(\text{ad})} + \text{CO}_{(\text{ad})} \rightarrow 2\text{CO}_{2(\text{g})}$ has an energy barrier of only 15.0 kcal/mol in Ref. [31]. In the same study, the activation energy for $\text{O}_{(\text{ad})} + \text{CO}_{(\text{ad})} \rightarrow \text{CO}_{2(\text{g})}$ was calculated to be 1.2 kcal/mol, which is very close to 2.1 kcal/mol from the current study. Based on those facts, we can conclude that the carbonates are fairly stable on silver, but can be removed by further CO dosing or dissociation. The reaction pathway of CO oxidation through carbonate is less favored thermodynamically.

E4: Conclusions

In summary, we have studied the CO oxidation by molecular and atomic oxygen on the silver surface at the DFT-PW91PW91/[LANL2DZ, 6-31G(d)] level. The Ag₂₉ and Ag₃₈ cluster models were selected to represent the Ag(100) surface. The calculated results show that all adsorptions of O, O₂ and CO molecules on Ag (100) are of chemical type. The O₂ molecule is partially activated when bonded to the Ag surface and ready to participate in the reaction of CO oxidation. The CO oxidation by O₂ molecule prefers the L-H mechanism and it involves the dissociation of the O-O bond and the formation of C-O bond. The interactions between 2s and 2p of C and O, and 4d of Ag orbitals facilitate the CO oxidation. However, the CO oxidation by atomic oxygen slightly favours the E-R mechanism since the adsorption of CO with the presence of absorbed oxygen is very weak and both its geometrical and electronic structures are closer to that of a free CO. The activation energy for CO oxidation is only 6.9 kcal/mol by molecular oxygen and 2.1 kcal/mol by atomic oxygen, respectively. So, both molecular and atomic oxygen are very reactive for CO oxidation on Ag(100). The formation and removal of CO₃ on silver is also discussed, but this pathway is not favoured thermodynamically. However, the low adsorption energy of CO on Ag(100) implies a low sticking probability of CO on silver with or without the presence of oxygen, which is not considered in the current study as well as the effects of temperature.

E5: References

- (1) Liu, L.; Zhou, F.; Wang, L.; Qi, X.; Shi, F.; Deng, Y. Low-temperature CO oxidation over supported Pt, Pd catalysts: Particular role of FeO_x support for oxygen supply during reactions. *J. Catal.* **2010**, *274*, 1–10.
- (2) Okumura, M. and Haruta, M. Interplay of theoretical calculations and experiments for a study of catalysis by gold. *Catal. Today* **2015**, *259*, 81–86.
- (3) Daniel, M.-C.; Astruc, D. Gold nanoparticles: assembly, supramolecular chemistry, quantum-size-related properties, and applications toward biology, catalysis, and nanotechnology. *Chem. Rev.* **2004**, *104*, 293–346.
- (4) Min, B. K.; Friend, C. M. Heterogeneous Gold-Based Catalysis for Green Chemistry: Low-Temperature CO Oxidation and Propene Oxidation. *Chem. Rev.* **2007**, *107*, 2709–2724.
- (5) Luo, J.; Meng, M.; Li, X.; Zha, Y.; Hu, T.; Xie, Y.; Zhang, J. Mesoporous Co₃O₄–CeO₂ and Pd/Co₃O₄–CeO₂ catalysts: Synthesis, characterization and mechanistic study of their catalytic properties for low-temperature CO oxidation. *J. Catal.* **2008**, *254*, 310–324.
- (6) Zheng, X.; Zhang, X.; Wang, X.; Wang, S.; Wu, S. Low-Temperature CO Oxidation over a Ternary Oxide Catalyst with High Resistance to Hydrocarbon Inhibition. *Appl. Catal. A* **2005**, *295*, 142–149.
- (7) Binder, A. J.; Toops, T. J.; Unocic, R. R.; Parks II, J. E. and Dai, S. Low-Temperature CO Oxidation over a Ternary Oxide Catalyst with High Resistance to Hydrocarbon Inhibition. *Chem. Int. Ed.* **2015**, *54*, 13263–3267.
- (8) Ko, E.-Y.; Park, E. D.; Lee, H. C.; Lee, D. and Kim, S. Supported Pt–Co Catalysts for Selective CO Oxidation in a Hydrogen-Rich Stream. *Angew. Chem. Int. Ed.* **2007**, *46*, 734–737.
- (9) Mu, R.; Fu, Q.; Xu, H.; Zhang, H.; Huang, Y.; Jiang, Z.; Zhang, S.; Tan, D. and Bao, X.

- Synergetic Effect of Surface and Subsurface Ni Species at Pt-Ni Bimetallic Catalysts for CO Oxidation. *J. Am. Chem. Soc.* **2011**, *133*, 1978–1986.
- (10) Alayoglu, S.; Nilekar, A. U.; Mavrikakis, M.; Eichhorn, B. Ru–Pt core–shell nanoparticles for preferential oxidation of carbon monoxide in hydrogen. *Nat. Mater.* **2008**, *7*, 333–338.
 - (11) Yamamoto, T. A.; Nakagawa, T.; Seino, S.; Nitani, H. Bimetallic nanoparticles of PtM (M= Au, Cu, Ni) supported on iron oxide: Radiolytic synthesis and CO oxidation catalysis. *Appl. Catal. A* **2010**, *387*, 195–202.
 - (12) Zhang, H.; Liu, X.; Zhang, N.; Zheng, J.; Zheng, Y.; Li, Y.; Zhong, C.-J.; Chen, B. H. Construction of ultrafine and stable PtFe nano-alloy with ultra-low Pt loading for complete removal of CO in PROX at room temperature. *Appl. Catal. B* **2016**, *180*, 237–245.
 - (13) Ma, D.; Tang, Y.; Yang, G.; Zeng, J.; He, C.; Lu, Z. CO catalytic oxidation on iron-embedded monolayer MoS₂. *Appl. Surf. Sci.* **2015**, *328*, 71–77.
 - (14) Ma, D. W.; Li, T.; Wang, Q.; Yang, G.; He, C.; Ma, B.; Lu, Z. Graphyne as a promising substrate for the noble-metal single-atom Catalysts. *Carbon* **2015**, *95*, 756–765.
 - (15) Li, Y.; Zhou, Z.; Yu, G.; Chen, W. and Chen, Z. CO Catalytic Oxidation on Iron-Embedded Graphene: Computational Quest for Low-Cost Nanocatalysts. *J. Phys. Chem. C* **2010**, *114*, 6250–6254.
 - (16) Song, E. H.; Wen, Z.; Jiang, Q. CO catalytic oxidation on copper-embedded graphene, *J. Phys. Chem. C* **2011**, *115* (9), 3678–3683.
 - (17) Liu, X.; Sui, Y.; Duan, T.; Meng, C.; Han, Y. CO oxidation catalyzed by Pt embedded graphene: a first-principles investigation, *Phys. Chem. Chem. Phys.* **2014**, *16* (43), 23584–23593.
 - (18) Li, F.; Zhao, J. and Chen, Z. Fe-Anchored Graphene Oxide: A Low-Cost and Easily Accessible Catalyst for Low-Temperature CO Oxidation. *J. Phys. Chem. C* **2012**, *116*, 2507–2514.
 - (19) Mao, K.; Li, L.; Zhang, W.; Pei, Y.; Zeng, X. C.; Wu, X. et al. A theoretical study of single-atom catalysis of CO oxidation using Au embedded 2D h-BN monolayer: a CO-promoted O₂ activation, *Sci. Rep.* **2014**, *4*, 1–7.
 - (20) Lin, S.; Ye, X.; Johnson, R. S.; Guo, H. First-principles investigations of metal (Cu, Ag, Au, Pt, Rh, Pd, Fe, Co, and Ir) doped hexagonal boron nitride nanosheets: stability and catalysis of CO oxidation, *J. Phys. Chem. C* **2013**, *117* (33), 17319–17326.
 - (21) Liu, X.; Duan, T.; Sui, Y.; Meng, C.; Han, Y. Copper atoms embedded in hexagonal boron nitride as potential catalysts for CO oxidation: a first-principles investigation. *RSC Adv.* **2014**, *4* (73), 38750–38760.
 - (22) Sinthika, S.; Kumar, E. M.; Thapa, R. Doped h-BN monolayer as efficient noble metal-free catalysts for CO oxidation: the role of dopant and water in activity and catalytic de-poisoning, *J. Mater Chem. A* **2014**, *2* (32), 12812–12820.
 - (23) Liu, X.; Duan, T.; Meng, C.; Han, Y. Pt atoms stabilized on hexagonal boron nitride as efficient single-atom catalysts for CO oxidation: a first-principles investigation. *RSC Adv.* **2015**, *5* (14), 10452–10459.

- (24) Narasimharao, K.; Al-Shehri, A.; Al-Thabaiti, S. Porous Ag–Fe₂O₃nanocomposite catalysts for the oxidation of carbonmonoxide. *Appl. Catal. A* **2015**, *505*, 431–440.
- (25) Afanasev, D. S.; Yakovina, O. A.; Kuznetsova, N. I.; Lisitsyn, A. S. High activity in CO oxidation of Ag nanoparticles supported on fumed silica. *Catal. Commun.* **2012**, *22*, 43–47.
- (26) Zhang, X. D.; Qu, Z. P.; Yu, F. L.; Wang, Y. High-temperature diffusion induced high activity of SBA-15 supported Ag particles for low temperature CO oxidation at room temperature. *J. Catal.* **2013**, *297*, 264–271.
- (27) Yousefi, N.; Pazouki, M.; Alizadeh, M. and Hesari, F. A. Biosynthesis of Ag/MWf-CNT Nanocomposites Using *Aspergillus fumigatus* as the CO Oxidation Catalyst. *Synthesis and Reactivity in Inorganic, Metal-Organic, and Nano-Metal Chemistry* **2016**, *46*, 464–470.
- (28) Zhang, X. D.; Qu, Z. P.; Li, X. Y.; Wen, M.; Quan, X.; Ma, D.; Wu, J. J. Studies of silver species for low-temperature CO oxidation on Ag/SiO₂ catalysts. *Sep. Purif. Technol.* **2010**, *72*, 395–400.
- (29) Tang, D.; Chen, Z.; Hu, J.; Sun, G.; Lu, S. and Hu, C. CO oxidation catalyzed by silver nanoclusters: mechanism and effects of charge. *Phys. Chem. Chem. Phys.* **2012**, *14*, 12829–12837.
- (30) Chi, Y.; Zhao, L.; Lu, X.; An, C.; Guo, W.; Wu C. L. Effect of alloying on the stabilities and catalytic properties of Ag–Au bimetallic subnanoclusters: a theoretical investigation. *J. Mater. Sci.* **2016**, *51*, 5046–5060.
- (31) Negreiros, F. R.; Sementa, L.; Barcaro, G.; Vajda, S.; Aprá, E. and Fortunelli, A. CO Oxidation by Subnanometer Ag_xAu_{3-x} Supported Clusters via Density Functional Theory Simulations. *ACS Catal.* **2012**, *2*, 1860–1864.
- (32) Wei, Z.; Li, D.; Pang, X.; Lv, C. and Wang, G. The Mechanism of Low-Temperature CO Oxidation on IB Group Metals and Metal Oxides. *ChemCatChem* **2012**, *4*, 100–111.
- (33) Gaussian 09, Revision B.01, Frisch, M. J. et al., Gaussian, Inc., Wallingford CT, 2010.
- (34) Perdew, J. P.; Chevary, J. A.; Vosko, S. H.; Jackson, K. A.; Pederson, M. R.; Singh, D. J.; Fiolhais, C. Atoms, molecules, solids, and surfaces: Applications of the generalized gradient approximation for exchange and correlation. *Phys Rev B* **1992**, *46*, 6671.
- (35) Perdew, J. P.; Burke, K.; Wang, Y. Generalized gradient approximation for the exchange-correlation hole of a many-electron system. *Phys Rev B* **1996**, *54*, 16533.
- (36) Soo, T.; Qin, C. Adsorption and Dissociation of Carbon Trioxide on Ag(100). *Int. J. Quantum Chem.* **2010**, *110*, 946–952.
- (37) Kuang, X.; Wang, X.; Liu, G. A density functional theory study on the Ag_nH (*n* = 1–10) clusters. *Struct Chem.* **2011**, *22*, 517–524.
- (38) Kuang, X.; Wang X.; Liu, G. A density functional study on the Au_nAg (*n* = 1–12) alloy clusters. *J. Alloys Compd.* **2013**, *570*, 46–56.
- (39) Kuang, X.; Wang X.; Liu, G. The adsorptions of silver-doped small gold clusters toward carbon monoxide molecule. *Struct Chem.* **2012**, *23*, 671–679.
- (40) Stewart, D. M.; Mavros, M. G. and Micha D. A. Light Absorption by Crystalline and Amorphous Silicon Quantum Dots with Silver Adsorbates and Dopants. *J. Phys. Chem. C*

2012, 116, 23107–23112.

- (41) Hay, P. J.; Wadt, W. R. *Ab initio* effective core potentials for molecular calculations. Potentials for the transition metal atoms Sc to Hg. *J Chem. Phys.* **1985**, 82, 270.
- (42) Wadt, W. R.; Hay, P. J. *Ab initio* effective core potentials for molecular calculations. Potentials for main group elements Na to Bi. *J Chem. Phys.* **1985**, 82, 284.
- (43) Hay, P. J.; Wadt, W. R. *Ab initio* effective core potentials for molecular calculations. Potentials for K to Au including the outermost core orbitals. *J Chem. Phys.* **1985**, 82, 299.
- (44) Rassalov, V. A.; Pople, J. A.; Ratner, M.; Windus, T. L. 6-31G* basis set for atoms K through Zn. *J Chem. Phys.* **1998**, 109, 1223.
- (45) Hariharan, P. C.; Pople, J. A. The influence of polarization functions on molecular orbital hydrogenation energies. *Theor. Chim. Acta* **1973**, 28, 213.
- (46) Francel, M. M.; Pietro, W. J.; Hehre, W. J.; Binkley, J. S.; Gordon, M. S.; DeFrees, D. J.; Pople, J. A. Self-consistent molecular orbital methods. XXIII. A polarization-type basis set for second-row elements. *J Chem. Phys.* **1982**, 77, 3654.
- (47) Fukui, K. The path of chemical-reactions - The IRC approach. *Acc. Chem. Res.*, **1981**, 14, 363–68.
- (48) Hratchian H. P. and Schlegel, H. B. Using Hessian updating to increase the efficiency of a Hessian based predictor-corrector reaction path following method. *J. Chem. Theory and Comput.*, **2005**, 1, 61–69.
- (49) Vosko, S. H.; Wilk, L.; Nusair, M. Accurate spin-dependent electron liquid correlation energies for local spin density calculations: a critical analysis. *Can. J. Phys.* **1980**, 58, 1200.
- (50) Lee, C.; Yang, W.; Parr, R. G. Development of the Colle-Salvetti correlation-energy formula into a functional of the electron density. *Phys. Rev. B* **1988**, 37, 785.
- (51) Becke, A. D. Density-functional exchange-energy approximation with correct asymptotic behavior. *Phys. Rev. A* **1988**, 38, 3098.
- (52) Gajdoš, M.; Eichler A. and Hafner, J. CO adsorption on close-packed transition and noble metal surfaces: trends from *ab initio* calculations. *J. Phys.: Condens. Matter*, **2004**, 16, 1141–1164.
- (53) Hansen, W.; Bertolo, M.; Jacobi, K. Physisorption of CO on Ag(111): investigation of the monolayer and the multilayer through HREELS, ARUPS, and TDS. *Surf. Sci.* **1991**, 253, 1.
- (54) McElhiney, G.; Papp, H.; Pritchard, J. The adsorption of Xe and CO on Ag (111). *Surf. Sci.*, **1976**, 54, 617
- (55) Backx, C.; de Groot, C. P. M. and Biloen, P. Adsorption of oxygen on Ag (110) studied by high resolution ELS and TPD. *Surf. Sci.*, **1981**, 104, 300–317.
- (56) Qin, C.; Sremaniak, L. S. and Whitten, J. L. CO Adsorption on Ag(100) and Ag/MgO(100). *J. Phys. Chem. B* **2006**, 110, 11272–11276.
- (57) Engle, T.; Ertl, G. A molecular beam investigation of the catalytic oxidation of CO on Pd(111). *J. Chem. Phys.* **1978**, 69, 1267.

- (58) Engle, T. A molecular beam investigation of He, CO, and O₂ scattering from Pd(111). *J. Chem. Phys.* **1978**, 69, 373.
- (59) Kuipers, E. W.; Vardi, A.; Danon, A.; Amirav, A. Surface-molecule proton transfer: A demonstration of the Eley-Rideal mechanism. *Phys. Rev. Lett.* **1991**, 66, 116–119.
- (60) Rettner, C. T. Dynamics of the direct reaction of hydrogen atoms adsorbed on Cu(111) with hydrogen atoms incident from the gas phase. *Phys. Rev. Lett.* **1992**, 69, 383–386.
- (61) Stampfl, C.; Scheffler, M. Anomalous Behavior of Ru for Catalytic Oxidation: A Theoretical Study of the Catalytic Reaction $\text{CO} + 1/2\text{O}_2 \rightarrow \text{CO}_2$. *Phys. Rev. Lett.* **1997**, 78, 1500–1503.

Novel MC/BZY Proton Conductor: Materials Development, Device Evaluation, and Theoretical Exploration using CI and DFT Methods

Changyong Qin, Benedict College, Columbia, SC 29204 (PI)

Kevin Huang, University of South Carolina, Columbia, SC 29208 (Co-PI)

(Education and Community Services Part)

PART A: STUDENT MENTORING

The following students have been involved in the research activities supported by the current grant in the year of 2013-2017. Six of the seven students were female African America and the work funded from this grant had served as their requirements for senior thesis/oral defense. One graduate student completed a Ph.D. degree with partial support from the grant in the Co-PI group at the University of South Carolina

Kahla Haines, Chemistry Major, Benedict College, B.S. Degree 2015

Susan Njoki, Chemistry Major, Benedict College, B.S. Degree 2016

June P. Medina, Chemistry Major, Benedict College, B.S. Degree 2017

Renee Terrell, Biology Major, Benedict College, B.S. Degree 2017

Shanice Fezeu, Biology Major, Benedict College, B.S. Degree 2017

Tamia Brice, Chemistry Major, Benedict College, B.S. Degree 2019 (expected)

Maria Melville, Biology Major, Benedict College, B.S. Degree 2019 (expected)

Xiaolei Xiong, Mechanical Engineering, PhD in 2017, University of South Carolina

Dr. Xueling Lei, Postdoc Research Associate

Dr. Jingjing Tong, Postdoc Research Associate

PART B: INFRASTRUCTURE IMPROVEMENT

The Undergraduate Teaching and Research Laboratory for Advanced Materials (UTRAM) has been developed with increased research capacity and is now the Center for Advanced Materials (CAM) at Benedict College. It serves a core facility for faculty/student research and also for the STEM education and community services. In particular, follow instruments have been purchased and added to CAM through the current grant supports.

Vacuum drying oven (QTN: 1)

VERASTA3-200 Advanced DC Voltammetry System (QTN: 1)

Solartron 1470 Fuel Cell Test System (QTN: 1)

High temperature sample stage for Raman Spectroscopy (QTN: 1)

64-Core Intel Computing Server (QTN: 1)

AMD Opteron Quad-Socket Computing System (QTN: 4)

Rotating Disc Electrode System (QTN: 1)

Planetary Ball Mill (QTN: 1)

Rotary Ball Mill (QTN: 1)

PART C: PUBLICATIONS AND PRESENTATIONS

The project funded by the current grant has led to several conference and meeting presentations, and also six papers published in peer-reviewed journals and two manuscripts being submitted. Below is the complete list.

CO Oxidation by Molten Carbonate: A DFT Study

S. Njoki and C. Qin, WoPhyS'15, Lincoln, Nebraska

Proton Transfer in Molten Carbonate: Mechanism and Kinetics from DFT Study

X. Lei and C. Qin, APS annual spring meeting, Washington, DC, March, 2016

Molten Carbonate as Non-metal Catalyst for CO Oxidation

J. Tong and C. Qin manuscript in submission.

Kinetics and Mechanism of Proton Transfer in Molten Lithium Carbonate: Insights from Static and Dynamic DFT Studies

X. Lei, K. Huang, C. Qin, Scientific Reports, DOI: 10.1038/s41598-017-07726-3.

DFT Study of CO Oxidation by Molten Carbonate

X. Lei, K. Huang, C. Qin, manuscript in preparation.

DFT Study of Oxygen Migration in Molten Carbonate

X. Lei, K. Haines, K. Huang, C. Qin, J. of Power Sources, 2016, 305, 161-166.

Enhanced Interfacial Proton Migration on BaZr(Y)O₃ by Molten Carbonate: A First Principles Study

X. Lei, K. Huang, C. Qin, Solid State Ionics , 2016, 289, 48-54.

DFT Study of Oxygen Dissociation in Molten Carbonate

X. Lei, K. Haines, K. Huang, C. Qin, J. of Phys. Chem. A, 2015, 119, 8806-8812.

Energetics of Proton Transfer in Alkali Carbonates: A First Principles Calculation

X. Lei, C. Qin, K. Huang, RSC Advances, 2015, 5, 56205-56209.

Synergetic Proton Conduction in BZY-Carbonate Composite Electrolyte for IT-SOFC

X. Xiong, X. Lei, C. Zhang, J. Wang, K. Huang, Solid State Ionics , 2015, 279, 66-71.

PART C: OUTREACH ACTIVITIES

The grant has supported the Xtreme Technology Event for high school students at Benedict College. Most of them are from African American community. Three African American

middle/high school students have also participated a one-week fuel cell program at the Co-PI laboratory at The University of South Carolina.

The grant has supported the Xtreme Technology Event for high school students at Benedict College. Most of them are from African American community. The grant also allowed the STEM students to participate the annual Harambee festival on the campus of Benedict College, which services the local African American community and increases their awareness of high technologies.